A Robinson Wiggler for the Metrology Light Source

Dissertation

zur Erlangung des akademischen Grades

doctor rerum naturalium

(Dr. rer. nat.)

im Fach: Physik

Spezialisierung: Experimentalphysik

eingereicht an der

Mathematisch-Naturwissenschaftlichen Fakultät

der Humboldt-Universität zu Berlin

von

Dipl.-Phys. Tobias Tydecks (geb. Goetsch)

Präsidentin der Humboldt-Universität zu Berlin

Prof. Dr.-Ing. Dr. Sabine Kunst

Dekan der Mathematisch-Naturwissenschaftlichen Fakultät

Prof. Dr. Elmar Kulke

Gutachter:
1. Prof. Dr. Andreas Jankowiak
2. PD Dr. Bernhard Schmidt
3. Prof. Dr. Riccardo Bartolini

Tag der mündlichen Prüfung: 16.11.2016

Abstract

In 1958, Kenneth W. Robinson proposed the usage of a magnetic correction device to reduce the antidamping of the radial betatron oscillations in the Cambridge electron accelerator (Robinson, 1958). The essence of this correction device are short, alternating dipoles with a strong gradient, such that the radiation loss decreases with increasing radius of the trajectory. In 1986, four of these transverse gradient "Robinson" Wigglers (RW) were installed to the Proton Synchrotron (PS) at CERN so that the PS could serve in the Large-Electron-Positron-Collider (LEP) injector chain for positron and electron acceleration (Baconnier et al., 1985). In recent years, the RW concept came into focus again in the scope of synchrotron light sources. In order to reduce the horizontal emittance, a RW could be installed as an upgrade option for existing machines, e.g. at SOLEIL (Abualrob et al., 2012). Newly built light sources, like MAX IV (Tavares et al., 2014), are optimized concerning their damping distribution using combined function dipoles, which make use of the same theoretical framework as the RW.

The Metrology Light Source (MLS), owned by the Physikalisch-Technische Bundesanstalt (PTB), is an electron synchrotron which was designed and is operated by the Helmholtz-Zentrum Berlin für Materialien und Energie (HZB) (Abo-Bakr, 2000; Klein et al., 2008). It is optimized for the production of synchrotron radiation in the THz to the Extreme-Ultraviolet (EUV) spectral region. Compared to other light sources, the MLS is a low electron energy synchrotron, with a nominal operation energy of 629 MeV. Unlike BESSY II, which is a 3$^{\text{rd}}$ generation, 1.7 GeV synchrotron light source of HZB, the MLS does not feature a full energy injection and therefore Top-Up operation is not possible. With a decaying beam current, the lifetime of the stored beam is of importance for the user community, for reasons of temporal stability and integrated photon flux.

It is proposed to install a RW at the MLS in order to improve the lifetime. With a RW, it is possible to transfer damping from the longitudinal to the horizontal plane in a way, that the energy spread increases by a factor of ~ 3 and the emittance reduces by a factor of ~ 2. Doing so, the bunch length is increased by a larger

fraction than the average horizontal bunch width is decreased. Thereby the electron density is reduced which results in a lower loss rate of the electrons. This improves the beam lifetime and reduces induced radioactivity of accelerator components and shielding. The latter being of increasing significance for the developments towards diffraction limited storage rings, where high scattering rates occur due to small beam sizes.

With an increased energy spread and a reduced emittance, the contribution of the dispersion to source size becomes more important. By carefully choosing the magnet optics, the brilliance at the source point can be improved simultaneously to increasing the lifetime. Simulations indicate that a RW, like the one proposed in this thesis, is able to increase the beam lifetime in the standard user operation mode at the MLS by a factor of 2.3, corresponding to an increase in integrated photon flux for one standard user run of approximately 30 %. With installing such a device, the damping partition numbers become tunable, opening access to new operation modes and enhancing the existing ones.

Contents

Abbreviations and Symbols

α	Momentum Compaction Factor
$\alpha_{x/y}$	Courant-Snyder Parameter, $\alpha_{x/y} = -\beta'_{x/y}/2$
At	Unit: Ampere turns
$\boldsymbol{B}$	Magnetic Induction
BESSY	Berliner Elektronen-Speicherring für Synchrotronstrahlung
β	Ratio between speed v and the speed of light c: $\beta = v/c$
β_0	Ratio between speed v and the speed of light c of the reference particle
$\beta_{x/y}$	Horizontal / Vertical β-function, Courant-Snyder Parameter
BPM	Beam Position Monitor
BW	Bandwidth
c	Speed of Light; in vacuum: $c = 299\,792\,458\,\mathrm{m\,s^{-1}}$
$\tilde{c}$	Proportionality Constant in Touschek Lifetime
C_γ	Radiation Constant; $C_\gamma \approx 8.85 \times 10^{-5}\,\mathrm{m\,GeV^{-3}}$
C_q	Quantum Constant; $C_q \approx 3.83 \times 10^{-13}\,\mathrm{m}$
CERN	European Organization for Nuclear Research
γ	Lorentz Factor
$\gamma_{x/y}$	Courant-Snyder Parameter, $\gamma_{x/y} = (1+\alpha_{x/y}^2)/\beta_{x/y}$
D	Damping Partition: Ratio between I_4 and I_2
$\mathscr{D}$	Function used to calculate contributions to the Touschek Lifetime
DBA	Double Bend Achromat
δ	Momentum Deviation from Reference Momentum normalized to the Reference Momentum

δ_{acc}	Momentum Acceptance normalized to the Reference Momentum
e	Elementary Charge $e = 1.602\,176\,620\,8(98) \times 10^{-19}\,\mathrm{C}$
E	Particle Energy
$\boldsymbol{E}$	Electric Field
E_0	Energy of Reference Particle
E_γ	Photon Energy
ϵ_0	Vacuum Permittivity $\epsilon_0 \approx 8.854\,187\,817 \times 10^{-12}\,\mathrm{A\,s\,V^{-1}\,m^{-1}}$
ERL	Energy Recovery LINAC
EUV	Extreme Ultraviolet
$\varepsilon_{x/y}$	Horizontal / Vertical Emittance
η_c	Phase Slip Factor
η_x	Horizontal Dispersion
f_{rev}	Revolution Frequency
f_{rf}	RF-Frequency
f_s	Synchrotron Frequency
h	Harmonic Number
$\mathscr{H}$	Chromatic Invariant
HZB	Helmholtz-Zentrum Berlin
I	Beam Current
$I_{1\ldots5}$	Synchrotron Radiation Integrals
$I_{F1/2}$	First / Second Field Integral
ID	Insertion Device
IDB	ID-Beamline
IR	Infrared
$j_{x/y/s}$	Damping Partition Numbers
K	Deflection Parameter of ID
κ	Emittance Coupling Parameter: $\kappa = \frac{\varepsilon_y}{\varepsilon_x}$
k_i	Multipole Strength Parameter for Multipole of Order i, normalized by $B\rho$: $k_i = \frac{1}{B\rho}\frac{\partial^i B_y}{\partial x^i}$
λ_i	Wavelength of the i-th Undulator Harmonic
λ_{ID}	Periodlength of ID
LEP	Large Electron-Positron Collider (CERN)
LHC	Large Hadron Collider (CERN)

LINAC	Linear Accelerator
LOCO	Linear Optics from Closed Orbits
MAD	Methodical Accelerator Design
MLS	Metrology Light Source
∇	Nabla (Vector): $\left(\frac{\partial}{\partial x}, \frac{\partial}{\partial y}, \frac{\partial}{\partial z}\right)$
p	Particle Momentum
p_0	Momentum of Reference Particle
PCT	Parametric Current Transformer
PS	Proton Synchrotron (CERN)
PTB	Physikalisch-Technische Bundesanstalt
PTC	Polymorphic Tracking Code
QNIM	Source Normal Incident Monochromator
QPD	Source Point Imaging
$Q_{x/y}$	Horizontal / Vertical Tune
r_e	Classical Electron Radius
	$r_e = 2.817\,940\,326\,7(27) \times 10^{-15}\,\mathrm{m}$
rf	Radio Frequency
rms	root mean square
RW	Robinson Wiggler
ρ	Bending Radius
SU	Standard User
σ_δ	Energy Spread
σ_s	RMS-Bunchlength
$\sigma_{x/y}$	Horizontal / Vertical RMS-Beamsize
T	Revolution Time
τ	Lifetime
τ_g	Gas Lifetime
τ_q	Quantum Lifetime
τ_t	Touschek Lifetime
U_0	Energy Loss per Turn
UV	Ultraviolet
V	Scalar Potential
V_{rf}	Cavity Voltage
$\xi_{x/y}$	Horizontal / Vertical Chromaticity
Z	Atomic Number

Introduction

With the development of the theory of quantum mechanics in the early 20th century,
particles could be described as waves according to De Broglie's wavelength

$$\lambda = \frac{h}{p}, \tag{1.1}$$

with Planck's constant h in the numerator and the momentum p of the particle in
the denominator. With increasing momentum, the associated wavelength shortens,
enabling the particle to reveal more detail during a scattering process. Limited
to $\sim 5\,\text{MeV}$, α-particles were a natural source of test particles to perform scatter-
ing experiments. In order to obtain higher resolution, particle accelerators were
invented. In addition to the finding of greater detail in the structure of matter,
more massive particles could be generated during collisions according to Einstein's
$E = mc^2$ (Wilson, 2001). Since their invention, particle accelerators have continued
to grow in accelerator complex size and achievable energy of the particle beams.
They opened the door to new particle physics such as finding quarks, gluons and
more recently the Higgs boson (Aad et al., 2012; Chatrchyan et al., 2012). Today,
particle accelerators are still the major tool for particle physics and, in the case of
the Large Hadron Collider (LHC) in Geneva, can reach up to $27\,\text{km}$ in circumference,
delivering proton beams with energies up to $7\,\text{TeV}$.

When accelerating charged light particles, like electrons or positrons, the max-
imum achievable energy is limited due to radiation emitted by the particles undergo-
ing acceleration. This radiation was first observed at a $70\,\text{MeV}$ electron synchrotron
of the General Electric Company Research Laboratory (New York State) in the late
1940's. *Synchrotron radiation* was first seen as a negative effect, because the "lost"
energy had to be fed back to the beam additionally to the energy needed for acceler-
ation. However, several years later, scientists considered using the emitted radiation

parasitically. What began as a by-product, became its own field of research in the late 1960's, when the first dedicated synchrotron radiation facility Tantalus, of the Synchrotron Radiation Center in Madison, Wisconsin / USA, came into operation (Lynch, 1997). Today, many so called "light sources" are in operation around the world. These light sources store electrons for the sole purpose of emitting high intensity, polarized, broad banded, exactly calculable, pulsed synchrotron radiation. It is used in various fields of science such as materials science, physical chemistry, biophysics, life science and metrology.

As a large number of particles is stored in the accelerator, it becomes probable that a particle is lost due to scattering events with other particles or gas atoms. Therefore, the stored beam is decaying with time. Hence, it is possible to define a lifetime of the beam which should be as long as possible in order to provide stable experimental conditions and to minimize induced radioactivity by particle losses. The beam lifetime of an electron synchrotron, namely the MLS of Germany's national metrology institute PTB, is the subject of this thesis. A concept to improve the beam lifetime while simultaneously improving the brilliance at selected beamlines is developed.

1.1 Synchrotron Radiation

Ultra-relativistic charged particles which are accelerated emit electromagnetic dipole radiation. The power emitted by light particles such as electrons or positrons is many orders of magnitude higher than that of heavier particles such as protons or ions. Usually the energy losses due to synchrotron radiation are negligible for heavy particles like protons. For electrons, due to their low mass, it is a strong effect. The spectrum of the emitted radiation is shifted to higher photon energies depending on the momentum of the emitting particles (comp. MLS at 105 MeV and 629 MeV in Fig. 1.1).

The radiation is emitted by particle bunches. In the laboratory frame, these bunches can be seen as delta peaks passing by the source point. The Fourier transform of a delta peak gives a broad spectrum, which is one of the reasons why synchrotron radiation became popular. The spectrum reaches from the Far-Infrared (FIR) to the hard X-Ray regime. Users may choose the wavelength with which they wish to conduct experiments using a monochromator. In Fig. 1.1, the spectra for the Extreme-Ultraviolet (EUV) beamlines of PTB at the MLS and at BESSY II are presented. Due to a smaller acceptance at the dipole beamline, the spectrum for
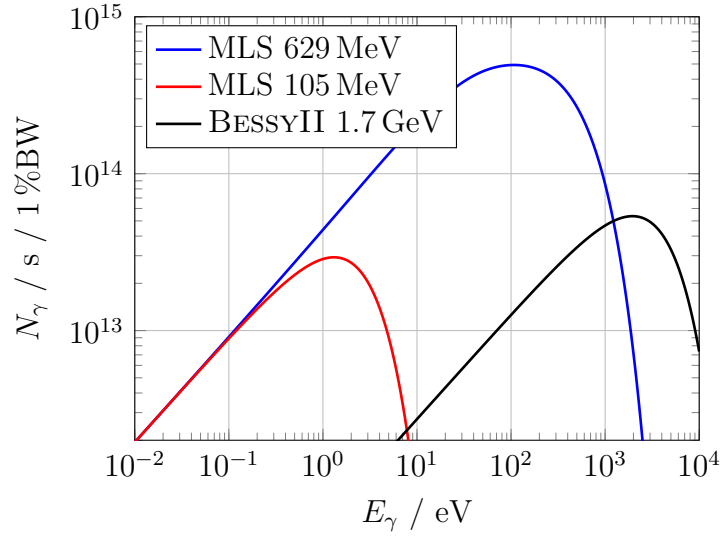
Figure 1.1: Number of photons from a bending magnet through the acceptances at PTB's EUV-beamlines at the MLS and at BESSYII as a function of the photon energy.

photon energies below 1 keV shows less intensity for BESSYII than for the MLS. But as BESSYII operates at 1.7 GeV, its dipole spectrum covers also the X-Ray regime up to several 10 keV.

In contrast to the MLS, BESSYII is a third generation light source. First generation light sources were parasitically used accelerators built for particle physics. Second generation light sources were built solely for the generation of synchrotron radiation. The radiation that was emitted in the deflecting dipoles was used and beam parameters could be adjusted to meet user demands. Third generation light sources, which most of today's light sources belong to, feature *insertion devices* (ID) in the straight sections between the deflecting dipoles as their main radiation source. These ID's, usually consisting of a sequence of short dipoles with alternating field, send the beam on an alternating / undulating trajectory. With each oscillation period, synchrotron radiation is emitted. Depending on the oscillation amplitude of the trajectory, ID's are distinguished between *undulators* and *wigglers*. Undulators cause the electron beam to follow a gentle, periodic, undulating trajectory so that the emitted wavefronts overlap and interference effects occur (Clarke, 2004). Depending on the wavelength, the interference is constructive and large enhancement in intensity can be observed. Wigglers send the beam on higher oscillation amplitudes, resulting in no overlap between the wavefronts. Instead, the spectrum of the emitted radiation compares to that of a single dipole with the exception that it has the number of poles fold intensity. The MLS features one ID (U125, Fig. 1.2),
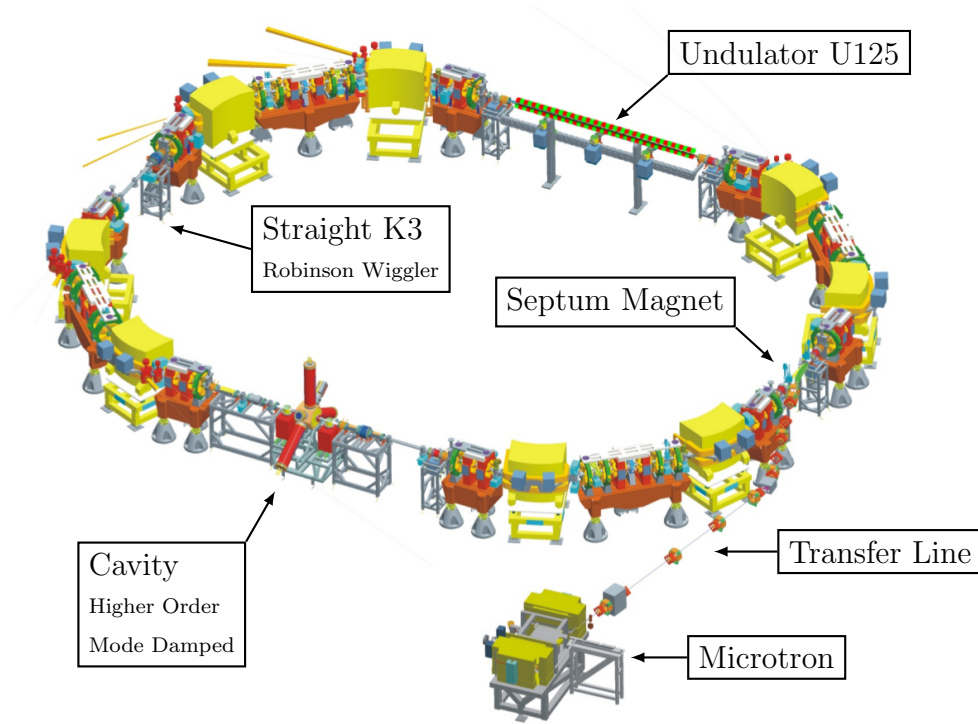
Figure 1.2: Scheme of the Metrology Light Source, with microtron and transfer line.

but mainly serves dipole beamlines. It is therefore part of an own class between the second and third generation of light sources.

1.2 The Metrology Light Source

The MLS (Fig. 1.2) is an electron synchrotron situated in Berlin (Germany). It is owned by the Physikalisch-Technische Bundesanstalt (PTB) and operated and designed by the Helmholtz-Zentrum Berlin für Materialien und Energie (HZB). It is dedicated to metrology and technological developments in the Ultraviolet (UV) and EUV spectral range as well as in the Infrared (IR) and THz region. It can be operated at any energy between 50 MeV and 629 MeV, while the stored current can be varied from 200 mA down to a single electron (= 1 pA).

The electrons are extracted from a heated cathode and accelerated to 70 keV in the electron gun. From there, they are injected into a racetrack microtron where they are accelerated to 105 MeV. Through the transfer line, the electrons may then be injected into the synchrotron. Here the electrons are accumulated up to the desired beam current at 105 MeV. The highest possible beam current is 200 mA due to radiation protection requirements. The electron energy in the synchrotron

can be varied between 50 MeV and 629 MeV, the latter being the nominal energy during user operation. The MLS consists of four double bend achromat (DBA) cells. All together 24 individually powered quadrupoles are installed to provide transverse focussing. The 24 sextupoles are grouped into three sextupole families, providing control of the chromaticities in all three planes. Furthermore, each DBA structure has an octupole magnet placed at its centre. Together with the third sextupole family, the octupole is used to alter higher order momentum compaction factor terms (Ries, 2014).

The MLS features multiple operation modes specialized for different applications. The most important and regularly set up operation modes are the standard user operation mode (SU), the low-α mode, and the low-ε mode (comp. Fig. 1.3). The key figures for the MLS in standard user operation mode are listed in Tab. 1.1. If not noted otherwise, all calculations in this thesis will be conducted for the standard user operation mode at 629 MeV with a stored beam current of 150 mA. During a typical standard user operation run at the MLS, the beam usually decays from 200 mA to 80 mA in a time interval of 6 h. Due to the varying beam current, the vertical beam size has to be controlled using a stripline kicker and a random frequency generator. Thus, the beam is vertically excited with "white noise". Doing so, current dependent ion effects on the source size are reduced and reliable conditions are maintained. The excitation strength is varied according to the stored beam current in order to maintain a vertical source size of 280 µm at one of the diagnosis beamlines.

Due to its low operation energy, in comparison to other light sources, the beam lifetime at the MLS is dominated by the Touschek effect. Electrons scattering with other electrons within the same bunch exchange momenta and may get lost to the limiting acceptance. In order to reduce induced radioactivity due to beam losses and to improve the timely stability of the radiation, as well as the integrated photon flux, it is beneficial to improve the beam lifetime. To increase the lifetime, it is necessary to improve the Touschek lifetime component. This is done by reducing the electron density inside the bunch. One way to achieve this goal shall be investigated in this thesis: by redistributing the damping partition of the beam, the bunch length can be increased. Thus, the electron density is reduced, resulting in an increased lifetime. The damping partition is altered using combined function magnets. For an existing accelerator, an insertion device consisting of combined function magnets can be used. Such a device is called a Robinson Wiggler (RW) and is presented in the following section.
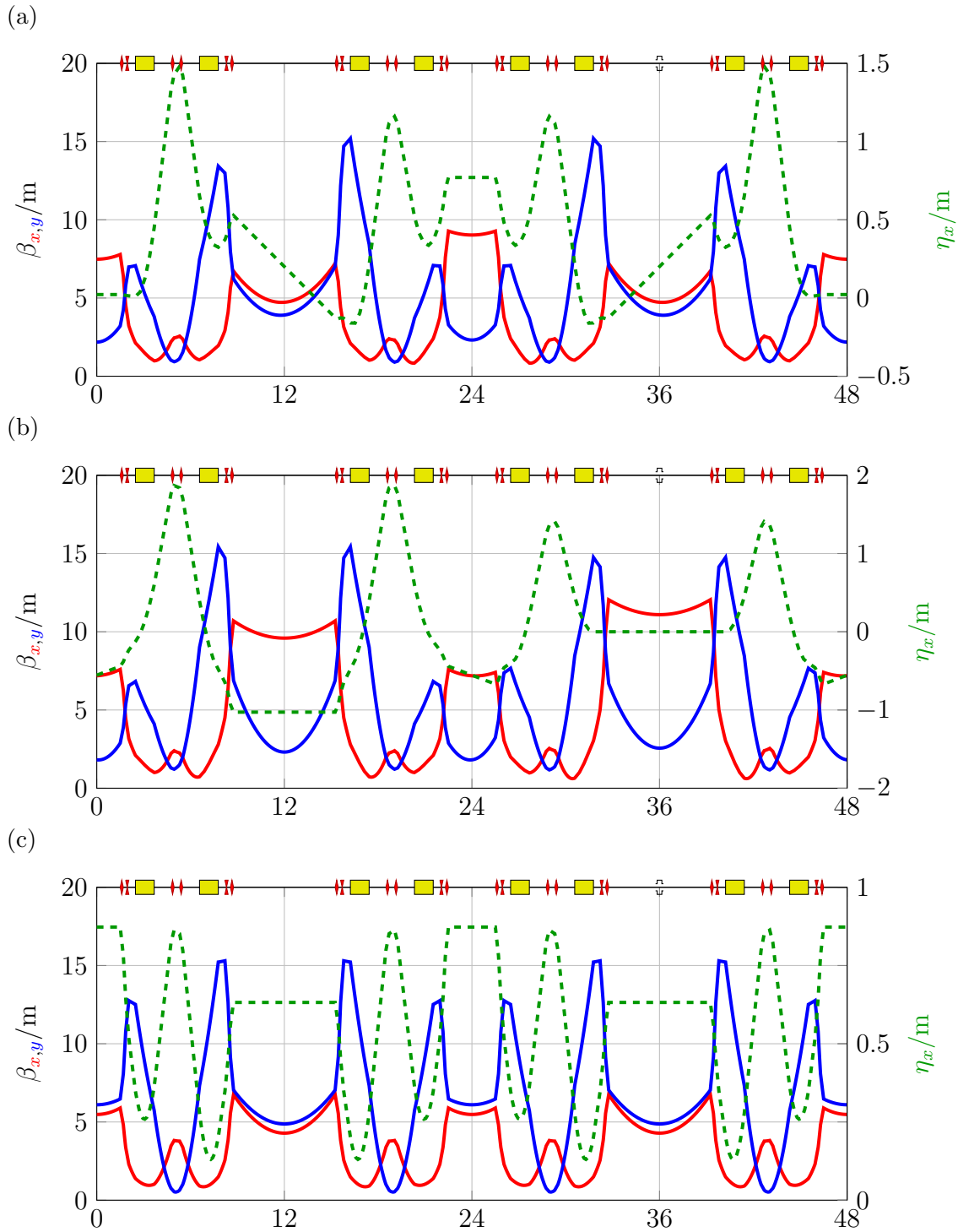
(a)

(b)

(c)

Figure 1.3: Optical functions of the typical user operation modes at the MLS: the
standard user operation mode (a), the low-α operation mode (b), and the low-ε mode
(c).

Table 1.1: Key figures for the standard user operation mode at the MLS. Rows marked with "(SU)" are standard user operation mode specifics. The column "(RW)" indicates the possible changes with a twelve poled Robinson Wiggler (dispersion at RW: $\eta_x = 1.1\,\mathrm{m}$, excitation current density $j = 7.1\,\mathrm{A\,mm^{-2}}$). Calculated values are marked with ^{c}.

quantity		value	(RW)	unit
circumference		48.0		m
electron energy E_0		629.0		MeV
γ		1230.92		
dipole bending radius ρ		1.528		m
magnetic induction dipoles B_y		1.373		T
beam current I:				
I_min		1.0		pA
I_max		200.0		mA
beam lifetime τ at 150 mA	(SU)	6.0	12.0^c	h
tunes:				
Q_x	(SU)	3.178		
Q_y	(SU)	2.232		
chromaticities without sextupoles:				
ξ_x	(SU)	-3.39	0.57^c	
ξ_y	(SU)	-4.91	-5.62^c	
momentum compaction factor α	(SU)	0.031	0.034^c	
rf-cavity voltage V_rf	(SU)	500.0		kV
rf-frequency f_rf		499.648		MHz
revolution frequency f_rev		6.246		MHz
synchrotron frequency f_s	(SU)	110.6	115.9^c	kHz
harmonic number h		80		
damping constants:				
j_x	(SU)	1.055^c	2.72^c	
j_y	(SU)	1.0^c		
j_s	(SU)	1.945^c	0.28^c	
damping partition D	(SU)	-0.055^c	-1.72^c	
damping times:				
τ_x	(SU)	21.05^c	8.17^c	ms
τ_y	(SU)	22.21^c		ms
τ_s	(SU)	11.42^c	79.32^c	ms
horizontal emittance ε_x	(SU)	117.37^c	50.74^c	nm rad
energy spread σ_δ		0.44	1.16^c	‰
bunch length σ_s	(SU)	20.75	54.7^c	ps
apertures:				
full chamber height septum magnet		37.0		mm
full chamber width septum magnet		56.0		mm
full chamber height undulator chamber		24.0		mm
full chamber width undulator chamber		74.0		mm
full chamber height remaining magnets		42.0		mm
full chamber width remaining magnets		70.0		mm

Figure 1.4: One of the four RW's that had been installed at the PS for the electron / positron acceleration during LEP runs. Picture from (Nadolski, 2011).

1.3 Robinson Wiggler Concept

A Robinson Wiggler (RW) is a sequence of alternating combined function magnets. Placed in a dispersive section, this arrangement enables one to redistribute damping between the longitudinal and the deflection plane (usually the horizontal plane).

The idea first appeared in 1958, when Kenneth W. Robinson proposed the usage of a magnetic correction device to reduce the antidamping of radial betatron oscillations in the Cambridge electron accelerator (Robinson, 1958). The device consists of alternating dipoles with a gradient, so that the radiation losses decrease with increasing radius. Such, longitudinal and horizontal damping are coupled and the damping distribution between the two planes can be controlled by the field strength of the device and the value of the dispersion function at the place of the device. In 1986, four so called Robinson Wigglers were installed at the PS at CERN. The PS, originally built for proton acceleration, had to serve in the injector chain for the electron / positron runs at LEP. The bare PS lattice was horizontally antidamped for electrons and positrons, therefore the damping had to be altered in order to use PS as a pre-accelerator for LEP. In Fig. 1.4, a picture of one of the RW's at PS is presented.

When changing the damping partition, damping can be transferred between the horizontal (i.e. deflection) and the longitudinal plane. Increasing the damping in the horizontal plane reduces the horizontal emittance of the beam. At the same time,

the damping in the longitudinal plane is reduced, resulting in an increased energy spread of the beam and thus an increased bunch length. Synchrotron light sources are constantly pushing for lower emittance. In recent years, the idea of using a RW in a synchrotron light source in order to reduce the horizontal emittance and increase the brilliance was developed (e.g. SOLEIL (Abualrob et al., 2012)). In general, the minimum average source size is achieved for a damping partition $D = -1$. The emittance is reduced by a factor of 2, whereas the energy spread increases by a factor of $\sqrt{2}$.

At the MLS, another reason for installing such a device is given: the lifetime of the stored beam may be improved considerably. The Touschek lifetime, depending on the particle density inside the bunch, can be improved by increasing the bunch volume. By redistributing the damping to values of D in the order of -1.75, the bunch length can be increased by a factor of 3, whereas the average horizontal bunch width stays constant. A lifetime improvement of more than $100\,\%$ is achievable. Due to the increased energy spread, the horizontal source size in such a setup depends significantly on the value of the dispersion function at the source point. By carefully choosing the accelerator optics so that the dispersion at a given source point is small, the RW may simultaneously increase the brilliance and improve the lifetime. The available installation length for such a RW at the MLS is $1.9\,\mathrm{m}$ in the short straight section (K3) opposite the septum magnet (comp. Fig 1.2).

The necessary accelerator physics and theoretical considerations will be covered in Chapter 2. The RW design for the MLS is derived in Chapter 3. In addition, Chapter 3 features simulations concerning the resulting aperture with RW, the tracking code `FTRACK` used to determine the aperture, and simulations regarding the radiation characteristics of the device. An alternative superconducting design is given at the end of Chapter 3. The effects of the RW on the operation of the machine, including simulations for beam lifetime, emittance, and source sizes, are discussed in Chapter 4. The conclusion is given in Chapter 5.

Accelerator Physics & Theory

In this chapter, the fundamental accelerator physics, relevant for the design and characterisation of a RW for a circular, multi-turn electron accelerator, will be introduced. First, beam dynamics issues will be discussed, followed by remarks on the physics of synchrotron radiation. In a next section, the effects of the emitted synchrotron radiation on the particle beam will be reviewed. Finally, the different beam lifetime contributions and their dependencies on the damping partition will be elaborated.

2.1 Fundamental Accelerator Physics

2.1.1 Reference Frame

It is worthwhile to describe the particle motion in an accelerator with respect to a co-moving reference frame, such as depicted in Fig. 2.1. This Frenet-Serret coordinate system describes the individual particle trajectory with respect to an ideal path $\boldsymbol{r}_0(s)$[1] at azimuthal position s in the accelerator. Three unity vectors are defined (Wiedemann, 2007):

$$\boldsymbol{u}_x(s) \qquad\qquad \text{unit vector } \perp \text{ to trajectory, } \parallel \text{ to } \boldsymbol{r}_0(s) \qquad (2.1)$$

$$\boldsymbol{u}_s(s) = \frac{\mathrm{d}\boldsymbol{r}_0(s)}{\mathrm{d}z} \qquad\qquad \text{unit vector } \parallel \text{ to trajectory}$$

$$\boldsymbol{u}_y(s) = \boldsymbol{u}_s(s) \times \boldsymbol{u}_x(s) \qquad\qquad \text{unit binormal vector.}$$

---

[1]Vector quantities will be printed in bold font in this thesis (e.g. $\boldsymbol{r}$), whereas scalar quantities will be printed in regular font (e.g. s).
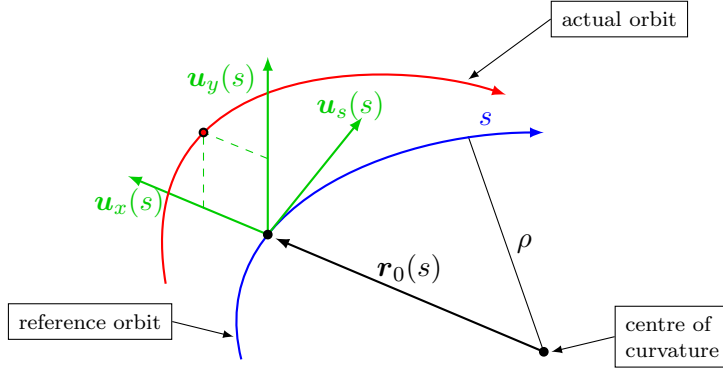
Figure 2.1: Frenet-Serret coordinate system to describe the particle motion in an accelerator with respect to the reference orbit.

The individual particles coordinates are then defined as (all with respect to the reference particle and orbit):

x : the horizontal displacement of the particle in the direction of $\boldsymbol{u}_x(s)$

y : the vertical displacement of the particle in the direction of $\boldsymbol{u}_y(s)$

z : the longitudinal displacement of the particle in the direction of $\boldsymbol{u}_s(s)$,
   $z(s) = s(t) - \beta_0 ct$, where t is the time of flight

x': the horizontal angle defined as the ratio between the horizontal momentum p_x and the reference momentum p_0,
   $x' \equiv \frac{p_x}{p_0}$

y': the vertical angle defined as the ratio between the vertical momentum p_y and the reference momentum p_0,
   $y' \equiv \frac{p_y}{p_0}$

δ : the relative momentum deviation (and $\sim$ relative energy deviation, for $\beta \approx 1$) of the particle with respect to the reference momentum p_0,
   $\delta = \frac{\Delta p}{p_0} = \frac{1}{\beta_0^2} \frac{\Delta E}{E_0} \approx \frac{\Delta E}{E_0}$.

2.1.2 Charged Particle in Electromagnetic Field

The governing force of a charged particle in an electromagnetic field is the Lorentz force:

$$\boldsymbol{F}_L = q\left[\boldsymbol{E} + (\boldsymbol{v} \times \boldsymbol{B})\right], \tag{2.2}$$

where q is the particles charge, $\boldsymbol{v}$ its speed, $\boldsymbol{E}$ is the electric field, and $\boldsymbol{B}$ is the magnetic induction[2]. An accelerator is a 3d particle trap. To guide and to focus the beam, magnetic structures are used. The reason why magnetic fields are used instead of electric fields lies in the occurrence of the speed $\boldsymbol{v}$ in Eq. 2.2. The Lorentz force component of a magnetic field is as high as $F_{L,B} = qvB$, whereas the component due to an electric field is $F_{L,E} = qE$. The speed of the particles is close to the speed of light. Therefore the impact of a magnetic field is much higher than that of an electric field.

In the deflection plane (usually the horizontal plane), the force acting on a particle in a magnetic field is equal to the centrifugal force:

$$
\begin{aligned}
F_L &= F_C, \\
qvB &= \frac{mv^2}{\rho}, \\
\Rightarrow \frac{1}{\rho} &= \frac{q}{p}B,
\end{aligned}
\tag{2.3}
$$

where ρ is the radius of curvature of the trajectory, and $p = mv$ is the particle momentum. The quantity $p/q = B\rho$ is referred to as the beam rigidity (for the MLS: $B\rho = 2.098\,\mathrm{T\,m}$). Assuming deflection in the horizontal plane, a vertical field component of the magnetic field is necessary.

The transverse beam dimensions are usually small compared to the radius of curvature ρ. Therefore, the vertical field component of the magnetic field may be expanded as a Taylor series in the vicinity of the reference trajectory as

$$
\begin{aligned}
\frac{q}{p}B_y &= \frac{1}{B\rho} \cdot \left(\quad B_{y,0} \quad + \quad \frac{\partial B_y}{\partial x}x \quad + \quad \frac{1}{2!}\frac{\partial^2 B_y}{\partial x^2}x^2 \quad + \quad \frac{1}{3!}\frac{\partial^3 B_y}{\partial x^3}x^3 \quad + \dots \right) \\
&= \qquad\quad \frac{1}{\rho} \qquad + \qquad kx \qquad + \qquad \frac{1}{2!}mx^2 \qquad + \qquad \frac{1}{3!}ox^3 \qquad + \dots \\
&\qquad\quad \text{dipole} \qquad \text{quadrupole} \qquad \text{sextupole} \qquad \text{octupole} \quad .
\end{aligned}
\tag{2.4}
$$

The dipole field is used to deflect the beam on a curvature with radius ρ. The quadrupole field is used to focus the beam. Depending on the horizontal (or vertical) displacement of the particle, it experiences a magnetic field that scales linearly with the particles displacement. Therefore, the kick, a particle accumulates in such a quadrupolar field, depends on its initial displacement. The strength of the focussing depends on the gradient of the field. The quantity for the strength of a quadrupole

---

[2]The magnetic induction will also be referred to as the "magnetic field" throughout this thesis.

magnet is k, which is the gradient normalized to the beam rigidity.

As the beam has a certain energy spread, particles experience different focussing from the quadrupolar fields, depending on their energy. To compensate energy dependent focussing, sextupolar fields may be used. In a storage ring or synchrotron all of the mentioned components are installed as dipole, quadrupole, and sextupole magnets. At the MLS also octupole magnets are installed. These may be used to influence higher order non-linear beam dynamics (Feikes et al., 2011).

2.1.3 Transverse Focussing

The transverse focussing is provided by quadrupole magnets (strong focussing) and by dipole magnets (weak focussing). The particle motion can then be described by Hill's equation:

$$x''(s) + \tilde{k}(s)x(s) = 0, \tag{2.5}$$

with

$$\tilde{k}(s) = \frac{1}{\rho(s)^2} - k(s).$$

The negative sign in front of the quadrupole strength $k(s)$ is convention. For electrons, a positive k is focussing in the horizontal plane. Assuming periodicity of the focussing term $k(s)$, the solution to Hill's equation takes the form of a harmonic motion (Wilson, 2001):

$$x(s) = \sqrt{\beta(s)\varepsilon} \cos\left(\phi(s) + \phi_0\right).$$

The phase ϕ and the amplitude $\sqrt{\beta\varepsilon}$ depend on the focussing elements along the azimuth s. Therefore, the "wavelength" of the harmonic motion is varying with s. The constant ε is referred to as the *emittance* of the circulating particle. Multiplying emittance ε by π gives the area of the ellipse in phase space, the particles path encloses. Phase ϕ and amplitude function β are connected through

$$\phi(s) = \int_0^s \frac{\mathrm{d}s'}{\beta(s')}.$$

The amplitude function $\beta(s)$ is usually called "β-function". The phase advance $\Delta\phi$ for one turn is called the *tune*. It is the number of betatron oscillations per

revolution (Wilson, 2001):

$$Q_i = \frac{\Delta\phi_i}{2\pi} = \oint \frac{\mathrm{d}s}{\beta_i(s)}, \tag{2.6}$$

where the subscript i represents either the horizontal or the vertical plane. Horizontal and vertical tune are called the working point of an accelerator. As the focussing of particles depends on their energy, there exists an energy dependent tune shift called *chromaticity* ξ. The following definition for chromaticity will be used in this thesis:

$$\Delta Q_i = \xi_i \cdot \delta. \tag{2.7}$$

The natural chromaticity is the chromaticity of a linear lattice, i.e. a lattice consisting of solely dipoles and quadrupoles. The natural chromaticity of an circular accelerator is negative. It can be compensated and tuned to be small and positive with sextupole magnets which are placed in a dispersive section (see Sec. 2.1.4 for dispersion).

For circulating particle beams, Liouville's theorem states that the area $A = \pi\varepsilon$ of the ellipse in phase space is conserved. In terms of the Twiss (or Courant-Snyder) parameters α, β, and γ, the equation of the ellipse takes the form (Wilson, 2001):

$$\gamma(s)x^2 + 2\alpha(s)xx' + \beta(s)x'^2 = \varepsilon \tag{2.8}$$

with

$$\alpha(s) = -\frac{\beta'(s)}{2},$$
$$\gamma(s) = \frac{1 + \alpha^2(s)}{\beta(s)}.$$

The Courant-Snyder parameters α, β, and γ are periodic with circumference C:

$$\alpha(s) = \alpha(s + C), \quad \beta(s) = \beta(s + C), \quad \gamma(s) = \gamma(s + C). \tag{2.9}$$

The particle density distribution in the transverse planes takes the form of a Gaussian distribution because of the stochastic emission of photons:

$$\rho(x, y) = \frac{Ne}{2\pi\sigma_x\sigma_y} \exp\left(-\frac{x^2}{2\sigma_x^2} - \frac{y^2}{2\sigma_y^2}\right). \tag{2.10}$$

The transverse beam sizes $\sigma_{x/y}$ are defined as one standard deviation of the Gaussian particle distribution. The beam size at azimuth s can be calculated from the β-function and the emittance for a particle at one standard deviation of the coordinate distribution in phase space:

$$\sigma_i(s) = \sqrt{\beta_i(s)\varepsilon_{\mathrm{rms},i}}. \tag{2.11}$$

The emittance corresponding to a particle with an amplitude of one σ in phase space is usually referred to as the "beam emittance" or short "emittance". It is an important property of an accelerator as it impacts e.g. the brilliance of the emitted photon beam. The emittance for electron beams will be discussed in detail in Sec. 2.3, when damping and excitation due to the emission of synchrotron radiation are discussed.

2.1.4 Dispersion and Momentum Compaction

Particles with different energies usually travel on different closed orbits through a circular accelerator. These "dispersive" orbits arise from the different deflection angles in the dipoles, depending on the particles energy deviation. Assuming deflection in the horizontal plane, the equation of motion for an off-momentum particle is given by the inhomogeneous Hill's equation (Wille, 2005):

$$x'' + \frac{1}{\rho^2}x = \frac{1}{\rho}\delta. \tag{2.12}$$

The trajectory corresponding to $\delta = 1$ is defined as the dispersion function $\eta_x(s)$. Inserting η_x into Eq. 2.12 results in

$$\eta_x''(s) + \frac{1}{\rho^2}\eta_x(s) = \frac{1}{\rho}.$$

With the initial conditions at $s = 0$, the solution to the differential equation is (Wille, 2005):

$$\eta_x(s) = \eta_{x,0} \cos \frac{s}{\rho} + \eta_{x,0}'\rho \sin \frac{s}{\rho} + \rho \left(1 - \cos \frac{s}{\rho} \right) \tag{2.13}$$

$$\eta_x'(s) = -\frac{\eta_{x,0}}{\rho} \sin \frac{s}{\rho} + \eta_{x,0}' \cos \frac{s}{\rho} + \sin \frac{s}{\rho}. \tag{2.14}$$

For non-zero values of the dispersion function, off-momentum particles will have an additional dispersive displacement:

$$x(s) = x_\beta(s) + x_\eta(s) = x_\beta(s) + \eta_x(s) \cdot \delta.$$

Off-momentum particles travel on dispersive orbits. These orbits have differing path lengths. Therefore, the length of the path, along which a particle travels, depends on the energy of the particle. The ratio between the relative change in path length $\Delta L/L$ and the corresponding momentum deviation δ is called the "momentum compaction factor" α:

$$\alpha = \frac{\Delta L/L}{\delta}. \tag{2.15}$$

The total path length L can be written as (Wille, 2005):

$$L = L_0 + \Delta L = \oint \frac{\rho + x_\eta}{\rho}\,\mathrm{d}s = \underbrace{\oint \mathrm{d}s}_{L_0} + \underbrace{\delta \cdot \oint \frac{\eta_x(s)}{\rho}\,\mathrm{d}s}_{\Delta L}$$

$$\Rightarrow \alpha = \frac{1}{L_0} \oint \frac{\eta_x(s)}{\rho}\,\mathrm{d}s. \tag{2.16}$$

The momentum compaction factor may be controlled by altering the integrated dispersion function in the dipoles around the ring. For the standard user operation mode at the MLS, the momentum compaction factor is $\alpha = 0.031$. With an integrated dispersion function close to zero, the momentum compaction factor can be made small. As the bunch length depends on the momentum compaction factor, it can be made short by reducing α (Ries, 2014). At the MLS and BESSY II such operation modes exist, called low-α operation (Feikes et al., 2011; Abo-Bakr et al., 2003). In Fig. 1.3b the optical functions for the low-α mode at the MLS are presented. The dispersion function oscillates between positive and negative values and its integral is close to zero.

2.1.5 Beam Size

Because particles with different momenta travel on different orbits, the effective beam size has to be adjusted. In Eq. 2.11, the beam size due to emittance and β-function is presented. It has to be extended to take dispersive effects into account,

resulting in the rms beam size as

$$\sigma_i = \sqrt{\beta_i \cdot \varepsilon_i + \sigma_\delta^2 \cdot \eta_i^2}, \tag{2.17}$$

where σ_δ is the energy spread of the beam. Dispersion exists both in the horizontal and vertical plane. However, in the vertical plane it is usually negligible as long as no vertical bending magnets are in operation. Therefore, in most cases the horizontal and vertical beam size can be expressed as

$$\sigma_x(s) = \sqrt{\beta_x(s) \cdot \varepsilon_x + \sigma_\delta^2 \eta_x^2(s)} \tag{2.18}$$

$$\sigma_y(s) = \sqrt{\beta_y(s) \cdot \varepsilon_y}. \tag{2.19}$$

The vertical emittance ε_y is usually dominated by the horizontal emittance through coupling and alignment errors of magnets. It can be expressed with the coupling parameter κ as:

$$\varepsilon_y \approx \kappa \cdot \varepsilon_x. \tag{2.20}$$

The divergence of the particle beam can be expressed as (Wiedemann, 2007):

$$\sigma_i'(s) = \sqrt{\gamma_i(s)\varepsilon_i + \sigma_\delta^2 \eta_i'^2(s)}. \tag{2.21}$$

With the optical functions for the different operation modes at the MLS (comp. Fig. 1.3), the source sizes and divergences at the individual beam lines can thus be calculated. The results for these calculations in the standard user operation mode are presented in Tab. 4.1 of Chapter 4, where the effects on operation of an installation of a RW are discussed.

2.1.6 Longitudinal Focussing

Longitudinal electric fields are necessary in order to accelerate particles or, in the case of light particles such as electrons or positrons, to store them at a certain energy. These fields accelerate or decelerate the particles while the particles pass through them. The accelerating fields are stored in radio frequency (rf) cavities. A radio frequency signal is generated in e.g. a klystron and is then coupled into the cavity structure in the beam pipe. The resonance frequency of the cavity is an
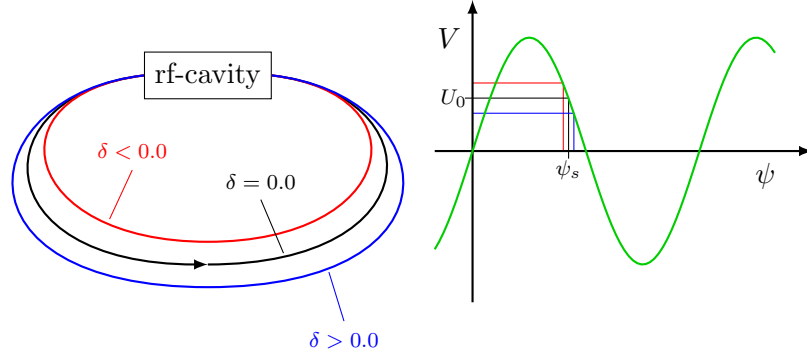
Figure 2.2: Concept of phase focussing for an accelerator above transition.

integer multiple of the revolution frequency f_{rev} of the particles:

$$f_{\text{rf}} = h \cdot f_{\text{rev}},$$

with the integer harmonic number h. The amplitude of the longitudinal electric field E inside the cavity is then oscillating as

$$E(t) = E_0 \cdot \sin(\psi(t)), \tag{2.22}$$

where ψ is the phase of the oscillation. Particles, which arrive at the right point in time at the cavity experience an attractive field which increases their energy, whereas particles arriving at the wrong phase experience a repelling field. Such arises a "bunched" structure of the particle beam: the particle beam is not a continuous one, but the particles are grouped in so called bunches. For protons, where, up to certain energies, effects of synchrotron radiation are negligible, the cavities can be switched off while the protons will still be stably stored in the accelerator. For electrons (or positrons), where synchrotron radiation is not negligible, switching off the cavities would result in a beam loss on the time scale of milli seconds, depending on the damping times.

Apart from restoring or enhancing the energy of the particles, cavities provide phase focussing to the beam: the particles in the beam will have slightly different energies and will travel on different paths through the accelerator. Due to the centrifugal force, particles with positive momentum deviation ($\delta > 0$) will travel a longer path through the accelerator than particles with negative momentum deviation ($\delta < 0$)[3]. For ultra relativistic particles, above transition, the speed of the particles is $v \approx c$. The change in energy is higher than the corresponding change in

---

[3]Assuming positive momentum compaction.

velocity. Therefore, the high energy particles will arrive later at the cavity than low energy particles (comp. Fig. 2.2). Hence, they experience a weaker field than the low energy particles and get less accelerated.

This leads to an oscillation around the reference energy with a frequency called the synchrotron frequency f_s. It can be calculated as (Wiedemann, 2007):

$$f_s^2 = f_{\text{rev}}^2 \frac{h\eta_c e V_{\text{rf}} \cos\psi_s}{2\pi\beta E_0}, \tag{2.23}$$

where V_{rf} is the amplitude of the rf-voltage, f_{rev} is the revolution frequency, h is the harmonic number, which is the number of rf-oscillations per revolution, ($h = 80$ for the MLS), and $\eta_c = \alpha - \frac{1}{\gamma^2}$ is the phase slip factor with α being the momentum compaction factor (see Sec. 2.1.4). For the MLS in standard user operation mode, with $V_{\text{rf}} = 500\,\text{kV}$ and $\eta_c \approx \alpha = 0.031$, the synchrotron frequency is $f_{s,\text{SU}} = 110.6\,\text{kHz}$.

By detuning the rf-frequency from its reference frequency, it is possible to introduce momentum deviation δ to the beam to study for example the natural chromaticity of the beam. A change Δf of the rf-frequency alters the revolution time for the closed orbit. Assuming positive momentum compaction factor, positive Δf shortens the reference orbit. Due to phase focussing, the reference energy reduces to adjust to the new orbit. For negative Δf the reference orbit is lengthened, leading to an increased reference energy. The revolution time in terms of the rf-frequency f_{rf} is

$$T_0 = \frac{1}{f_{\text{rev}}} = \frac{h}{f_{\text{rf}}}.$$

The change in revolution time due to Δf is

$$\Delta T = (T_0 + \Delta T) - T_0 = \frac{h}{f_{\text{rf}} + \Delta f} - \frac{h}{f_{\text{rf}}}.$$

The orbit length is given by $L \approx c \cdot T$. Substituting ΔL and L in Eq. 2.16 results in

$$\frac{\Delta L}{L} = \frac{c\left(\frac{h}{f_{\text{rf}} + \Delta f} - \frac{h}{f_{\text{rf}}}\right)}{c \cdot \frac{h}{f_{\text{rf}}}} = \frac{f_{\text{rf}}}{f_{\text{rf}} + \Delta f} - 1 = \alpha \cdot \delta. \tag{2.24}$$

Finally Δf can be expressed in terms of the relative momentum deviation δ:

$$\Delta f = -\frac{\alpha\delta f_{\text{rf}}}{\alpha\delta + 1} \approx -\alpha\delta f_{\text{rf}}. \tag{2.25}$$

For the MLS, a momentum deviation of e.g. $1\,\text{‰}$ is achieved by altering the rf-frequency by $\Delta f = -14.99\,\text{kHz}$.

2.1.7 Matrix Formalism

Each lattice element and groups of lattice elements may be approximated by a transfer matrix. Equation 2.5 has solutions which can be tracked from one azimuthal position s_i to another azimuthal position s_f by a 2×2 transport matrix (Wilson, 2001):

$$\begin{pmatrix} x(s_f) \\ x'(s_f) \end{pmatrix} = \begin{pmatrix} a & b \\ c & d \end{pmatrix} \cdot \begin{pmatrix} x(s_i) \\ x'(s_i) \end{pmatrix} = \boldsymbol{M}_{fi} \cdot \begin{pmatrix} x(s_i) \\ x'(s_i) \end{pmatrix}. \tag{2.26}$$

The matrix elements can be identified in terms of the optical functions α, β, and γ in Eq. 2.8. The result is the so call Twiss matrix (Wilson, 2001):

$$\boldsymbol{M} = \begin{pmatrix} \cos(\phi) + \alpha \sin(\phi) & \beta \sin(\phi) \\ -\gamma \sin(\phi) & \cos(\phi) - \alpha \sin(\phi) \end{pmatrix}. \tag{2.27}$$

To perform 6d particle tracking, accelerator elements are described by transport matrices. In (Brown, 1968) a first and second order matrix theory is presented. The particles coordinates $x_k(s_f)$ at azimuthal position s_f are expressed in terms of a linear 6×6 transport matrix $\boldsymbol{R}$, a second order matrix $\boldsymbol{T}$ and the particles initial coordinates $x_l(s_i)$ as:

$$x_k(s_f) = \sum_{l=1}^{6} R_{kl} x_l(s_i) + \sum_{l=1}^{6} \sum_{m=l}^{6} T_{klm} x_l(s_i) x_m(s_i), \tag{2.28}$$

with $x_1 = x$, $x_2 = x'$, $x_3 = y$, $x_4 = y'$, $x_5 = z$, $x_6 = \delta$. The transfer matrix elements R_{21} and R_{43} describe the focussing characteristics of an element in the horizontal and vertical plane respectively.

2.2 Generation of Synchrotron Radiation

Relativistic charged particles undergoing acceleration emit synchrotron radiation. The power emitted by an ultra-relativistic particle ($v \approx c$) is given by (Wilson, 2001):

$$P_\gamma = \frac{1}{6\pi\varepsilon_0} \frac{e^2 a^2}{c^3} \cdot \gamma^4. \tag{2.29}$$

Apart from constants, a is the acceleration and γ Lorentz' factor. The acceleration a in the longitudinal plane due to the rf-system is small compared to the transverse acceleration in the dipole magnets. Here $a = v^2/\rho$ and

$$P_\gamma = \frac{1}{6\pi\varepsilon_0} \frac{e^2 c}{\rho^2} \cdot \gamma^4 = \frac{2}{3} \frac{r_e c}{(m_0 c^2)^3} \frac{E^4}{\rho^2}. \tag{2.30}$$

As the emitted power scales with the relativistic factor γ, it becomes clear why light particles like electrons emit much more radiation than heavy particles like protons. The power scales rapidly with the energy of the particles. The power lost per turn of a particle and which has to be fed back by the rf-system is (Wilson, 2001):

$$U_0 = \frac{4}{3}\pi \frac{r_e}{(m_0 c^2)^3} \frac{E^4}{\rho} \stackrel{\text{\tiny MLS}}{=} 9.062\,\text{keV}. \tag{2.31}$$

For high energy lepton rings like LEP with an electron energy of $100\,\text{GeV}$, the power lost per turn was as high as $2.9\,\text{GeV}$. However, Eq. 2.31 only includes the power radiated by the deflecting bending magnets, it does not include power radiated by ID's (Sec. 2.2.2).

2.2.1 Bending Magnet Radiation

The spectrum of photons emitted by electrons in a bending field is characterized by the critical photon energy of the spectrum (Clarke, 2004):

$$E_c = \hbar\omega_c = \frac{3}{2}\frac{\hbar c\gamma^3}{\rho} \stackrel{\text{\tiny MLS}}{=} 361\,\text{eV}. \tag{2.32}$$

E_c divides the spectrum into two half-spectra which both emit the same power. The emitted power for photon energies smaller than E_c and the emitted power for photon energies greater than E_c are equal. The maximum spectral flux is found for photon energies of approximately $E = 0.25E_c$. In Fig. 2.3, the dipole radiation spectrum of
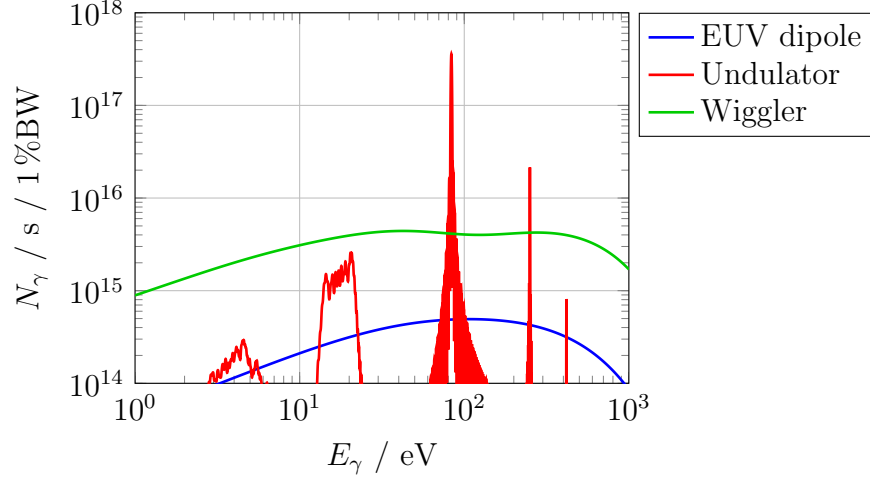
Figure 2.3: Dipole radiation at the EUV-beamline at MLS compared to example wiggler and undulator radiation. All calculations for MLS beam parameters and for the acceptance at the EUV-beamline (87 mm hor., 40 mm ver., distance 5 m). ID radiation calculated with `WAVE` (Scheer, 2012). Undulator: $K = 0.5$, $\lambda_{\mathrm{ID}} = 4\,\mathrm{cm}$, 50 periods. Wiggler: $K = 40.0$, $\lambda_{\mathrm{ID}} = 30\,\mathrm{cm}$, 6 periods.

a bending magnet at the MLS with the acceptance given by the EUV-beamline is depicted (blue).

2.2.2 Insertion Device Radiation

3rd generation light sources are characterized by the employment of insertion devices in the straight sections between the deflecting dipoles. ID's usually consist of a sequence of multiple bending magnets, where the particles are sent on an alternating orbit. Within each bend, radiation is emitted. Depending on the deflection parameter K, the emitted radiation overlaps and interference effects occur. The deflection parameter is calculated as (Clarke, 2004):

$$K = \frac{eB_0 \lambda_{\mathrm{ID}}}{2\pi mc} \approx 93.37\,\mathrm{T}^{-1}\,\mathrm{m}^{-1} \cdot B_0 \lambda_{\mathrm{ID}}. \tag{2.33}$$

B_0 is the peak magnetic field and λ_{ID} is the period length of the magnetic structure of the ID. For values of K smaller than 1, the electron trajectories overlap with the emitted radiation fan ($\sim 1/\gamma$) and interference effects occur. For $K \gg 1$, little overlap is present and the poles can be treated as independent, bend-like sources (Clarke, 2004).

An ID with K smaller than 1 is referred to as an *undulator*, whereas an ID with $K \gg 1$ is called a *wiggler*. The boundary between undulator and wiggler regime is

soft as also for $K > 1$ interference effects occur for longer wavelengths.

The spectrum of a wiggler is characterized by the critical photon energy E_c in Eq. 2.32. However, due to the varying field inside the wiggler, the spectrum alters, depending on the observation angle. The spectrum of a wiggler is the sum of the spectra of the individual poles. In Fig. 2.3, a spectrum of a fictional wiggler is presented (green). The wiggler has the same on-axis peak field as the bending magnet ($B_0 = 1.37\,\mathrm{T}$). The number of poles was set to 13, which results in 13 times the intensity of the EUV-dipole (blue). The dip in the wiggler spectrum at $\sim 100\,\mathrm{eV}$ is due to the vertical acceptance of the beamline.

The spectrum of an undulator is characterized by the wavelengths of the undulator harmonics (Clarke, 2004):

$$\lambda_n = \frac{\lambda_{\mathrm{ID}}}{2n\gamma^2}\left(1 + \frac{K^2}{2} + \theta^2\gamma^2\right), \tag{2.34}$$

where λ_{ID} is the period length of the device, θ the observation angle ($\theta = 0$ for $x = 0$), and n the order of the harmonic of wavelength λ_n. Due to interference effects, the intensity of some wavelengths is enhanced, whereas in between these wavelengths dark regions occur. In Fig. 2.3, a typical undulator spectrum for $K = 0.5$ of a fictional undulator is depicted (red). The wavelength of the first undulator harmonic is calculated to be $\lambda_1 = 14.85\,\mathrm{nm}$, which corresponds to a photon energy of $E_{\gamma,1} = 83.50\,\mathrm{eV}$.

Comparing the spectra for bending magnet radiation with the spectra for ID radiation in Fig. 2.3 it becomes clear that todays 3rd generation synchrotron light sources focus on ID's as their main radiation sources. The flux obtained by undulators are about 3 orders of magnitude higher for selected wavelengths than those obtained by the bending magnets.

2.3 Effects of Synchrotron Radiation

The emission of synchrotron radiation is not only useful for the scientist conducting experiments, but has different effects on the particle beam itself. For a detailed review on effects of synchrotron radiation, the reader is referred to (Wolski, 2014). Here, a brief version is presented.

2.3.1 Radiation Damping and Quantum Excitation

In an electron storage ring, radiation damping and quantum excitation occur. Both effects are related to the emission of synchrotron radiation. If a stored particle emits a photon, it emits the photon in flight direction. The particle loses mainly longitudinal momentum, but also a small fraction transverse momentum. The momentum is restored in the rf-cavity. However, in the cavity only the longitudinal momentum is restored. Therefore, transverse momentum is carried away through the interplay between emission of radiation and longitudinal acceleration in the cavity. Thus, the transverse betatron oscillations are damped.

Due to synchrotron radiation not only damping but also excitation arises. In the case of finite dispersion at the place of the photon emission, the reference orbit jumps to a new transverse position according to the momentum lost to the photon. The particle therefore performs betatron oscillations around its new reference orbit. This corresponds to a "heating" of betatron oscillations (Wolski, 2014).

Radiation damping and quantum excitation result in an equilibrium state which defines emittances (Eq. 2.53) and the energy spread (Eq. 2.61) of the beam. The damping and excitation characteristics of an accelerator can be described in terms of the synchrotron radiation integrals presented in the following section.

2.3.2 Synchrotron Radiation Integrals

The synchrotron radiation integrals are defined as (Wolski, 2013):

$$I_1 = \oint \frac{\eta_x}{\rho}\,\mathrm{d}s \qquad \overset{\mathrm{MLS}}{\approx} 1.64\,\mathrm{m}, \tag{2.35}$$

$$I_2 = \oint \frac{1}{\rho^2}\,\mathrm{d}s \qquad \overset{\mathrm{MLS}}{\approx} 4.11\,\mathrm{m}^{-1}, \tag{2.36}$$

$$I_3 = \oint \frac{1}{|\rho|^3}\,\mathrm{d}s \qquad \overset{\mathrm{MLS}}{\approx} 2.69\,\mathrm{m}^{-2}, \tag{2.37}$$

$$I_4 = \oint \frac{\eta_x}{\rho}\left(\frac{1}{\rho^2} + 2k_1\right)\,\mathrm{d}s \qquad \overset{\mathrm{MLS}}{\approx} -0.23\,\mathrm{m}^{-1}, \tag{2.38}$$

$$I_5 = \oint \frac{\mathscr{H}_x}{|\rho|^3}\,\mathrm{d}s \qquad \overset{\mathrm{MLS}}{\approx} 0.88\,\mathrm{m}^{-1}, \tag{2.39}$$

with

$$k_1 = \frac{e}{p_0}\frac{\partial B_y}{\partial x} = \frac{1}{B\rho}\frac{\partial B_y}{\partial x},$$

$$\mathscr{H}_x = \gamma_x \eta_x^2 + 2\alpha_x \eta_x \eta_x' + \beta_x \eta_x'^2.$$

The evaluation of the synchrotron radiation integrals was conducted for the MLS in standard user operation mode according to (Helm et al., 1973).

The first synchrotron radiation integral is not directly connected to radiation effects, but can be associated with the definition of the momentum compaction factor α in Eq. 2.16:

$$\alpha = \frac{1}{L_0} \oint \frac{\eta_x(s)}{\rho} \, \mathrm{d}s = \frac{1}{L_0} \cdot I_1. \tag{2.40}$$

In Equation 2.31, the energy loss per turn was calculated by integrating the emitted power (Eq. 2.30) over all dipoles assuming no other devices in which photons are emitted. More generally, the energy loss per turn for a reference particle can be found by integrating the radiation power along the reference trajectory around the ring (Wolski, 2013):

$$U_0 = \oint P_\gamma \, \mathrm{d}t \approx \oint P_\gamma \frac{\mathrm{d}s}{c}.$$

P_γ in Eq. 2.30 can be rewritten as:

$$P_\gamma = \frac{C_\gamma c}{2\pi} \cdot \frac{c^4 p^4}{\rho^2} \approx \frac{C_\gamma c}{2\pi} \cdot \frac{E^4}{\rho^2}. \tag{2.41}$$

C_γ is called the "radiation constant" with

$$C_\gamma = \frac{q^2}{3\epsilon_0 (mc^2)^4} \overset{e^-}{\approx} 8.846 \times 10^{-5} \, \mathrm{m \, GeV^{-3}}. \tag{2.42}$$

The radiation loss per turn of the reference particle can now be expressed in terms of I_2 (Wolski, 2013):

$$U_0 \approx \frac{C_\gamma}{2\pi} E_0^4 \cdot I_2. \tag{2.43}$$

The synchrotron radiation integrals three, four, and five, are derived alongside with the equilibrium emittance and energy spread: The emittance ε_x can be defined as the average horizontal action $\langle J_x \rangle$ of all particles in the bunch in terms of the Courant-Snyder parameters (Eq. 2.8) (Wolski, 2013):

$$\varepsilon_x = \langle J_x \rangle, \tag{2.44}$$

with

$$2J_x = \gamma_x x^2 + 2\alpha_x x x' + \beta_x x'^2. \tag{2.45}$$

The average damping rate of horizontal action can be expressed in terms of the emitted power, being the source of radiation damping (a detailed derivation is found in (Wolski, 2013)):

$$\frac{\mathrm{d}J_x}{\mathrm{d}t} = -\frac{1}{T_0} \oint w_1 \frac{P_\gamma}{pc} \, \mathrm{d}t, \tag{2.46}$$

with

$$w_1 = \alpha_x x x' + \beta_x x'^2 - \eta_x(\gamma_x x + \alpha_x x') - \eta_x'(\alpha_x x + \beta_x x').$$

Substituting $\mathrm{d}t$ with a more convenient dependency on $\mathrm{d}s$ and keeping in mind curvatures:

$$\mathrm{d}t = \frac{\mathrm{d}C}{c} = \left(1 + \frac{x}{\rho}\right) \frac{\mathrm{d}s}{c},$$

where C is the circumference. Considering a variation of the dipole field such that

$$B = B_0 + x \frac{\partial B}{\partial x},$$

and substituting $1/\rho = B/B\rho$ in the expression for the emitted power P_γ in Eq. 2.41 results in:

$$\oint \left\langle w_1 P_\gamma \left(1 + \frac{x}{\rho}\right) \right\rangle \, \mathrm{d}s = cU_0 \left(1 - \frac{I_4}{I_2}\right) \varepsilon_x. \tag{2.47}$$

The damping of the horizontal emittance in a purely classical model can now be expressed as (Wolski, 2013):

$$\frac{\mathrm{d}\varepsilon_x}{\mathrm{d}t} = -\frac{1}{T_0} \frac{U_0}{E_0} \left(1 - \frac{I_4}{I_2}\right) \varepsilon_x = -\frac{2}{\tau_x} \varepsilon_x. \tag{2.48}$$

Here, τ_x is the horizontal damping time defined with the horizontal damping parti-

tion number j_x as

$$\tau_x = \frac{2}{j_x}\frac{E_0}{U_0}T_0, \tag{2.49}$$

$$j_x = 1 - \frac{I_4}{I_2}. \tag{2.50}$$

In analogy to the damping rate, a growth rate of the emittance due to quantum excitation can be derived. The difference in the derivation is that not a classical model is used as in the derivation of the damping rate, but a quantum model, where photons are emitted in distinct quanta. The evolution of the horizontal emittance can be derived to be (Wolski, 2013):

$$\frac{\mathrm{d}\varepsilon_x}{\mathrm{d}t} = -\frac{2}{\tau_x}\varepsilon_x + \frac{2}{j_x\tau_x}C_q\gamma^2\frac{I_5}{I_2}. \tag{2.51}$$

C_q is the "quantum constant" with

$$C_q = \frac{55}{32\sqrt{3}}\frac{\hbar}{mc}\overset{e^-}{\approx} 3.832 \times 10^{-13}\,\mathrm{m}. \tag{2.52}$$

With the condition

$$\frac{\mathrm{d}\varepsilon_x}{\mathrm{d}t} = 0,$$

the equilibrium emittance is found to be (Wolski, 2013):

$$\varepsilon_{x,0} = C_q\gamma^2\frac{I_5}{j_xI_2}. \tag{2.53}$$

Not only the transverse planes are affected by radiation damping and excitation but also the longitudinal plane. The change in energy deviation δ and longitudinal coordinate z of a particle in one turn can be expressed as (Wolski, 2013):

$$\Delta\delta = \frac{qV_{\mathrm{rf}}}{E_0}\sin\left(\psi_s - \frac{f_{\mathrm{rf}}z}{c}\right) - \frac{U}{E_0}, \tag{2.54}$$

$$\Delta z = -\alpha C_0\delta, \tag{2.55}$$

where U is the energy lost per turn of the particle, which is not necessarily equal to U_0. Taking the time derivative of $\Delta\delta$ results in

$$\frac{\mathrm{d}\delta}{\mathrm{d}t} = \frac{qV_{\mathrm{rf}}}{E_0T_0}\sin\left(\psi_s - \frac{f_{\mathrm{rf}}z}{c}\right) - \frac{U}{E_0T_0}.$$

$-U/E_0 T_0$ is a damping term of the momentum deviation δ. The synchrotron radiation power by the particle depends on the energy deviation of the particle. In first order of δ, U can be expressed as (Wolski, 2013):

$$U = U_0 + E_0 \delta \left. \frac{\mathrm{d}U}{\mathrm{d}E} \right|_{E=E_0}. \tag{2.56}$$

With

$$\mathrm{d}t = \frac{\mathrm{d}C}{c} = \frac{1}{c}\left(1 + \frac{x}{\rho}\right)\,\mathrm{d}s = \frac{1}{c}\left(1 + \frac{\eta_x \delta}{\rho}\right)\,\mathrm{d}s,$$

the energy loss per turn is

$$U = \frac{1}{c}\oint P_\gamma \left(1 + \frac{\eta_x \delta}{\rho}\right)\,\mathrm{d}s. \tag{2.57}$$

It follows in terms of I_4 and I_2:

$$\left. \frac{\mathrm{d}U}{\mathrm{d}E} \right|_{E=E_0} = \left(2 + \frac{I_4}{I_2}\right)\frac{U_0}{E_0} = j_s \frac{U_0}{E_0}, \tag{2.58}$$

with the longitudinal damping partition number

$$j_s = 2 + \frac{I_4}{I_2}. \tag{2.59}$$

According to the horizontal plane, a longitudinal damping time is defined as

$$\tau_s = \frac{2}{j_s}\frac{E_0}{U_0}T_0. \tag{2.60}$$

Considering the quantum excitation for the longitudinal plane, results in an equilibrium energy spread of the beam as (Wolski, 2013):

$$\sigma_\delta^2 = C_q \gamma^2 \frac{I_3}{j_s I_2}. \tag{2.61}$$

The bunch length σ_s can now be calculated from the energy spread, the momentum compaction factor α and the synchrotron frequency f_s:

$$\sigma_s = \frac{\alpha c}{2\pi f_s}\sigma_\delta\,[\mathrm{m}] = \frac{\alpha}{2\pi f_s}\sigma_\delta\,[\mathrm{s}]. \tag{2.62}$$

2.3.3 Damping Partition

As derived above, in the case of no vertical dispersion and coupling, horizontal and longitudinal damping are connected. The damping partition numbers in all three planes can be written as:

$$j_x = 1 - \frac{I_4}{I_2}, \quad j_y = 1, \quad j_s = 2 + \frac{I_4}{I_2}. \tag{2.63}$$

The damping partition numbers obey Robinson's damping theorem (Robinson, 1958):

$$j_x + j_y + j_s = 4. \tag{2.64}$$

Although it is possible to shift damping between the individual planes, the overall damping is conserved. The ratio between I_4 and I_2 is called the damping partition D:

$$D \equiv \frac{I_4}{I_2}. \tag{2.65}$$

The damping times in all three planes are given as:

$$\tau_x = \frac{2}{j_x} \frac{E_0}{U_0} T_0, \quad \tau_y = \frac{2}{j_y} \frac{E_0}{U_0} T_0, \quad \tau_s = \frac{2}{j_s} \frac{E_0}{U_0} T_0, \quad \frac{2E_0}{U_0} T_0 \overset{\mathrm{MLS}}{=} 22.21 \,\mathrm{ms}. \tag{2.66}$$

In terms of the damping partition D, emittance ε_x and energy spread σ_δ can be written as:

$$\varepsilon_x(D) = C_q \gamma^2 \frac{I_5}{I_2} \frac{1}{1-D} = \varepsilon_{x,0} \cdot \frac{1}{1-D}, \tag{2.67}$$

$$\sigma_\delta^2(D) = C_q \gamma^2 \frac{I_3}{I_2} \frac{1}{2+D} = \sigma_{\delta,0}^2 \cdot \frac{2}{2+D}, \tag{2.68}$$

with $\varepsilon_{x,0} = \varepsilon_x(D = 0)$ and $\sigma_{\delta,0} = \sigma_\delta(D = 0)$. Because of the coupling between horizontal and longitudinal damping, it is possible to transfer damping between the two planes. Emittance and energy spread can therefore be altered such that emittance reduces with increasing energy spread and vice versa. In Fig. 2.4, the evolution of emittance and energy spread as a function of the damping partition D is depicted. For the energy spread, a singularity occurs for $D = -2$, whereas for the emittance, a singularity occurs for $D = 1$.
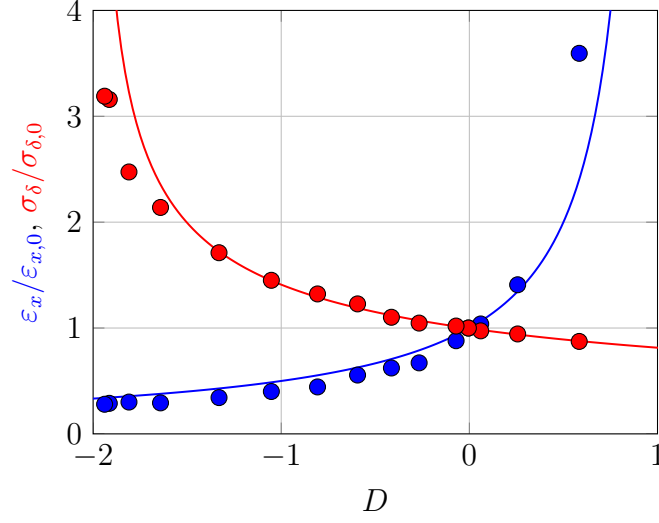
Figure 2.4: Evolution of emittance ε_x and energy spread σ_δ, normalized to values for $D = 0$, as a function of the damping partition D. Theoretical functionality is presented by solid lines, whereas tracked results are marked with circles. Single particle tracking was performed with `MAD-X-PTC`.

2.3.4 Controlling the Damping Partition with Combined Function Magnets

In I_4 occurs the product of a dipole field B_y, a gradient to that field $k_1 = \frac{1}{B\rho}\frac{\partial B_y}{\partial x}$, and the dispersion function η_x (comp. Eq. 2.38):

$$
\begin{aligned}
I_4 &= \oint \frac{\eta_x}{\rho}\left(\frac{1}{\rho^2} + 2k_1\right)\, \mathrm{d}s = \oint \left(\frac{\eta_x}{\rho^3} + 2\frac{\eta_x k_1}{\rho}\right)\, \mathrm{d}s \\
&= \oint \left(\frac{\eta_x}{\rho^3} + \frac{2}{(B\rho)^2}\cdot \eta_x B_y \frac{\partial B_y}{\partial x}\right)\, \mathrm{d}s.
\end{aligned}
$$

This product is zero when no combined function magnets are in operation. The damping partition D, which is the ratio between I_4 and I_2, can be manipulated with the introduction of such a non-zero product

$$
\eta_x \cdot B_y \cdot \frac{\partial B_y}{\partial x} \neq 0.
$$

In order to alter the damping partition D to negative values, the product has to be negative too. Therefore, the device, which is used to manipulate D, has to be placed in a dispersive section of the accelerator. Furthermore, the device needs to induce a field and a gradient whose product is negative, assuming positive dispersion. Such a product is given for a device whose absolute value of the field reduces with increasing
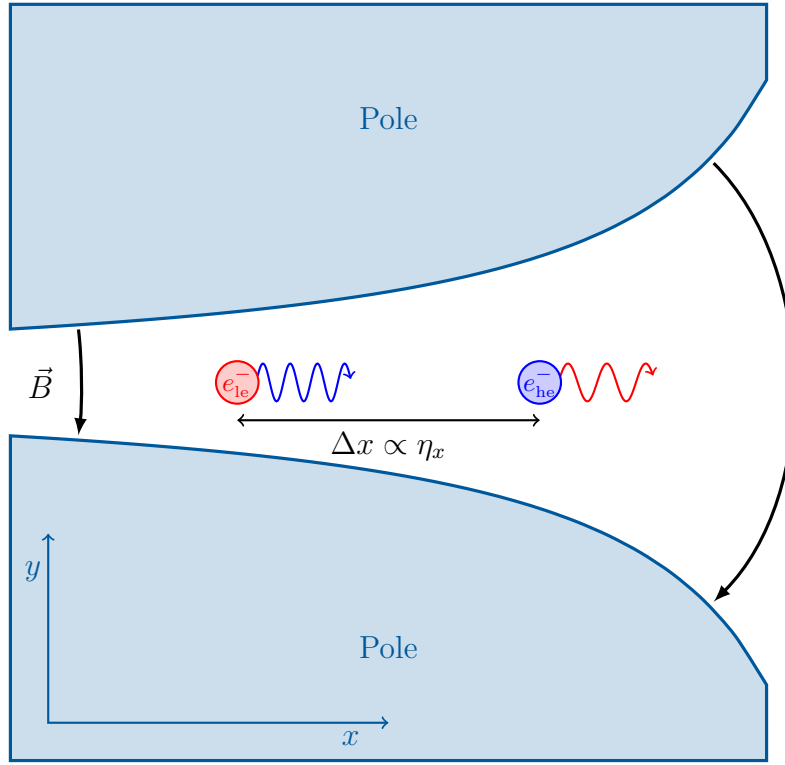
Figure 2.5: Function principle of the RW.

horizontal amplitude x.

The RW is a sequence of alternating combined function magnets. A simplified view on the function principle of the RW is as follows (comp. Fig. 2.5):

- the dispersion sorts the particles according to their energy, with $x \propto \eta_x \cdot \delta$,

- due to the gradient in the field, high energy particles experience a weaker field than low energy particles,

- high energy particles, experiencing a weaker field, radiate less power than low energy particles, according to Eq. 2.32, $E_{\gamma,c} \propto B_0$, [4]

- therefore, high energy particles lose less energy than low energy particles,

---

[4]One may argue that the critical photon energy is also proportional to the cube of the Lorentz factor in Eq. 2.32. A quick calculation example to show that B_0 is the dominant part here: Assuming two electrons with an energy deviation of $\pm 1\%$ of the reference energy $629\,\text{MeV}$ (Lorentz factor $\gamma = 1231$). These electrons are sorted according to a dispersion function of value $\eta_x = 1.0\,\text{m}$ in a field with on-axis dipole component $B_y = 1.0\,\text{T}$ and gradient $\partial B_y/\partial x = -14\,\text{T\,m}^{-1}$. The high energy electron ($\gamma = 1243$) experiences a magnetic field of $0.86\,\text{T}$, whereas the low energy electron ($\gamma = 1219$) experiences a field of $1.14\,\text{T}$. Calculating the product of $\gamma^3 \cdot B_y$ for both electrons results in $2.06 \times 10^9\,\text{T}$ for the low energy electron and $1.65 \times 10^9\,\text{T}$ for the high energy electron. Therefore, the impact of B on the radiated power is stronger than the impact of the cube of γ in this regime.

(a)   (b)
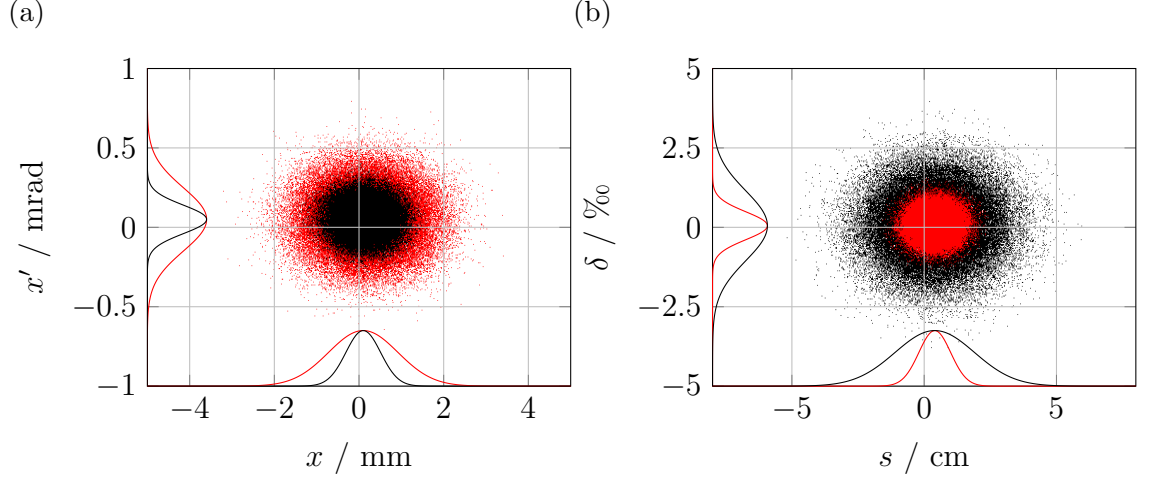
Figure 2.6: Tracked horizontal (a) and longitudinal (b) phase space for the MLS without (red) and with RW (black), corresponding to $D = -0.055$ (red) and $D = -1.75$ (black) respectively. For further visualization, the fitted normalized Gaussian distributions for the individual coordinates are indicated at the respective axes.

resulting in an increased energy spread.

The overall damping of the accelerator is conserved because the amount of radiation (including the additional radiation of the RW), being the source of the damping, is conserved. Therefore, as the energy spread increases, the horizontal emittance decreases as part of the damping is transferred from the longitudinal to the horizontal plane. In Fig. 2.6, the horizontal and longitudinal phase space, tracked with `MAD-X-PTC`, for $D = -0.055$, which is the damping partition for the MLS lattice, and $D = -1.75$, corresponding to the MLS with RW, is presented. The phase space was tracked at the septum, where the value of the dispersion function is zero. With the transition from $D = -0.055$, corresponding to the colour red, to $D = -1.75$, corresponding to the colour black, the distribution of the horizontal position of the particle shrinks. In contrast, the distribution for the energy deviation, and the longitudinal position, of the particle increase, as is shown in Fig. 2.6b. Thus, by altering the damping partition, the bunches can be made more slim in the horizontal plane, while they are lengthened in the longitudinal plane.

Tracking of Damping Effects with `MAD-X-PTC`

In order to study the damping effects of the RW, the RW was modelled in `MAD-X-PTC` by a sequence of misaligned quadrupoles. Longitudinal field components between the poles are not included in such a simplified model. As the longitudinal field com-

ponents do not contribute to the damping redistribution, the simplified model is sufficient to study damping effects. However, in order to study effects on the dynamic aperture, this approach is not sufficient. To study effects on the dynamic aperture the program `FTRACK` was developed and is presented in Sec. 3.4.1.

Single particle tracking was performed for 1×10^8 turns each, corresponding to ~ 1400 longitudinal damping times for $D = -0.055$ and ~ 180 longitudinal damping times for $D = -1.75$. The resulting phase space distribution was used to extract the emittance and the energy spread. The RW was modelled by a set of misaligned quadrupoles, together with a set of horizontal kickers between the quadrupoles in order to compensate the ponderomotive drift (comp. Sec. 3.2.3). In Fig. 2.4, the emittance and the energy spread together with the theoretical predictions as a function of the damping partition are presented. Minor deviations from the theoretical predictions are due to the varying matched optical functions for the different values of D.

Measurement of Damping Effects at the MLS

In a separate function lattice, the fourth synchrotron radiation integral I_4 can be altered in a limited range by steering the beam off-axis in quadrupole magnets. Thus, a dipole field component is added on top of the quadrupole gradient. In first order approximation, the change in I_4 from a single quadrupole is:

$$\Delta I_4 \approx 2 \cdot \eta_x(s_q) \cdot l_q \cdot k_q^2 \cdot \Delta x_{\text{beam}}. \tag{2.69}$$

Here, Δx_{beam} is the horizontal displacement of the beam inside the quadrupole at azimuthal position s_q, of strength k_q, and length l_q. The change in I_2 by the additional dipole fields is neglected here as they are assumed to be small compared to the contribution of the remaining dipoles.

Such an experiment was conducted in the standard user operation mode at the MLS. The horizontal displacement of the beam was set up by using the horizontal corrector magnets and by readjusting the rf-frequency. The achieved displacement was approximately $\pm 10 \, \text{mm}$ in the entire machine. The beam position monitors

Table 2.1: Expected and measured changes in bunch length via off centered orbit.

Δx_{beam} / mm	$\Delta \sigma_{s,\text{theo}}/\%$	$\Delta \sigma_{s,\text{meas}}/\%$
10	$-3.9(7)$	$-3.8(7)$
-10	$4.6(10)$	$3.5(7)$

were not able to measure the beam position precisely for these high amplitudes. The beam position had to be estimated from smaller displacements and by scaling the applied orbit bump. Each quadrupole, independent of the polarity, contributed to changing I_4. The impact of each individual quadrupole depends on the value of the dispersion function at the quadrupoles azimuthal position.

As the bunch length is proportional to the energy spread, the relative change in energy spread is equal to the one in bunch length. Therefore, the relative change in energy spread can be deduced by measuring the bunch length. The bunch length can be measured with a streak camera at the MLS ((Hamamatsu, 2010), resolution $\sim 100\,\text{fs}$). In Tab. 2.1, the expected and measured relative changes in bunch length are presented. The uncertainty of the orbit displacement was assumed to be $\sigma_{\Delta x} = \pm 0.5\,\text{mm}$. The error introduced by the streak camera was assumed to be $\sigma_\sigma = \pm 0.1\,\text{ps}$. The reference bunch length for zero orbit displacement was measured to be $\sigma_s = 20.75\,\text{ps}$. The results agree within the boundaries given by the uncertainties and show that damping effects cannot only be calculated, but also measured in existing separated function accelerators.

2.4 Beam Lifetime

The number of stored particles in an accelerator is steadily decreasing because particles might hit the aperture limit due to a scattering process, a resonance driven high amplitude, or because the particles energy at some point does not comply with the reference energy defined by the bending magnets. Either way, the particle beam is decaying with time and therefore a beam lifetime[5] can be defined as the time in which the stored initial current I_0 decays to I_0/e [6](Bocchetta, 1996). The stored beam current I decays with time following an exponential function as

$$I(t) = I_0 \cdot \exp\left(-\frac{t}{\tau(I)}\right), \tag{2.70}$$

where I_0 is the initially stored current at time $t = 0$ and $\tau(I)$ is the beam lifetime. The lifetime is current dependent and can locally be determined with approximating

$$\tau(I) \approx \frac{\Delta t}{\Delta I} \cdot \langle I \rangle. \tag{2.71}$$

---

[5]This lifetime is not to be confused with e.g. the half lifetime of an unstable isotope.
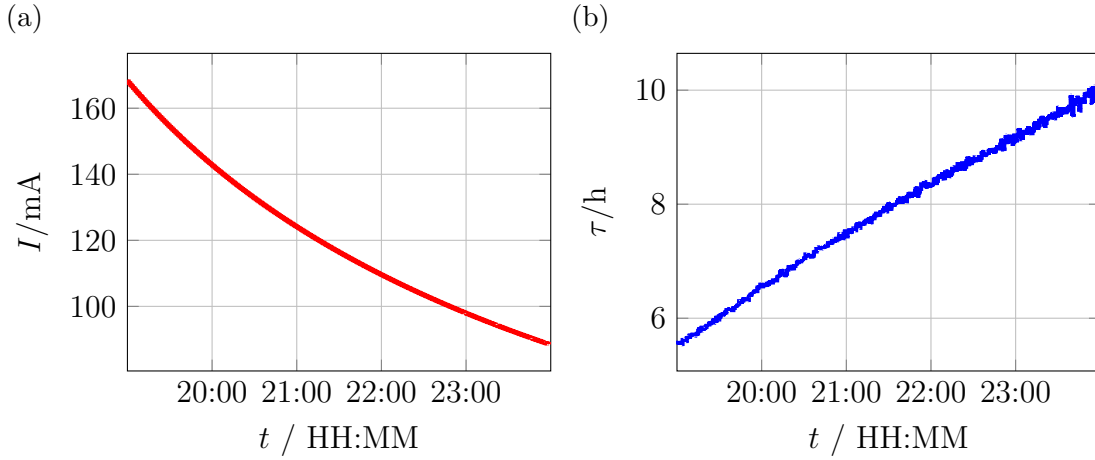[6]Here, e is Euler's number.

(a)

(b)

Figure 2.7: Decaying current (a) for the MLS in standard user operation with the corresponding lifetime (b). Data recorded on June 10th 2016.

Here, $\langle I \rangle$ is the average value of the stored current in the time interval Δt, while the beam current decays by ΔI. In Fig. 2.7, a decaying stored beam current for the MLS in the standard user operation mode is presented together with the lifetime determined by Eq. 2.71.

Different mechanisms are leading to particle losses. Each of these loss mechanisms contributes to the beam lifetime and has a lifetime contribution associated. In order to determine the beam lifetime from the individual lifetime contributions, the individual contributions have to be added inversely:

$$\tau^{-1} = \sum_i \frac{1}{\tau_i} = \frac{1}{\tau_t} + \frac{1}{\tau_g} + \ldots . \tag{2.72}$$

The different lifetime contributions are presented in the following sections 2.4.2, 2.4.3, and 2.4.4. The main contributions to particle losses are:

- **Gas scattering (Sec. 2.4.2)**

  Stored electrons perform Coulomb scattering at residual gas atoms. The scattering process can be elastic and inelastic, and can be performed with the nuclei or with the electrons of the gas atom or molecule. Stored particles may be deflected and lost to the limiting aperture. The gas lifetime is controlled by providing low vacuum pressure through continuous pumping.

- **Touschek scattering (Sec. 2.4.4)**

  Particles inside the bunch perform elastic Coulomb scattering. Thereby momenta may be exchanged between the particles. The changes in transverse momenta get Lorentz transformed, when deflected into the longitudinal plane.

The associated changes in longitudinal momenta lead to momentum deviations that may exceed the limiting momentum acceptance of the accelerator. The probability for such a scattering event depends on the electron density inside the bunch. By reducing the electron density, the Touschek lifetime can be improved.

Most lifetime contributions depend on the momentum acceptance of the accelerator. The momentum acceptance is the maximum deviation in momentum a particle can have from the reference momentum without being lost. If a particle exceeds this limit, it hits the limiting aperture. Therefore, in the following section, different types of acceptances are introduced. The smallest acceptance is the limiting acceptance.

2.4.1 Momentum Acceptance

The acceptance of an accelerator is a measure for the relative change in energy or momentum a particle can have without being lost. Three types of acceptance are important:

1. rf-acceptance,

2. dynamic acceptance,

3. geometrical / physical acceptance.

The smallest acceptance limits and defines the acceptance of the accelerator. In the following paragraphs, the different types are discussed.

RF-Acceptance: The rf-acceptance is given by the height of the *separatrix* in longitudinal phase space (comp. black curve in Fig. 2.8) (Wiedemann, 2007):

$$\delta^2_{\mathrm{acc,rf}} = \frac{U_0}{\pi h |\eta_c| E_0} \cdot F(q) \tag{2.73}$$

$$\text{with} \qquad F(q) = 2 \left[\sqrt{q^2 - 1} - \arccos \frac{1}{q} \right] \overset{q \to \infty}{\approx} 2q - \pi, \tag{2.74}$$

$$\text{and} \qquad q = \frac{eV_{\mathrm{rf}}}{U_0} = \frac{1}{\sin(\psi_s)},$$

where q is usually called the "overvoltage factor". Particles with momentum deviations larger than $\delta_{\mathrm{acc,rf}}$ travel on non closed lines in phase space. The momentum deviation increases until the particles eventually reach high horizontal amplitudes due to dispersion and are lost to the aperture. If the rf-acceptance is the limiting
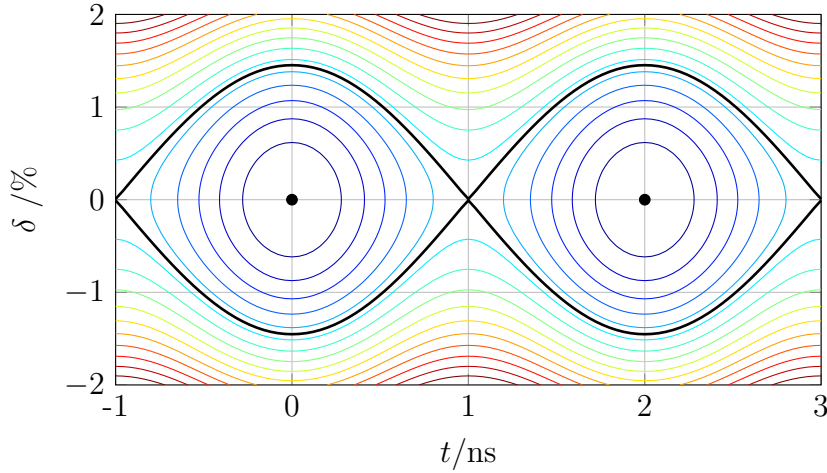
Figure 2.8: Longitudinal phase space for the MLS in standard user operation mode ($V_{\mathrm{rf}} = 500\,\mathrm{kV}$, $f_{\mathrm{rf}} \approx 500\,\mathrm{MHz}$) without energy loss. The black curve indicates the separatrix.

acceptance of an accelerator, the lifetime can be improved by upgrading the rf system so that higher voltages can be achieved. With an increased overvoltage factor, the rf-acceptance is increased likewise, resulting in an improved lifetime.

Dynamic Acceptance: The dynamic aperture limits the dynamic acceptance. The dynamic aperture is defined by the maximum transverse amplitude a particle can achieve without transcending into a divergent oscillation. Due to non-linear fields and potential at high amplitudes, the motion becomes anharmonic and resonances occur. The amplitude of a particle on resonance will divergently increase. The dynamic aperture can be determined by performing numerical particle tracking. Particles are tracked for a number of turns, in the order of a fraction or one damping time. If they exceed a certain amplitude they are declared as "lost". This amplitude is usually chosen to be much larger than the vacuum chamber. Particles are lost depending on their initial starting amplitudes. The border for which particles with higher initial amplitudes are lost is defined as the dynamic aperture. The dynamic aperture becomes smaller when strong non-linear fields are present, as the tuneshift with amplitude increases.

For the MLS in standard user operation mode, the dynamic aperture is larger than the geometric aperture (comp. Fig. 2.9). However, for the installation of the RW it has to be considered.

Geometrical Acceptance: If a particle spontaneously changes its energy by emitting a photon or by performing Coulomb scattering, it will perform betatron
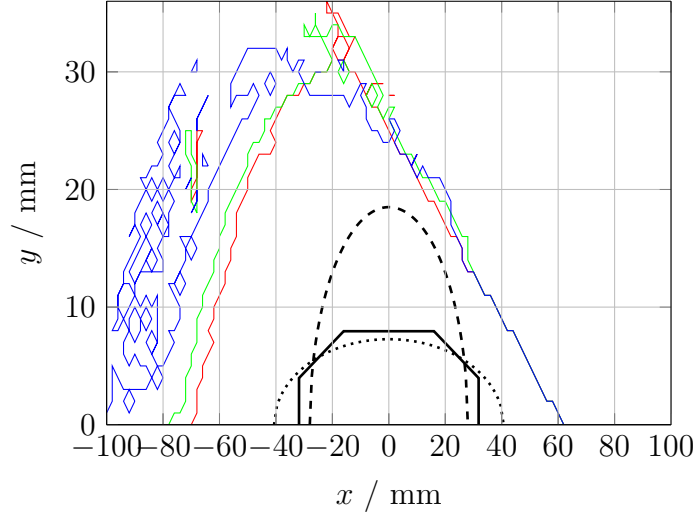
Figure 2.9: Dynamic aperture for the MLS in standard user operation mode without cavity and radiation, determined with `FTRACK` (Sec. 3.4.1). Particle energies: (green) on-energy, (red) -1%, (blue) 1%. The geometrical apertures (black) were scaled according to the square root of the ratio of the β-functions at the septum to the β-functions at the longitudinal position s_a of the aperture: $a_{x/y,\mathrm{plot}} = a_{x/y}(s_a) \cdot \sqrt{\frac{\beta_{x/y,\mathrm{septum}}}{\beta_{x/y}(s_a)}}$. The geometrical apertures are the septum magnet (dashed), the undulator chamber (dotted), and the remaining vacuum chamber (solid).

oscillations around a new dispersive closed orbit according to its new energy. If the amplitude of the particle is too high, the particle hits the limiting physical aperture. The minimum transverse displacement for which a particle is lost is $x_\eta = a(s)/2$, with $a(s)$ being the limiting aperture at azimuthal position s. With assuming that the beam is well centred, the geometrical acceptance can be described as:

$$\delta_{\mathrm{acc,g}} = \left(\frac{\Delta p}{p}\right)_{\mathrm{max}} = \min\left[\frac{a(s)}{2\eta_x(s)}\right] \ . \tag{2.75}$$

In Fig. 2.10, the geometrical acceptance is presented as function of the longitudinal position in the MLS. The minimum values for the geometric acceptance are found in the centre of the DBA structures, where the dispersion function has its maximum value of $\eta_x = 1.48\,\mathrm{m}$ (comp. also Fig. 1.3a). The minimum value of the geometric acceptance is found to be $\delta_{\mathrm{acc,g,MLS}} = 1.15\,\%$. It is not possible to decrease the peak dispersion below $1.43\,\mathrm{m}$ without changing the optics significantly. This implies that the geometric acceptance is limited to $\sim 1.22\,\%$. It is therefore of limited use to increase the cavity voltage significantly in order to improve the rf-acceptance at the MLS.
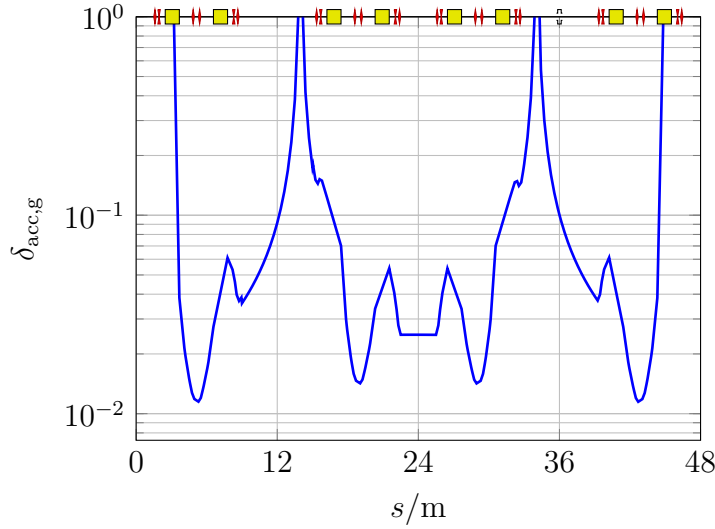
Figure 2.10: Geometrical acceptance for the MLS. The acceptance is calculated as in Eq. 2.75.

2.4.2 Gas Lifetime

Stored particles in the accelerator may scatter with the residual gas molecules inside the vacuum chamber and are lost due to their changed angle or momentum after the scattering event. Such arises the gas lifetime contribution, which is mainly controlled by pumping in order to maintain a sufficiently low pressure of the residual gas. There are two major effects (Bocchetta, 1996):

- **Elastic collision:**
  Elastic scattering leads to a deflection of the trajectory which increases the betatron oscillations. The particles are lost if they hit the geometrical or dynamic aperture.

- **Inelastic collision:**
  The stored particles lose momentum to their scattering partner during an inelastic collision. The particles are lost if their momentum deviation exceeds the momentum acceptance.

The cross sections for elastic and inelastic scattering are derived in detail in (Bocchetta, 1996). The cross section for elastic scattering including particle loss is given as:

$$\sigma_e = 2\pi r_e^2 \cdot \frac{1}{\gamma^2} \cdot Z^2 \cdot \frac{\langle \beta_y \rangle \beta_{y,a}}{a_y^2}, \tag{2.76}$$

where $a_y^2/\beta_{y,a}$ is the minimum ratio between the square of the vertical aperture a_y and vertical β-function $\beta_{y,a}$ at aperture a_y and azimuthal position s. Z is the atomic number of the residual gas and $\langle \beta_y \rangle$ is the average vertical β-function around the ring.

The cross section for the inelastic scattering process including particle loss is found to be:

$$\sigma_i = \frac{4r_e^2}{137} \cdot \left\{ F(Z) \cdot \frac{4}{3} \left[\ln\left(\frac{1}{\delta_{\mathrm{acc}}}\right) - \frac{5}{8} \right] + \frac{Z(Z+1)}{9} \left[\ln\left(\frac{1}{\delta_{\mathrm{acc}}}\right) - 1 \right] \right\},$$
$$(2.77)$$

with

$$F(Z) = Z^2 \ln\left(\frac{183}{Z^{1/3}}\right) + Z \ln\left(\frac{1194}{Z^{2/3}}\right).$$

The total cross section is the sum of the cross sections for the individual events (Bocchetta, 1996):

$$\sigma_{\mathrm{loss}} = \sigma_e + \sigma_i. \tag{2.78}$$

The gas lifetime can then be calculated as

$$\tau_g^{-1} = \sigma_{\mathrm{loss}} \beta c \rho, \qquad \tau_g \stackrel{\mathrm{MLS}}{\approx} 43.5\,\mathrm{h}, \tag{2.79}$$

where ρ is the gas density depending on the composition of the molecules present (Bocchetta, 1996). For the MLS, the theoretical value was calculated from the results of a gas composition measurement for the MLS and assuming a constant pressure of $\rho = 1 \times 10^{-9}\,\mathrm{mbar}$ (Dürr and Borninkhof, 2013; Goetsch, 2013). Due to the emitted synchrotron radiation, desorption of gas molecules from the vacuum chamber walls is a contributor to the residual gas pressure in light sources. Hence, the pressure and the gas lifetime depend on the stored beam current.

Equations 2.76 and 2.77 are independent of the damping partition D. Hence, changing the damping partition D does not affect the gas lifetime. It is therefore assumed that the gas lifetime is constant for the remainder of this thesis.

The gas lifetime can be estimated by measuring the lifetime for different bunch current settings: the same amount of current is distributed over a varying number of buckets. Thereby, the total ring current (and with that the gas lifetime) stays constant, whereas the bunch current varies (and with that the Touschek lifetime contribution (see Sec. 2.4.4)). When plotting the inverse of the measured lifetime as
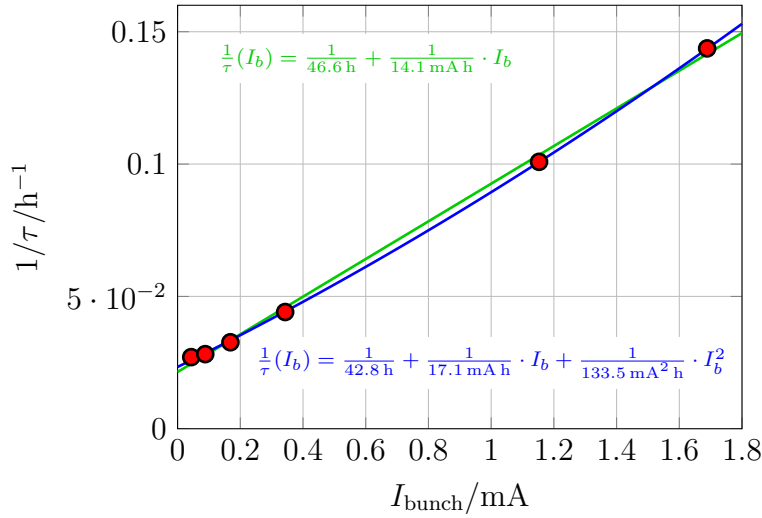
Figure 2.11: Inverse lifetime as a function of the bunch current in the standard user operation mode at the MLS. The ring current was kept constant, resulting in a constant gas lifetime contribution $\tau_g = \text{const.}$. The ring current was distributed over a varying number of bunches to alter the bunch current.

a function of the bunch current, the gas lifetime can be estimated by the y-intercept of the applied linear regression (comp. Fig. 2.11). A second order polynomial fit showed to agree better with the experimental data than a first order polynomial fit which theory would suggest. The first order polynomial fit results in a y-intercept corresponding to a gas lifetime of $46.6(67)\,\text{h}$. For the second order polynomial fit, the gas lifetime would be estimated to be $42.8(21)\,\text{h}$, which is close to the theoretical predictions ($\tau_{g,\text{theo}} = 43.5\,\text{h}$).

The same kind of measurement was already performed in (Goetsch, 2013): the gas lifetime contribution was estimated to be $\tau_g = 24.5\,\text{h}$ for the MLS. The differences may be due to improved vacuum conditions in the meantime. For all following calculations, the gas lifetime is assumed to have a value of $24.5\,\text{h}$. This is a worst case scenario. Any higher value for the gas lifetime contribution would only further increase the predicted lifetimes.

2.4.3 Quantum Lifetime

As discussed in Sec. 2.3, emission of synchrotron radiation leads to both radiation damping and quantum excitation. Excitation and damping lead to a "random" walk of the particles in phase space. Additionally, the particles perform multiple small angle Coulomb scattering events with other particles inside the same bunch. This effect is called intra-beam scattering and it leads to a continuous exchange of en-
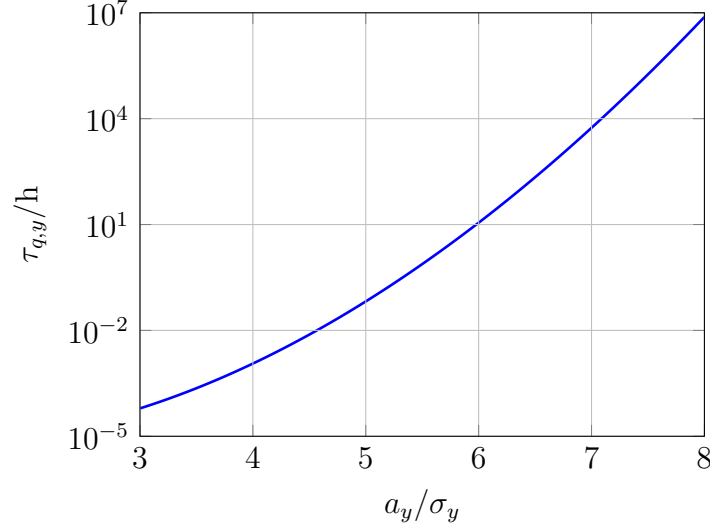
Figure 2.12: Vertical quantum lifetime as a function of the ratio between free vertical aperture a_y and vertical beam size σ_y.

ergy and momenta in all planes. Both effects lead to small random variations of the particles coordinates. After several damping times, the distribution of the coordinates a particle obtained approaches that of a Gaussian distribution, independent of the particles initial conditions. The standard deviation of the Gaussian distribution in the individual plane is a function of the lattice (Bocchetta, 1996). Particles with very high amplitudes are lost at the limiting aperture in the respective plane. Due to constant diffusion, caused by the effects mentioned above, a continuous loss of these high amplitude ("halo"-) particles is given. The different quantum lifetimes depend on the damping time τ_i in the respective plane i, the aperture a_i, as well as the standard deviation of the Gaussian distribution σ_i (Bocchetta, 1996):

$$\tau_{q,i} = \frac{\tau_i}{2} \frac{\exp\left(\zeta^2\right)}{\zeta^2}, \tag{2.80}$$

with

$$\zeta^2 = \frac{a_i^2}{2\sigma_i^2}.$$

However, for the horizontal plane effects of the dispersion have to be taken into account.

Vertical Quantum Lifetime: As derived in Eq. 2.80, the vertical quantum lifetime is

$$\tau_{q,y} = \tau_y \frac{\sigma_y^2}{a_y^2} \cdot \exp\left(\frac{a_y^2}{2\sigma_y^2}\right). \tag{2.81}$$

The vertical quantum lifetime depends on the ratio between the free vertical aperture a_y and the bunch height σ_y. In Fig. 2.12, the vertical quantum lifetime for different values of the ratio between a_y and σ_y is depicted. For the MLS in standard conditions (e.g. no scrapers near the beam), the ratio between vertical aperture $a_y = 12\,\text{mm}$ and vertical beam size $\sigma_y \sim 250\,\mu\text{m}$ is in the order of 48. Therefore, the vertical quantum lifetime is negligible. In fact, for ratios above 6.5, the vertical quantum lifetime is longer than 100 h. In the remainder of this work, the vertical quantum lifetime will not be considered because it is independent of the damping partition at the MLS (no vertical bends are present).

Horizontal Quantum Lifetime: For the horizontal quantum lifetime, effects of the dispersion as well as coupling between the longitudinal and the horizontal plane have to be considered. In (Bocchetta, 1996), the horizontal quantum lifetime is derived to be:

$$\tau_{q,x} = \frac{\tau_x}{\sqrt{2\pi}} \frac{\sigma_x^3}{a_x^3} \exp\left(\frac{a_x^2}{2\sigma_x^2}\right) \frac{\tau_s}{[\tau_x r + \tau_s(1-r)]\sqrt{r(1-r)}}, \tag{2.82}$$

with

$$\sigma_x^2 = \varepsilon_x \beta_x + \eta_x^2 \sigma_\delta^2,$$
$$r = \frac{\eta_x^2 \sigma_\delta^2}{\sigma_x^2}.$$

Like the vertical quantum lifetime, the horizontal quantum lifetime is high enough to be neglected for the standard operation at the MLS. For the standard operation it shows the same behaviour towards the ratio between free aperture and beam size as the vertical quantum lifetime. However, with the installation of the RW, the horizontal as well as the longitudinal quantum lifetime become important, as they limit the maximum possible lifetime increasing effect of the RW. This dependency will be explained after the longitudinal quantum lifetime is introduced.

Longitudinal Quantum Lifetime: The longitudinal quantum lifetime depends on the energy spread σ_δ and the limiting momentum acceptance δ_{acc} of the acceler-

ator. The longitudinal quantum lifetime is found to be (Bocchetta, 1996):

$$\tau_{q,s} = \tau_s \frac{\sigma_\delta^2}{\delta_{\text{acc}}^2} \exp\left(\frac{\delta_{\text{acc}}^2}{2\sigma_\delta^2}\right). \tag{2.83}$$

The longitudinal quantum lifetime takes the same form as the vertical quantum lifetime (Eq. 2.81). Therefore, a ratio between acceptance δ_{acc} and energy spread σ_δ in the order of 6.5 would lead to a longitudinal quantum lifetime above $100\,\text{h}$. For an energy spread of 4.4×10^{-4}, the acceptance would need to be as low as $2.86\,‰$. At the MLS, the acceptance is as high as $1.15\,\%$. Therefore, the longitudinal quantum lifetime is not important for the standard operation at the MLS.

However, as well as the horizontal quantum lifetime, the longitudinal quantum lifetime depends implicitly on the damping partition through the energy spread. Like the horizontal quantum lifetime, the longitudinal quantum lifetime becomes important with the installation of the RW. In the following section, these dependencies are discussed.

Quantum Lifetime as a Function of the Damping Partition

Rewriting Eq. 2.82 and 2.83 in terms of the damping partition D and the initial values for energy spread $\sigma_{\delta,0}$ and damping time $\tau_{i,0}$ for $D = 0$ results in

$$\tau_{q,x}(D) = \frac{1}{\sqrt{2\pi}}\tau_{x,0}\frac{1}{1-D} \cdot \frac{\sigma_x(D)^3}{a_x^3} \cdot \exp\left(\frac{a_x^2}{2\sigma_x(D)^2}\right)$$
$$\cdot \frac{\tau_{s,0}\frac{2}{2+D}}{[\tau_{x,0}\frac{1}{1-D}r(D) + \tau_{s,0}\frac{2}{2+D}(1-r(D))]\sqrt{r(D)(1-r(D))}}, \tag{2.84}$$

with

$$\sigma_x(D)^2 = \varepsilon_{x,0}\frac{1}{1-D}\beta_x + \eta_x^2\sigma_{\delta,0}^2\frac{2}{2+D},$$
$$r(D) = \frac{\eta_x^2\sigma_{\delta,0}^2}{\sigma_x(D)^2} \cdot \frac{2}{2+D}.$$

for the horizontal quantum lifetime and

$$\tau_{q,s}(D) = \tau_{s,0} \cdot \frac{2}{2+D} \cdot \frac{\sigma_{\delta,0}^2}{\delta_{\text{acc}}^2} \cdot \frac{2}{2+D} \cdot \exp\left(\frac{\delta_{\text{acc}}^2}{4\sigma_{\delta,0}^2} \cdot (2+D)\right)$$
$$= \tau_{s,0}\frac{\sigma_{\delta,0}^2}{\delta_{\text{acc}}^2} \cdot \frac{4}{(2+D)^2} \cdot \exp\left(\frac{\delta_{\text{acc}}^2}{4\sigma_{\delta,0}^2} \cdot (2+D)\right), \tag{2.85}$$
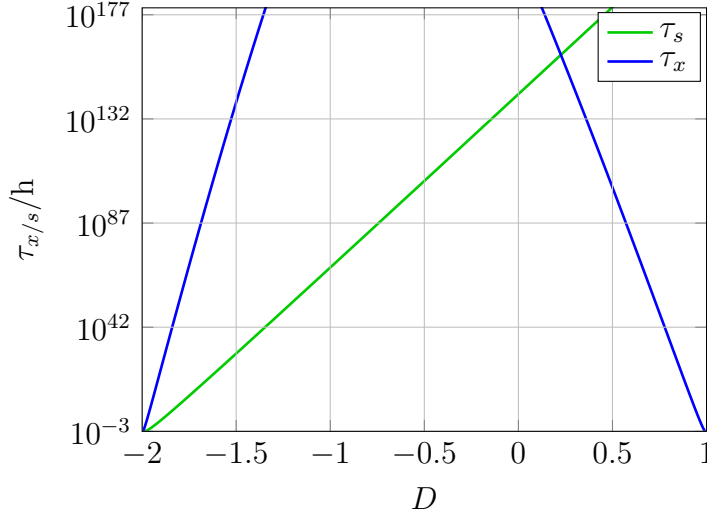
Figure 2.13: Horizontal and longitudinal quantum lifetime as a function of the damping partition D according to Eq. 2.84 and 2.85.

for the longitudinal quantum lifetime.

In Fig. 2.13, the horizontal and longitudinal quantum lifetime as a function of the damping partition D are presented. The MLS lattice in standard user conditions has a damping partition of $D = -0.055$, corresponding to values for the emittance and the energy spread of $117.67\,\mathrm{nm\,rad}$ and 4.42×10^{-4} respectively. From that, the values for emittance and energy spread for $D = 0$ can be calculated to be $\varepsilon_{x,0} = 123.79\,\mathrm{nm\,rad}$ and $\sigma_{\delta,0} = 4.36 \times 10^{-4}$. It was assumed that the dispersion as well as the β-functions do not change with changing the damping partition and are equal to the ones of the standard user operation mode (comp. Fig. 1.3). The momentum acceptance was also assumed to be constant at $\delta_{acc} = 1.15\,\%$ (comp. Sec. 2.4.1), whereas the limiting horizontal aperture was assumed to be the one of the standard vacuum chamber with $a_x = 35\,\mathrm{mm}$. The horizontal quantum lifetime drops below $1000\,\mathrm{h}$ for $D \leq -1.9714$ and $D \geq 0.9577$, whereas it drops below $1\,\mathrm{h}$ for $D \leq -1.9824$ and $D \geq 0.9733$. The longitudinal quantum lifetime drops below $1000\,\mathrm{h}$ for $D \leq -1.8823$, and it drops below $1\,\mathrm{h}$ for $D \leq -1.9277$.

Therefore, two lower and upper limits for a useful damping partition can be defined. The first one is for the case that the horizontal and longitudinal quantum lifetime yield negligible contributions to the total lifetime. For this case the damping partition has to be part of the interval

$$i_{D,1} = \left[-1.8823, 0.9577\right]. \tag{2.86}$$

The second interval is the limit for operation with a desired lifetime above $1\,\mathrm{h}$. For

this case the damping partition has to be part of the interval

$$i_{D,2} = \left]-1.9277, 0.9733\right[. \tag{2.87}$$

Hence, horizontal and longitudinal quantum lifetime set a limit to the achievable lifetime improvement by damping redistribution. This effect will also be of interest in Sec. 2.5, where the total lifetime as a function of the damping partition is discussed.

2.4.4 Touschek Lifetime

The Touschek effect is one of the major loss rate contributors in storage rings. It is the result of particles scattering within the same bunch. During the scattering process, comparably small momenta in the transverse plane may get transferred to the longitudinal plane. Due to the Lorentz shift, formerly small transverse momenta lead to momentum deviations in the order of several percent, which is comparable to the momentum acceptance of the accelerator. Particles which surpass the momentum acceptance of the accelerator are lost, giving rise to the Touschek lifetime.

An order of magnitude calculation for the MLS can be conducted as follows (comp. (le Duff, 1989)): assuming a particle at betatron amplitude $x_\beta = 1000\,\mu\text{m}$ at a place where the horizontal β-function has a value of $\beta_x = 10\,\text{m}$. The maximum horizontal angle is then given as $x' = x_\beta/\beta_x = p_x/p_0$. Assuming the operation energy of the MLS with $629\,\text{MeV}$, the transverse momentum can be as high as $p_x = 62.9\,\text{keV}\,c^{-1}$. When completely transferred into the longitudinal direction, it becomes $\Delta p = \gamma p_x = 77.43\,\text{MeV}\,c^{-1}$. This corresponds to a momentum deviation of $\delta = 12.3\,\%$, which is clearly larger than the limiting momentum acceptance of an accelerator ($\delta_{\text{acc,MLS}} \sim 1.15\,\%$).

The Touschek lifetime is derived by integrating over all scattering angles leading to particle losses. Here, the flat beam approximation presented by (le Duff, 1989) is given and for further information the reader is directed to (Piwinski, 1998) and (le Duff, 1989). According to (le Duff, 1989) the Touschek lifetime can be calculated as:

$$\frac{1}{\tau_t} = \frac{N r_e^2 c}{8\pi \sigma_x \sigma_y \sigma_s} \frac{1}{\delta_{\text{acc}}^3 \gamma^2} \mathscr{D}(\xi), \tag{2.88}$$

with a function $\mathscr{D}(\xi)$ as

$$\mathscr{D}(\xi) = \sqrt{\xi} \left\{ -\frac{3}{2} e^{-\xi} + \frac{\xi}{2} \int_{\xi}^{\infty} \frac{\ln u e^{-u}}{u} \, \mathrm{d}u + \frac{1}{2}(3\xi - \xi \ln \xi + 2) \int_{\xi}^{\infty} \frac{e^{-u}}{u} \, \mathrm{d}u \right\},$$

$$\xi = \left(\frac{\delta_{\mathrm{acc}} \beta_x}{\gamma \sigma_x} \right)^2. \tag{2.89}$$

The Touschek lifetime mainly depends on the limiting momentum acceptance ($\tau_t \propto \delta_{\mathrm{acc}}^3$), the beam energy ($\tau_t \propto \gamma^2$), and the electron density ($\tau_t \propto \frac{\sigma_x \sigma_y \sigma_s}{N}$). N is the number of particles inside the bunch. For a long Touschek lifetime component, the momentum acceptance of the accelerator should be as high as possible as it has the strongest impact on the Touschek lifetime. If the momentum acceptance is already optimized, the Touschek lifetime can be improved by reducing the scattering rate. The scattering rate can be reduced by lowering the electron density inside the bunch. This can be done in two ways: reducing the number of electrons or increasing the bunch volume. With decreasing the number of electrons inside the bunch, the intensity of the emitted radiation is reduced. As it is aimed to maintain the intensity, reducing the number of particles is not a rewarding approach. Increasing the transverse bunch sizes is also not useful as an increased transverse bunch size results in a reduced brilliance at the beamlines. What can be adjusted is the bunch length. With adjusting the damping partition, it is possible to increase the bunch length while keeping the average bunch width constant. Thereby, the bunch volume is increased, resulting in a reduced scattering rate and improved Touschek lifetime. In Sec. 2.4.4, the dependencies of the Touschek lifetime contribution on the damping partition D are discussed.

Measurement of the Touschek Lifetime Component

For the measurement presented in Fig. 2.11, the gas lifetime was kept constant by keeping the ring current constant. The Touschek lifetime, depending on the bunch current, was varied by distributing the total ring current over a varying number of buckets. Assuming all other lifetime contributions negligible, the inverse of the total beam lifetime as a function of the bunch current I_b is constituted as

$$\frac{1}{\tau}(I_b) = \frac{1}{\tau_g} + \frac{1}{\tau_t(I_b)} = \frac{1}{\tau_g} + \tilde{c} \cdot I_b, \tag{2.90}$$

with

$$\tilde{c} = \frac{1}{e f_{\mathrm{rev}}} \cdot \left\langle \frac{r_e^2 c}{8\pi \sigma_x \sigma_y \sigma_s} \frac{1}{\delta_{\mathrm{acc}}^3 \gamma^2} \mathscr{D}(\xi) \right\rangle. \tag{2.91}$$

Therefore, it is possible to derive a value for the proportionality constant $\tilde{c}$ by means of linear regression in Fig. 2.11. For the standard user operation mode at the MLS, $\tilde{c}$ has a value of $\tilde{c} = 0.071(4)\,\mathrm{mA}^{-1}\,\mathrm{h}^{-1}$. The proportionality constant can be made small by increasing the bunch volume, which is aimed for by operating a RW at the MLS.

Touschek Lifetime as a Function of the Damping Partition

Rewriting Eq. 2.88 in terms of the damping partition D and the initial values for energy spread $\sigma_{\delta,0}$ and emittance ε_0 results in

$$\tau_t^{-1}(D) = \frac{N r_e^2 c}{8\pi \delta_{\mathrm{acc}}^3 \gamma^2} \cdot \frac{\mathscr{D}(\xi(D))}{\sigma_x(D)\sigma_y(D)\sigma_s(D)}, \tag{2.92}$$

with

$$\xi(D) = \left(\frac{\delta_{\mathrm{acc}} \beta_x}{\gamma \sigma_x(D)} \right)^2,$$

$$\sigma_x(D) = \sqrt{\varepsilon_{x,0} \frac{1}{1-D} \beta_x + \eta_x^2 \sigma_{\delta,0}^2 \frac{2}{2+D}},$$

$$\sigma_y(D) = \sqrt{\varepsilon_{x,0} \frac{1}{1-D} \kappa \beta_y},$$

$$\sigma_s(D) = \sigma_{s,0} \cdot \sqrt{\frac{2}{2+D}}.$$

The vertical beam size depends on the damping partition via the emittance coupling parameter $\kappa = \varepsilon_y / \varepsilon_x$. At the MLS in standard user operation, the vertical beam size is controlled and kept constant with varying beam current using white noise excitation. This reduces ion effects on the beam. Therefore, the vertical beam size can be considered as independent of D while applying white noise excitation.

In Fig. 2.14, the Touschek lifetime normalized to the Touschek lifetime for $D = 0$ ($\tau_{t,0} = 8.36\,\mathrm{h}$ at $I = 150\,\mathrm{mA}$) as a function of the damping partition is shown for both varying σ_y with D and σ_y independent of D. As said, for the MLS the curve for an independent σ_y of D is applicable. Therefore, the Touschek lifetime at the MLS can be improved by decreasing the damping partition to negative values below -1 instead of values below -1.5 for varying σ_y with D.
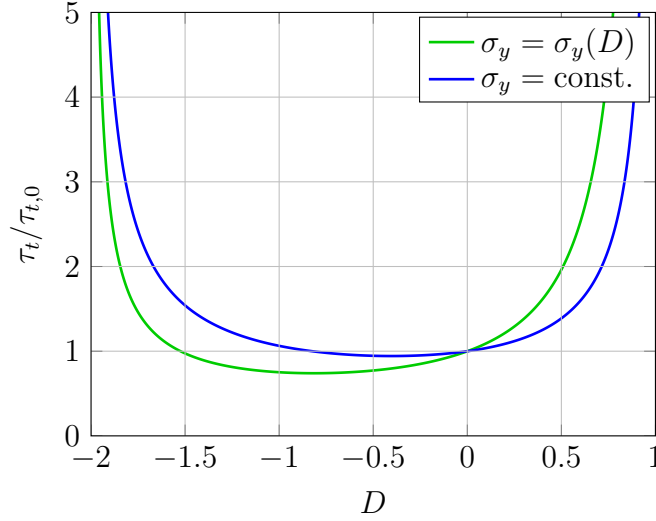
Figure 2.14: Touschek lifetime normalized to the Touschek lifetime for $D = 0$ as a function of the damping partition D.

2.5 Lifetime as a Function of the Damping Partition

In the previous section, the different lifetime contributions were derived. The Touschek lifetime and the horizontal and longitudinal quantum lifetime show a dependency on the damping partition D, whereas the gas lifetime and the vertical quantum lifetime are independent of it. The gas lifetime is treated as a constant throughout this work. Although the gas lifetime, varies with the stored beam current it is constant for a fixed current. The quantum lifetimes, usually high enough to be neglected, do have an impact on the lifetime for the damping partition D close to -2 and 1 (comp. Fig. 2.13). The Touschek lifetime increases for D approaching -2 and 1. When approaching $D = -2$, the Touschek lifetime increases because of the increase in bunch length through the energy spread. When approaching $D = 1$, the Touschek lifetime increases because of the increasing horizontal beam size through the horizontal emittance.

In Fig. 2.15, the resulting lifetime as a function of the damping partition D is presented, together with the variables emittance ε_x, energy spread σ_δ, and average horizontal beam size $\bar{\sigma}_x$. The gas lifetime as well as the vertical beam size were assumed to be constant. For approaching $D = 1$, the lifetime increases because of the increasing Touschek lifetime until it drops sharply because of the horizontal quantum lifetime at $D = 0.9733$. For approaching $D = -2$, the lifetime again increases because of the increasing Touschek lifetime until it drops sharply because
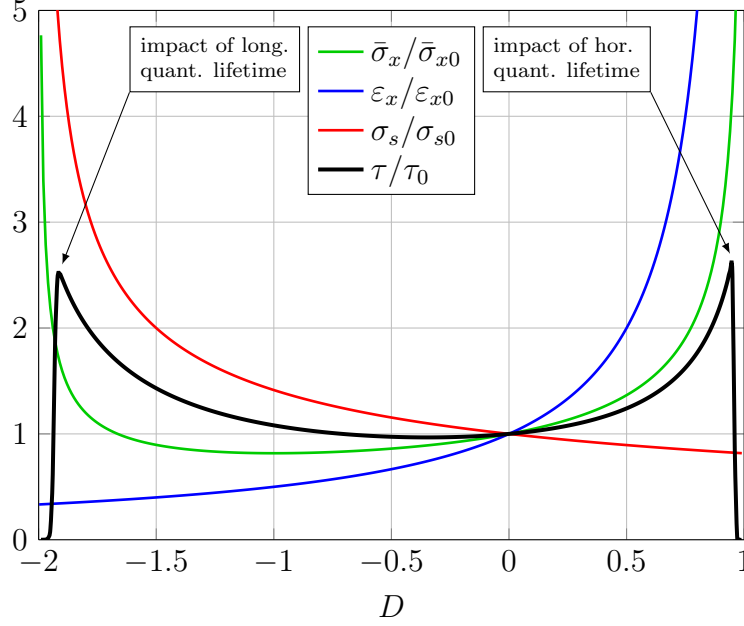
Figure 2.15: Effect of changing the damping partition D on the lifetime τ (for constant vertical beam size), the horizontal emittance ε_x, the energy spread σ_δ, and the average horizontal beam size $\bar{\sigma}_x$, all normalized to their initial values at $D = 0$.

of the longitudinal quantum lifetime at $D = -1.9277$.

For both positive and negative values of D an increase in lifetime of a factor of 2 or more can be achieved. However, negative values of D are preferable. For positive values, the lifetime increasing effect is caused by an increase in emittance. This effect reduces the brilliance at the experimental observation point and hence, should be avoided. For negative values of D, the lifetime increasing effect is caused by an increased bunch length, while simultaneously the horizontal emittance is reduced. In order to increase the lifetime by a factor of 2 a damping partition below ~ -1.75 is appropriate.

The horizontal beam size $\bar{\sigma}_x$, averaged along the azimuth s, has a minimum at $D = -1$. This is the reason why the lattices for most storage ring based synchrotron light sources today are designed for an initial damping partition around $D = -1$, e.g. MAX IV with a design damping partition of $D_{\text{MAX IV}} = -0.847$ (Tavares et al., 2014). The emittance for $D = -1$ is reduced by a factor of 2 compared to $D = 0$, while the energy spread is increased by a factor of $\sqrt{2}$. Thus, the minimum impact of the energy spread and the maximum impact of the reduced emittance on the source size is achieved.

2.6 Further Techniques to Improve the Lifetime through Bunch Lengthening

There are other techniques to increase the bunch length in a storage ring. Two rather popular solutions that are commonly applied are presented in this section. Namely, these are phase modulation of the rf-signal and the installation of a 3rd harmonic cavity.

2.6.1 Phase Modulation of the RF

Phase modulation of the rf-signal is an easy and quick method to lengthen the bunches and increase the lifetime. The rf-signal is modulated at a frequency two times the synchrotron frequency. At the KEK photon factory, the beam lifetime could thus be improved from 22 h to 36 h (Sakanaka et al., 2000). Another example is the DELTA storage ring: here a lifetime increasing effect in the order of 20 % is achieved while simultaneously reducing coupled-bunch instabilities (Sommer et al., 2016).

At the MLS, this method was also applied. But, it turned out that the most demanding user at the MLS, in terms of beam stability, measured a signal to noise ratio an order of magnitude worse than without the modulation. The modulation of the rf-signal was noticeable in the radiation signal at the beamline and measurements could not be conducted. However, the underlying mechanism for this is still unclear. This method may be applied at the MLS if the stability requirements of the users are not too stringent.

2.6.2 Higher Harmonic Cavity

Operating higher harmonic (Landau) cavities are a common method to reduce the electron density through bunch lengthening in storage ring based light sources. These are passive cavities, usually operating at the 3rd harmonic of the base rf-frequency. With the superposition of the base rf-voltage and the induced voltage in the Landau cavities, the potential takes a form as depicted in Fig. 2.16. The phase of the 3rd harmonic cavity is adjusted such, that the sum voltage has a flat point corresponding to the energy loss per turn of the stored electrons. Thus, the potential for stable storage of the particles is lengthened in time, which leads to bunch lengthening. However, there are some reasons why a Landau cavity may not
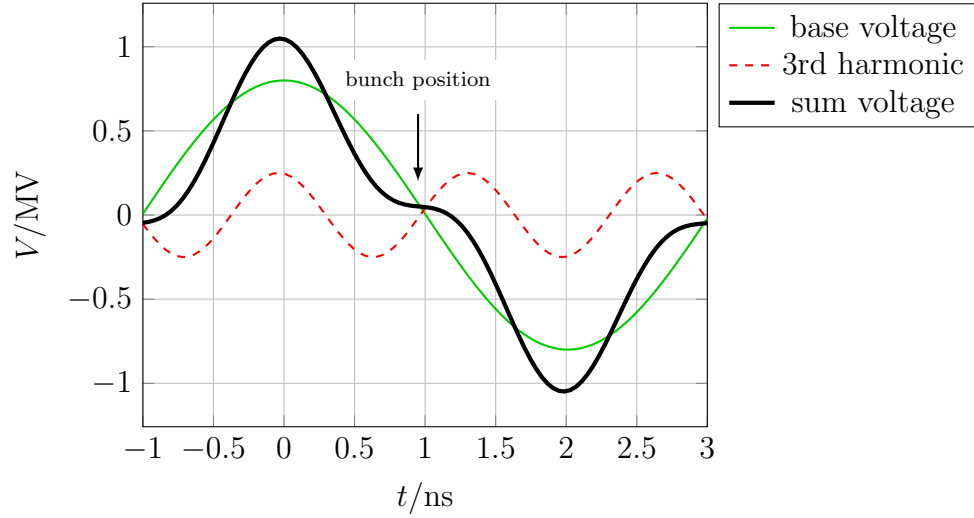
Figure 2.16: Superposition of base rf-voltage and induced voltage by a 3rd harmonic cavity.

be the optimum choice for increasing the lifetime at the MLS, and why the RW does have advantages compared to a Landau cavity in the case of the MLS:

- **Tuneability**
  Other than the RW, a Landau cavity has only a limited tuning range, and is therefore usually specified for a limited stored beam current interval (e.g. $100\,\mathrm{mA}$ to $200\,\mathrm{mA}$ in the case of the MAX II storage ring (Å. Anderson, 1998)). This is not applicable for the MLS, as the beam current may vary rapidly by two orders of magnitude during operation, depending on the user demands. Concerning the lifetime this would not be problematic, as the lifetime is long for small currents. However, the reliability and reproducibility of an accelerator, dedicated to metrology applications, includes the bunch length. If the Landau cavities do not work for small currents, the bunch length varies with varying beam current.

- **Beam interaction in parking position**
  When the Landau cavities are switched off, they may still interact with the stored beam, as they add to the impedance budget of the machine. The RW does not add to the impedance budget, as it is an out of vacuum device with no interaction with the beam when switched off, apart from hysteresis effects.

- **Beam loading**
  A Landau cavity would be sensitive to the fill pattern of the machine. The demand for high flexibility of the MLS also includes the flexibility of the fill

pattern varying from filling every bucket down to a single bunch, which is troublesome for a passive Landau cavity.

- **Brilliance**

  One major advantage of the RW over a 3$^{\text{rd}}$ harmonic cavity is the option to change the emittance. With carefully choosing the beam optics, the users of the synchrotron radiation may gain in brilliance, while simultaneously the lifetime is increased.

Some of the above mentioned advantages of the RW over a 3$^{\text{rd}}$ harmonic cavity can also be achieved by an actively powered 3$^{\text{rd}}$ harmonic cavity. The induced voltage is then independent of the stored beam current and fill pattern. Up to now, no such cavity is in operation. In future, such a cavity could further enhance the performance of the MLS. For now, the RW is the first item to upgrade the MLS, mainly because of the positive impact on the emittance and because there is no need to install cryogenic systems.

A Robinson Wiggler for the MLS

Several constraints have to be considered when designing an additional magnetic insertion device for an existing accelerator. The available free installation length in the straight section is arguably one of the strongest limitations for the new magnet structure. It is possible to move the remaining parts of the existing accelerator in order to create additional space, but it should be avoided if possible. Reasons for not breaking the existing lattice are:

- the downtime of the user operation can be minimized,

- no realignment of accelerator components is necessary,

- the position of the source points at the beamlines can be maintained,

- it is not necessary to develop new optics and settings for the operation modes when the new magnet is switched off.

The limitation in available length, influences the design parameters of the ID, such as the number of poles or the current density in the coils. Furthermore, the desired field parameters such as field strength and gradient should be met within specified boundaries to guarantee operation at long lifetimes while achieving the desired effect on the beam. A minor field quality affects the dynamic aperture and hence, jeopardizes the lifetime of the beam and the operation of the accelerator.

In the following, the requirements for the RW in order to improve the lifetime together with the limiting constraints will be introduced. According to these, a normal conducting design is derived in Sec. 3.2, which is then further investigated regarding its effects on the beam dynamics and its radiation characteristics in the following sections. At the end of the chapter, an alternative superconducting design is presented.
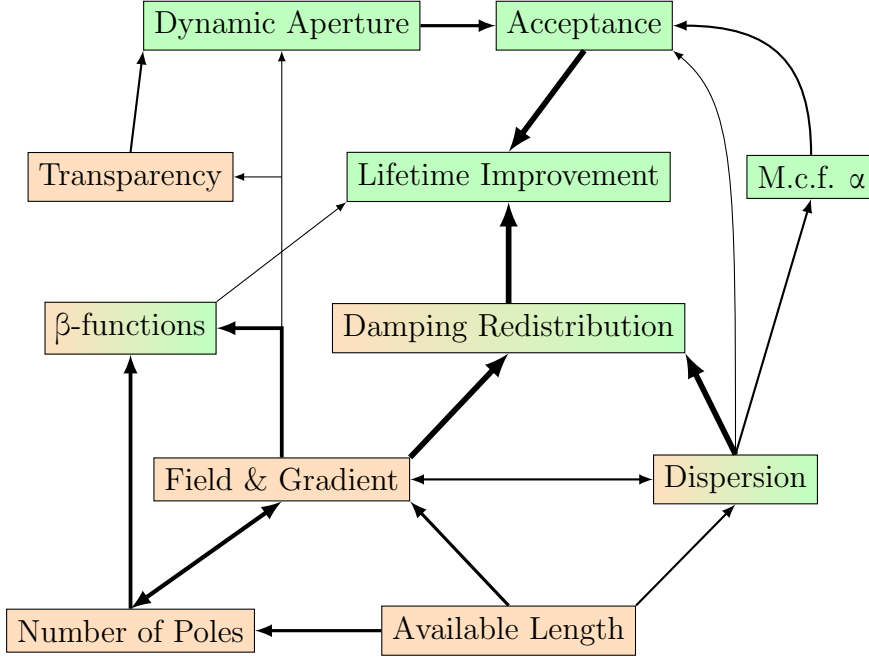
Figure 3.1: Sketch of different requirements and quantities that are affected by the operation of the RW and in turn set conditions for the design of the RW. The thickness of the connecting arrows corresponds to the significance of the effect. Green: accelerator related; orange: design related.

3.1 Requirements and Limitations

As described in Sec. 1.3 and 2.3.4, the RW consists of a set of alternating poles superimposing both dipole and quadrupole field components. The RW is then placed at a location in the accelerator where the dispersion function is non-zero. All three quantities, i.e. dipole field B_y, gradient $\partial B_y/\partial x$, and dispersion η_x need to have certain non vanishing values. Finding the optimum settings for each of these, depends on constraints and requirements that are themselves interdependent. A sketch of the different effects is presented in Fig. 3.1.

(A) Space Limitations: The RW is being designed for an accelerator that has been successfully in user operation since 2008. It is desirable not to break the existing magnet lattice in order to install the RW. Therefore, if possible, the RW has to fit in the available space in the short straight section opposite the septum magnet. If the maximum length of the device is limited, the minimally required on-axis field in the poles, the maximum number of poles that can be installed, and consequently the effects on the accelerator optics are affected. After optimization of the usage of the free space in the remaining straight sections, the available longitudinal length in the K3 straight is 1.9 m.
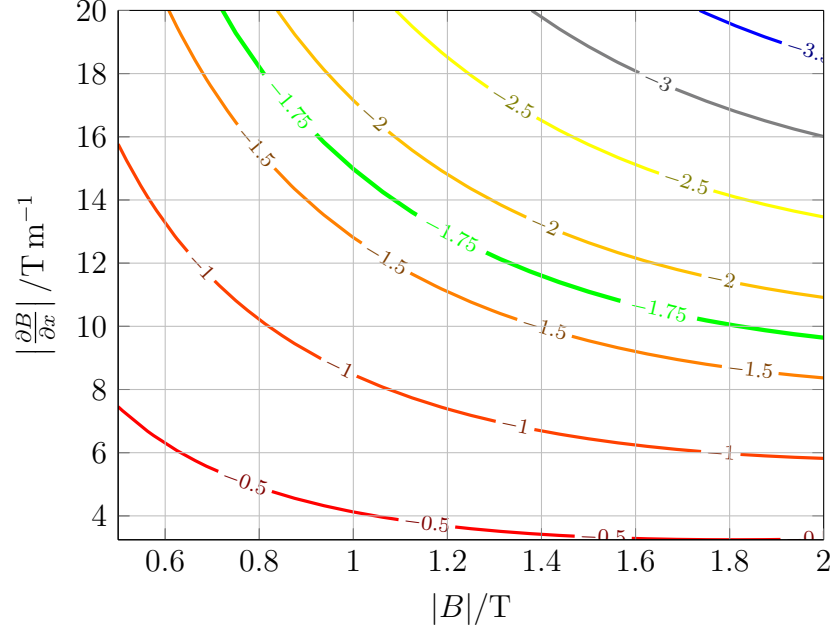
Figure 3.2: Damping partition D in contour lines as a function of field and gradient in the wiggler for a total length of $1.1\,\mathrm{m}$ and dispersion $\eta_x = 1.0\,\mathrm{m}$ at the wiggler.

(B) Lifetime Improvement: The RW improves the Touschek lifetime component of the electron beam through bunch lengthening. However, the Touschek lifetime depends not only on the bunch length, but on multiple interconnected parameters that may be affected by the operation of the RW. For example, the Touschek lifetime is proportional to the cube of the momentum acceptance (comp. Eq. 2.88). But the value of the dispersion function at the RW, necessary to increase the effect on the damping redistribution of the RW, has in turn a negative impact on the momentum acceptance as it increases the momentum compaction factor α (comp. Sec. 3.3.1, Fig. 3.12b). So in this case, although the RW could work properly regarding the damping redistribution and bunch lengthening, the net effect on the lifetime may be lost because the momentum acceptance is too small.

In Fig. 2.15, the theoretically achievable beam lifetime as a function of the damping partition was presented. The lifetime does not increase linearly with decreasing D, but the slope is getting steeper towards negative D. In fact, close to D equal zero, the lifetime is actually decreasing for decreasing D. Therefore, a major effect on the lifetime can only be achieved if the RW is working at the full extent regarding its intentional ability to alter D to values below -1.75. For example, a lifetime increasing effect of more than $50\,\%$ occurs for damping partitions smaller than -1.5 only. In Fig. 3.2 the damping partition is plotted as a function of field and gradient of the poles of the wiggler. The wiggler is assumed to have a total length of $1.1\,\mathrm{m}$,

fringe fields were neglected, and the field was assumed to follow a step function when transcending from the field of one pole to the field of the consecutive pole. This showed to be a reasonable approximation for a real device of length $1.9\,\mathrm{m}$, with sinusoidal fields and distances between the poles. Furthermore it was assumed that the dispersion at the wiggler has a value of $\eta_x = 1.0\,\mathrm{m}$.

In order to achieve a value of $D = -2$ for the damping partition, an on-axis field of $B_y \approx 1.2\,\mathrm{T}$ together with a gradient to that field of $\partial B_y/\partial x \approx 15\,\mathrm{T\,m^{-1}}$ are required. To obtain a lifetime improvement of $100\,\%$, D needs to have a value around -1.75 (green line in Fig. 3.2), i.e. an on-axis field of e.g. $\sim 1\,\mathrm{T}$ with a gradient of $\sim 15\,\mathrm{T\,m^{-1}}$ is be required. If only e.g. $80\,\%$ of these values for either field or gradient are met, the lifetime improvement is below $50\,\%$. As the desired lifetime improvements do not scale linearly with the excitation strength of the RW, it is crucial that the requirements for field and gradient are met to full extent.

(C) Accelerator Optics: The MLS is a reliable and successfully established synchrotron light source. A modest impact of the RW on the accelerator optics is desirable, so that the RW optics are comparable to the current standard user optics. Therefore, the RW's focussing characteristics have to be moderate compared to the remaining focussing elements in the accelerator. As the RW consists of alternating poles, vertical focussing due to edge focussing cannot be avoided. But, as proven by many well running 3rd generation light sources, the additional vertical focussing of insertion devices can be compensated by the remaining quadrupoles in the lattice (Clarke, 2004).

The horizontal gradient of the field in the poles of the RW will additionally generate horizontal focussing. Both, horizontal and vertical focussing, depend on the number of poles of the device. In Fig. 3.8, the tracked transfer matrix elements R_{21} and R_{43} for RW's with different numbers of poles are presented. The higher the number of poles, the lower the net focussing due to the smaller integration length of the individual pole (the focal length in thin lens approximation: $f = 1/kl$). However, with increasing number of poles and constant excitation current density in the coils, the on-axis field and the gradient reduce. Therefore, the integrated field times gradient decreases with an increasing pole number. With a reduced integrated field times gradient, the effect on the damping redistribution and on the lifetime (B) is jeopardized.

(D) Transparency: The RW, like any insertion device, has to be magnetically transparent: an on-energy particle entering the device on the reference orbit has to exit the device on the same orbit (comp. Fig. 3.9b). In other words, the device should not produce any additional angles or offsets. Referring to Sec. 3.2.3, this
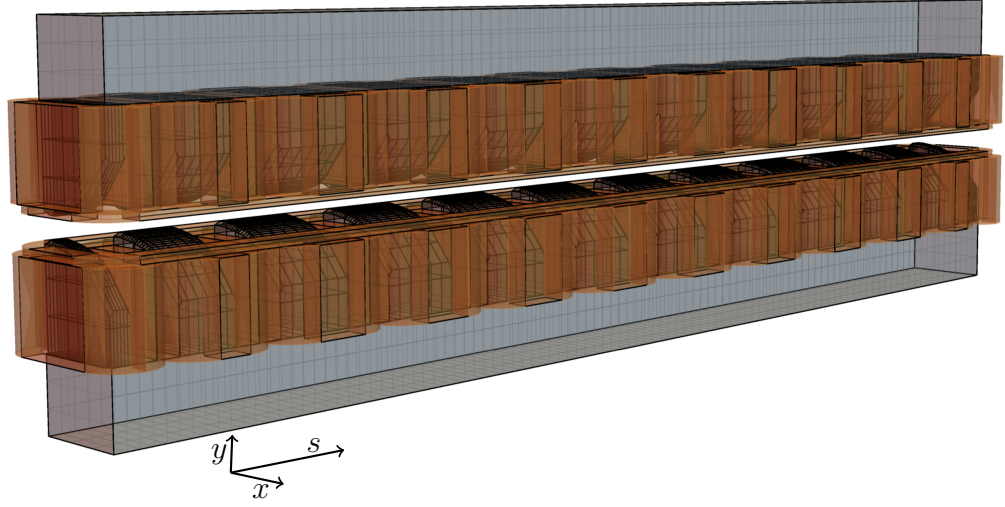
Figure 3.3: Design option for the normal conducting RW consisting of twelve poles (incl. endpoles). Gray: yoke, copper: coils.

requirement is particularly challenging for the RW as the gradient introduces a ponderomotive drift (comp. Fig. 3.9a) which needs to be compensated.

The above mentioned constraints set limits to the design parameters of the RW. Another constraint arises from non-linear field components of the device and their effects on the chromaticities without excited sextupoles (see next section). The normal conducting design of the RW is derived in the following section and in the consecutive sections its characteristics are studied.

3.2 Normal Conducting Design

In this section, a possible layout for the normal conducting RW for the MLS is presented. In Sec. 3.6 a superconducting alternative with its advantages and disadvantages over the normal conducting design is discussed.

The tool used for the hardware design of the RW is the `RADIA` package (version 4.29) (P. Elleaume, 1997; O. Chubar, 1997). `RADIA` is a `Mathematica` (Wolfram Research, Inc., 2016) add on and features simulation techniques for numerous kinds of magnets using the mathematical framework of `Mathematica`. In Sec. A.1, the `Mathematica` notebook for producing the normal conducting RW model for the MLS is given. After specifying the number of poles and the maximum length of the device, the individual lengths of the poles are adjusted automatically.

In the following section, an option for the pole shape is derived. After that, a

consideration for the number of poles is presented. In Sec. 3.2.3 the ponderomotive drift, arising from the gradient in the field, is presented together with the planned compensation scheme. In the end, the resulting design is introduced, whereas a picture is given here already with Fig. 3.3 in order to provide an overview for the following.

3.2.1 Poleshoe Design

The optimum pole shape for a multipole magnet with a ferromagnetic yoke can be derived by the equipotential lines of the scalar potential of the desired magnetic field. The underlying physics can be obtained in full detail in numerous sources, e.g. (Wiedemann, 2007; Russenschuck, 2010). Here, a reduced version of (Wiedemann, 2007) is presented:

The magnetic field in a current free region is derived by a scalar potential $V(x, y, z)$. V is a solution of the Laplace equation

$$\Delta V = 0. \tag{3.1}$$

The magnetic field is then derived by

$$\boldsymbol{B} = -\boldsymbol{\nabla} V. \tag{3.2}$$

For simplicity, the azimuthal variation of V is neglected in order to derive the profile for the transverse plane in the centre of a long magnetic pole. The potential for single higher order multipole components can be derived in Cartesian coordinates (Wiedemann, 2007):

$$V_n(x, y) = -B\rho \cdot \frac{1}{n!} A_n (x + iy)^n, \tag{3.3}$$

where $B\rho$ is the beam rigidity, n is the multipole order and A_n are the potential coefficients.

The imaginary part of the potential yields the normal components of the multipoles, whereas the real part of the potential yields the skew components of the multipoles. The imaginary part is(Wiedemann, 2007):

$$\Im\left[V_n(x, y)\right] = -B\rho \cdot \sum_{m=1}^{(n+1)/2} A_{n-2m+1,2m-1} \frac{x^{n-2m+1}}{(n-2m+1)!} \cdot \frac{y^{2m-1}}{(2m-1)!}. \tag{3.4}$$
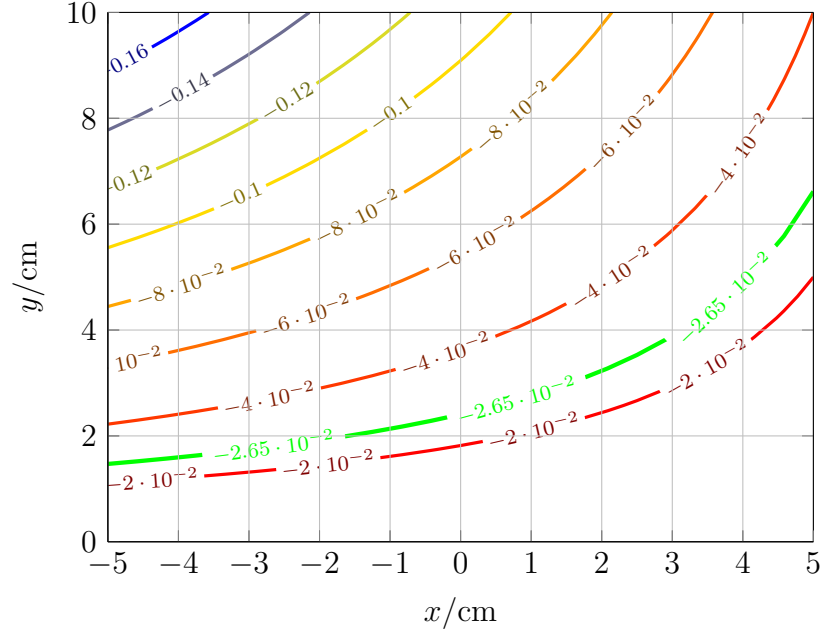
Figure 3.4: Equipotential lines in [T m] of $\Im\left[V_{\mathrm{CFM}}\right]$ for values of $B_y = 1.1\,\mathrm{T}$ on-axis and $\partial B_y/\partial x = 14.0\,\mathrm{T\,m^{-1}}$.

Here, the potential coefficients have been rewritten as $A_{j,k}$, where the sum of j and k is the multipole order and k gives information about the rotation of the magnet around the azimuth. For upright magnets, i.e. no skew magnets, k is equal to 1. For skew magnets k is zero.

The RW consists of an alternating sequence of combined function magnets. These combined function magnets should have a dipole and a quadrupole field component. Writing $\Im[V]$ up to $n = 2$ gives:

$$\Im\left[V_{\mathrm{CFM}}\right] = -B\rho \cdot \left[\underbrace{A_{0,1}}_{=\frac{1}{\rho}}\, y + \underbrace{A_{1,1}}_{=k_x=\frac{1}{B\rho}\frac{\partial B_y}{\partial x}}\, xy \right]$$

$$= -\left[B_y y + \frac{\partial B_y}{\partial x} xy \right]. \tag{3.5}$$

In Fig. 3.4, the resulting potential is presented for values of $B_y = 1.1\,\mathrm{T}$ on-axis and $\partial B_y/\partial x = 14.0\,\mathrm{T\,m^{-1}}$. The optimum pole shape is characterized by the equipotential line that is closest to the particle beam, in order to keep the excitation currents small, while simultaneously being far enough from the beam so that the vacuum chamber can fit between the pole tips. The vacuum chamber for the RW has a full height (including walls) of 28 mm, which is the same value as for the undulator chamber. The same design as for the undulator chamber was used for the RW cham-

(a)

(b)
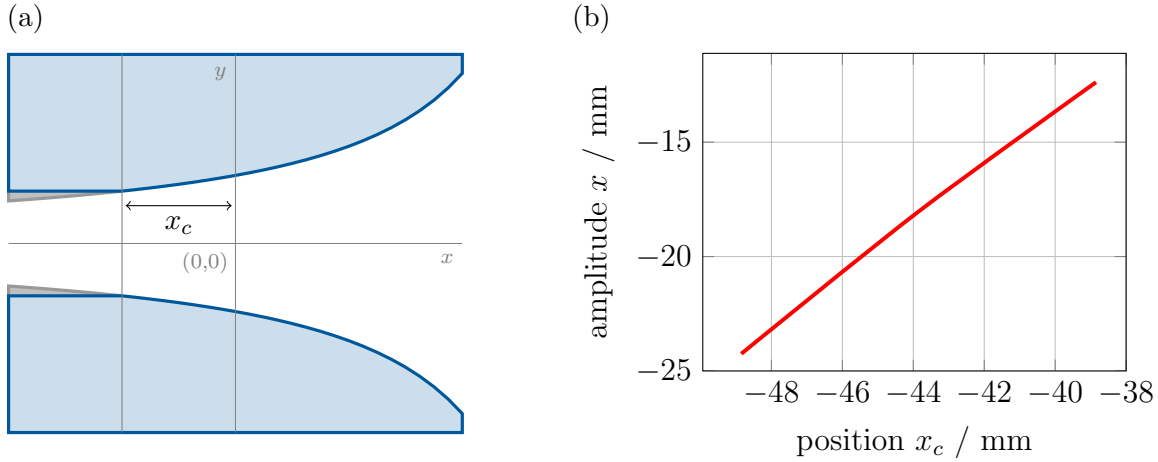
Figure 3.5: Explanatory scheme for horizontally cutting the pole shape in order to bring the pole tips closer together (a). The initial horizontal amplitude for which particles get defocused as a function of the horizontal starting position of the parallel pole tip area x_c relative to the reference orbit (b).

ber in order to not further minimize the vertical aperture. Therefore, the minimum gap between the pole tips has to be larger than $28\,\text{mm}$. In Fig. 3.4, the green line represents the equipotential line chosen for the RW poles. At the narrowest place $(x = -5\,\text{cm})$ it leaves a total gap of $29.4\,\text{mm}$, enough for the vacuum chamber to fit in between.

In the equation for the ideal pole tip x and y can take any value between $\pm\infty$. A real life magnet has finite dimensions, which means that at some point on the hyperbolic surface, the yoke has to be cut. As the poles dimensions are finite, the field linearity and purity are limited (higher order multipoles occur).

Furthermore, it is essential to keep the sloped surface to the full extent of the horizontal pole dimensions. In the scope of this work the effects of a horizontal cut in the hyperbolic pole shape were studied (comp. Fig. 3.5a). Vertically, this cut should bring the two poles closer together in order to increase the on-axis B_y and with that the effect on the damping partition D. However, doing so, the field between the parallel pole tip areas becomes more "dipole like". The ponderomotive drift (see Sec. 3.2.3) between the parallel areas is reduced. Therefore, the correction coil is overcompensating the drift in that area and the particles get defocused. This effect is important, as it significantly cuts into the momentum acceptance. In Fig. 3.5b, the y-axis describes the horizontal initial amplitude of a particle that becomes defocused due to the overcompensating correction. Particles with initial amplitudes smaller than the values plotted here are also defocused. The x-axis in Fig. 3.5b shows the horizontal starting position of the parallel pole tip area (x_c in
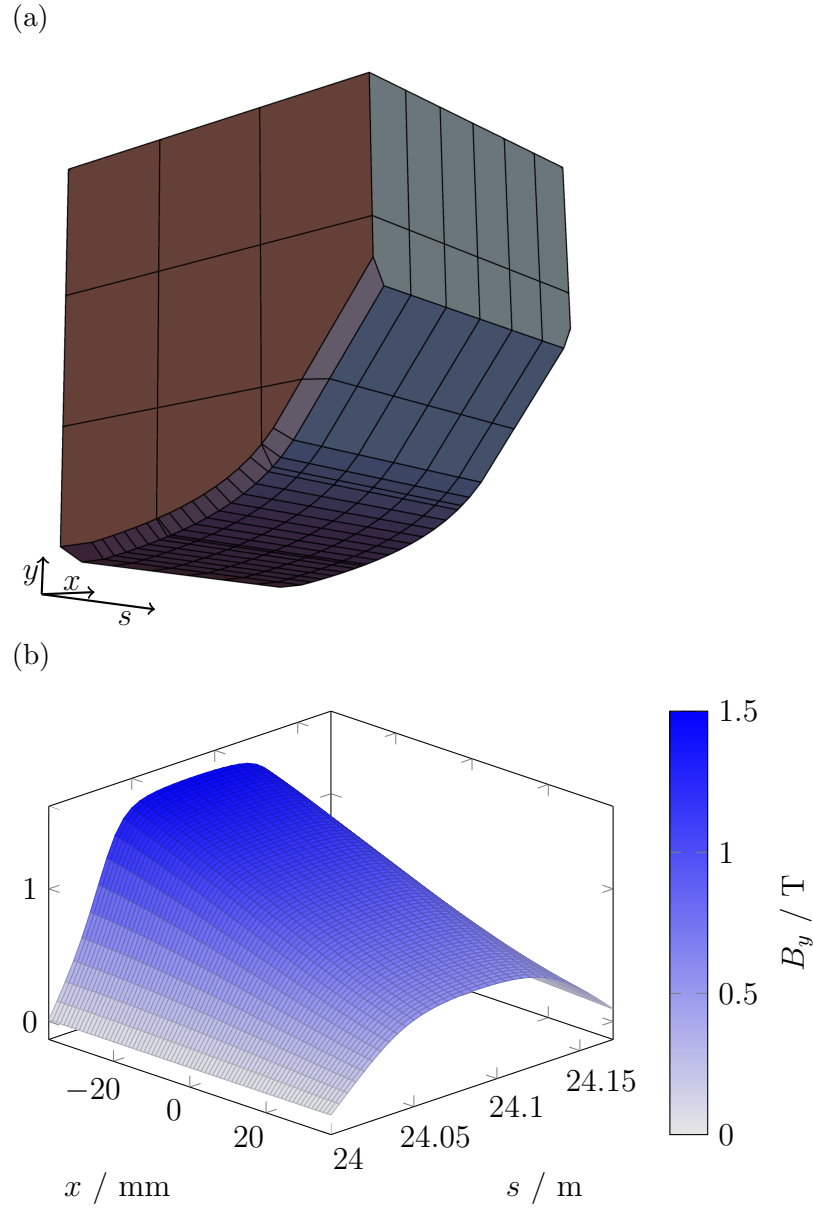
(a)

(b)

Figure 3.6: Final pole design for the RW, including chamfers (a). Field distribution in the median plane for a single pole as part of the RW (b).

Fig. 3.5a and 3.5b). From x_c to the end of the pole tip in direction of negative x, the pole tips are parallel. This correlation between defocussing and starting position of the parallel pole tip area is crucial for the design. Hence, the sloped surface (be that hyperbolic or tangential to it) needs to be maintained to the full horizontal extent of the poles.

In Fig. 3.6a, the suggested pole design is presented. The chamfers were included to reduce saturation effects during the ramping of the RW.

(a)   (b)
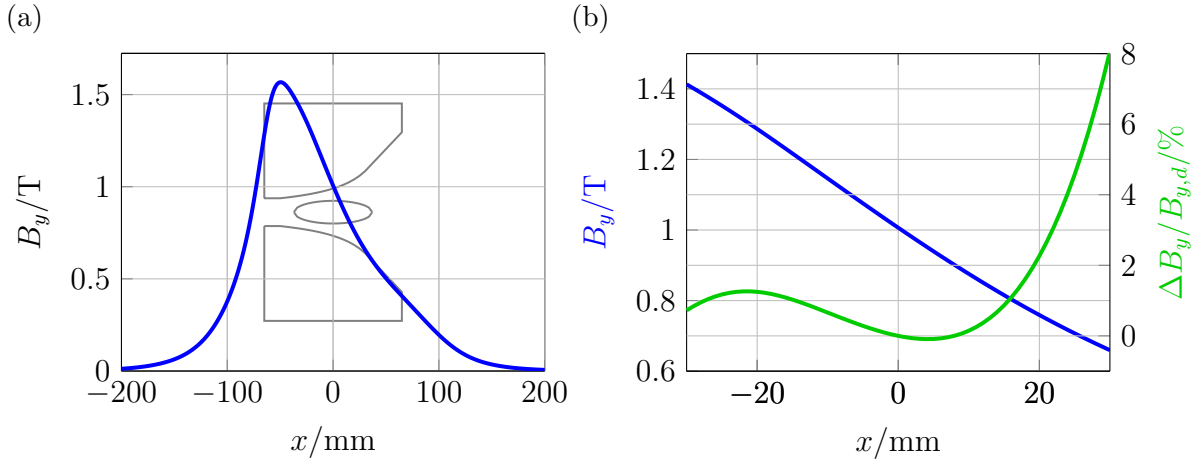
Figure 3.7: Vertical field component as a function of horizontal position in the centre of a single pole as part of a twelve poled RW (a). Deviation from linearity for a region $r = \pm 30\,\mathrm{mm}$ inside the vacuum chamber (b). $\Delta B_y = B_{y,d} - B_y$, where $B_{y,d}$ is the design field (multipole orders 0 and 1) and B_y the actual field.

Pole Shoe Material

Considering the necessary high field strengths in order to alter the damping partition, the choice for the yoke material of a normal conducting device appears to be a Cobalt-Iron steel called "AFK502" in `RADIA`. It is a compound of 49 % Fe, 49 % Co, and 2 % V and yields a high saturation induction of 2.35 T, which is higher than most materials are able to achieve. Other materials like standard iron steels were also considered, but the fields yielded by these materials are not high enough to achieve the desired effect on the damping redistribution while simultaneously keeping a high number of poles in order to minimize the impact on the accelerator optics (comp. Sec. 3.2.2).

As the Cobalt content of the material might get activated by beamlosses in the material or shielding components, preliminary studies have been conducted by the radiation protection group of HZB with `FLUKA` (Ferrari et al., 2005): the preliminary results indicate that the activation is not critical. However, these studies are not finalized, yet. More detailed studies including backscattered neutrons from the concrete shielding have to be conducted.

In Fig. 3.6b, the field distribution for one pole pair in the centre of a RW with twelve poles is presented. The field decreases with increasing horizontal amplitude. The horizontal field distribution in the centre of the pole is depicted in Fig. 3.7a. The contained multipoles are listed in Tab. 3.1. The multipoles are calculated as

part of a Taylor series (Russenschuck, 2010):

$$B_y(x) = B_{y,0} + \frac{\partial B_y}{\partial x} \cdot x + \cdots + \frac{1}{n!}\frac{\partial^n B_y}{\partial x^n} \cdot x^n = \sum_{n=0}^{N} \frac{1}{n!}\underbrace{\frac{\partial^n B_y}{\partial x^n}}_{c_n} \cdot x^n. \qquad (3.6)$$

The multipole coefficients c_n were calculated in the horizontal arbitrarily chosen interval between $\pm 30\,\text{mm}$. The dipole and quadrupole component are the "design" multipole components wanted. Assuming that the achieved dipole and quadrupole component meet the requirements in a perfect way, it is possible to calculate the relative field error introduced by the higher order multipole components at distance r from the centre:

$$\Delta B_r = \frac{B_y(r) - B_d(r)}{B_d(r)}. \qquad (3.7)$$

$B_y(r)$ is the magnetic field including higher order multipoles and $B_d(r)$ is the design field excluding higher order multipole components. The errors introduced by the higher order multipoles for the ten, eleven and twelve poled RW solutions at $r = \pm 30\,\text{mm}$ are:

$$\Delta B_{r,10} = 3.95\,\%, \quad \Delta B_{r,11} = 4.44\,\%, \quad \Delta B_{r,12} = 4.81\,\%.$$

The relative field error of higher order multipoles increases with increasing the pole

Table 3.1: Multipole coefficients as derived in Eq. 3.6 contained in the vertical field component in the median plane ($y = 0$) between $x = \pm 30\,\text{mm}$ for different numbers of poles.

n	$\partial^n B_y/\partial x^n$		
	10 poles	11 poles	12 poles
0	1.1927	1.1002	1.0172
1	-1.4513×10^1	-1.3878×10^1	-1.3207×10^1
2	7.1248	1.5738×10^1	1.9373×10^1
3	5.1300×10^3	4.3552×10^3	4.0563×10^3
4	2.3466×10^5	2.3430×10^5	2.1312×10^5
5	-1.9383×10^7	-2.7770×10^7	-4.3367×10^7
6	-2.2774×10^9	-3.1824×10^8	3.0675×10^9
7	7.3302×10^{11}	9.4700×10^{11}	1.3190×10^{12}
8	-4.0323×10^{13}	-1.1008×10^{14}	-2.3856×10^{14}
9	-1.1313×10^{16}	-1.1006×10^{16}	-8.6981×10^{15}

number, as the on-axis "design" B_0 and gradient decrease. However, the relative error of higher order multipoles does not yield information about the absolute values of the higher order multipoles. For example, the octupole component c_3 reduces with increasing pole number, whereas the sextupole component c_2 increases.

3.2.2 Number of Poles

The choice of the number of poles influences both the focussing characteristics and the achievable on-axis fields and gradients of the RW. The higher the number of poles, the lower the impact on the accelerator optics (comp. Fig. 3.8 -R_{21} and R_{43}). But the lower the number of poles, the higher the attained field and gradient (comp. Fig. 3.8 -$B_y \partial B_y / \partial x$). A low impact on the optics is desirable, but without the necessary field, the original intention of improving the lifetime would not be achieved.

Taking a closer look at the focussing characteristics, a difference between odd and even numbered poles appears. Considering the horizontal plane (R_{21}) it is favourable to choose an odd number of poles (connected by the green dashed lines in Fig. 3.8). For the vertical plane (R_{43}) the even numbered solutions yield slightly less focussing (connected by the red dashed lines in Fig. 3.8). Considering the focussing and the achievable field times gradient, a number of poles between ten and twelve seems preferable. Overall, it appears worthwhile to pick an odd numbered solution. Especially a solution with eleven poles yields small additional focussing in the horizontal plane while the field strengths are still high enough to achieve the desired effect on the damping.

Besides the linear beam optics, the chromatic effects of such a device have to be considered. The chromatic effect of the RW depends on energy dependent focussing inside the RW, caused by gradient, dispersion, and in particular the octupole component. The impact of this energy dependent focussing is very strong, as can be seen in Tab. 3.2, where the chromaticities, without excited sextupoles, of the MLS with

Table 3.2: Chromaticities, without excited sextupoles, of the MLS with RW's with different numbers of poles.

	ξ_x	ξ_y
SU w/o RW	-3.4904	-3.9929
RW 10 poles	5.0205	-5.6184
RW 11 poles	3.3264	-5.9562
RW 12 poles	0.5714	-5.6227

RW, for different numbers of poles, are presented. Comparing the horizontal chromaticities with the octupole components listed in Tab. 3.1, the correlation between the two can be observed.

The ten poled RW solution increases the horizontal "natural" chromaticity by $\Delta\xi_x = 8.51$, which is too high to compensate using the existing sextupoles. According to simulations, it is possible to tune the chromaticities below 1 in both planes for the eleven poled solution. However, it is not possible to tune the chromaticities below 0.8. For the twelve poled solution, the span is not as high as for the eleven and ten poled solution. Here, the "natural" chromaticities can be compensated with the existing sextupoles, and even negative chromaticities can be set up. Therefore, only the twelve poled RW is reasonable as the chromaticity without excited sextupoles can be compensated by the existing sextupoles and the chromaticities can be tuned in a wider range.

3.2.3 Ponderomotive Drift and Correction Scheme

In Fig. 3.9a, the trajectories of particles with different energies through a RW is displayed. The amplitude of the field decreases with increasing x. The particles drift towards the low field region, i.e. towards positive x. The reason for this is that the gradient in the field introduces a ponderomotive force acting on the particles: the horizontal kick, a particle accumulates in a high field amplitude region of one pole cannot be compensated in the lower field amplitude region the particle experiences in the consecutive pole. Therefore, a net force drives the particles towards the low field region. The strength of this force depends on the accumulated kick and therefore on the length of the poles and the gradient. The longer the poles (the smaller the pole number), the stronger the ponderomotive drift.

The ideal compensation scheme would be to vary the pole length of every second pole. Those poles in which the particles travel through a weak field region have to be lengthened in order to achieve the same integrated field as in the poles where the particles travel through the strong field region. However, this solution is static. It would not be possible, for example, to change the polarity of the device if wanted. A sufficient and easy manufacturable solution is to correct the drift by introducing a single longitudinal coil pair, which spans the complete length of the RW to continuously correct the drift (comp. Fig. 3.10). In contrast to the pole lengthening, the correction coil creates additional horizontal focussing: low energy particles travelling through the high field region experience a stronger ponderomotive force, whereas high energy particles travelling through the low field region experience a
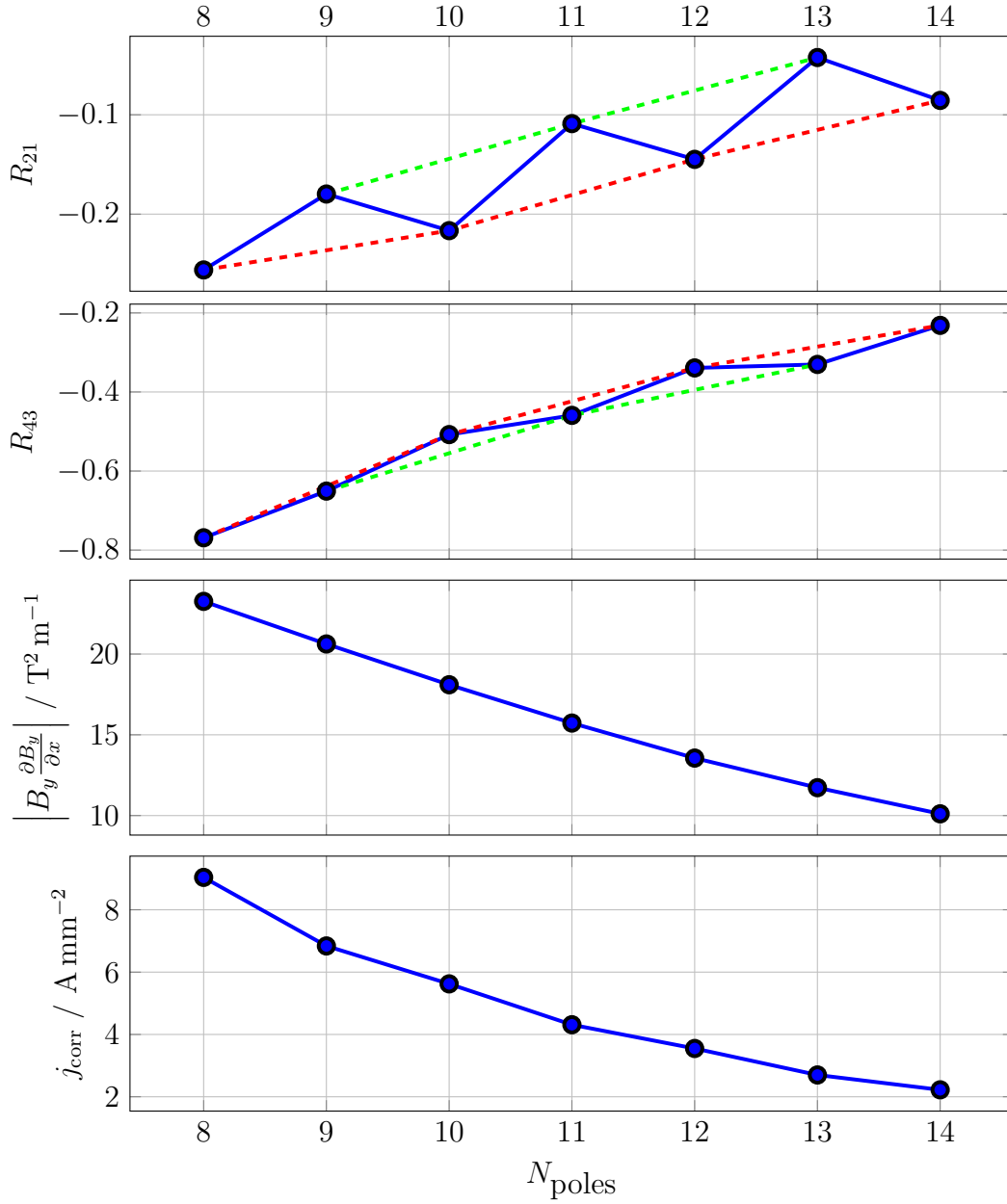
Figure 3.8: Different quantities as a function of the number of poles in the RW. The excitation current density of the main poles was kept constant, as well as the overall length of the device. The ratio between coil width and pole length was kept constant at 0.6. Therefore, the value of ampere turns per coil decrease with increasing pole number. The top two plots show the tracked R_{21} and R_{43} (comp. Sec. 2.1.7), describing the net focussing in the horizontal and vertical plane respectively. The third plot shows the product of field and gradient in the centre of one of the main poles. The last plot shows the necessary excitation current density in the corrector coil in order to compensate the ponderomotive drift.

(a)

(b)
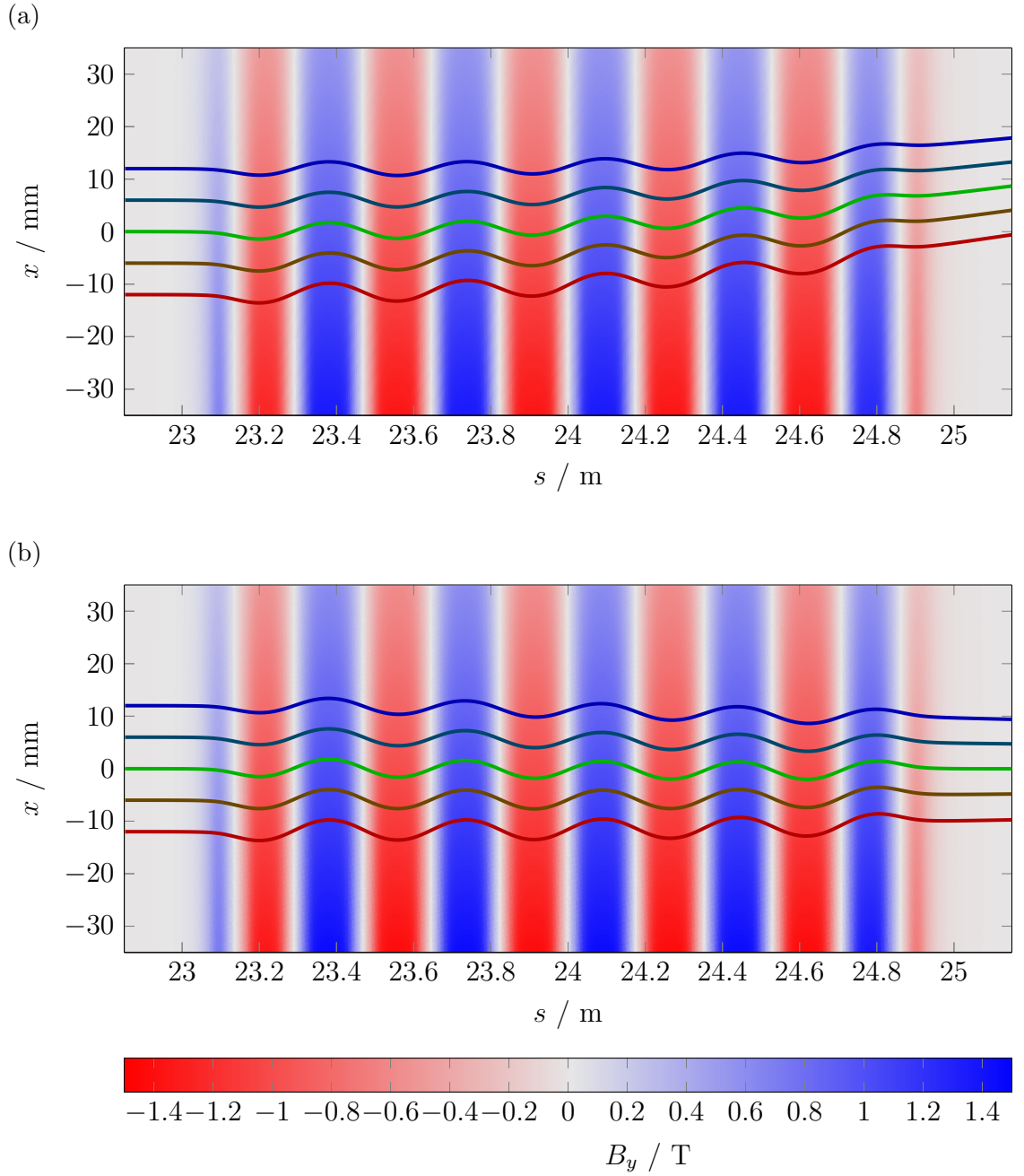
Figure 3.9: Vertical field distribution for a non-transparent (a) and transparent (b) device with twelve poles in the $y = 0$ - plane together with corresponding particle trajectories. The particles have different momentum deviations between $\pm 1\%$ and are sorted by dispersion $\eta_x = 1.2\,\text{m}$. The blue trajectory corresponds to the high energy particle, red corresponds to the low energy particle.

smaller ponderomotive force. The corrector coil, inducing merely a dipole field,
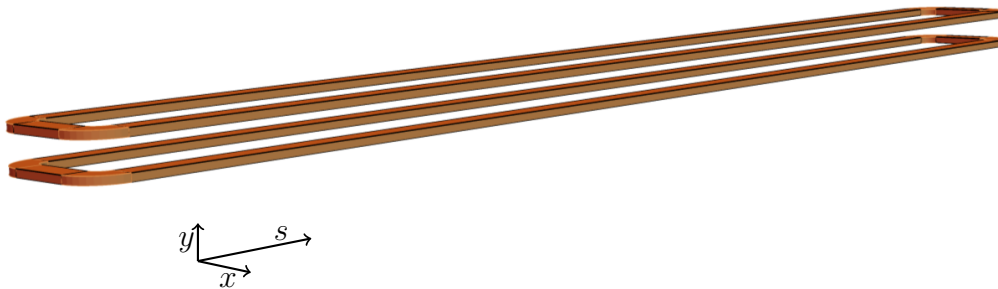
Figure 3.10: Longitudinal corrector coil, spanning the complete length of the RW, used to compensate the ponderomotive drift.

will overcompensate the ponderomotive drift of high energy particles whilst under-compensating the drift of low energy particles. For the twelve poles solution, this additional focussing can be compensated by the quadrupoles in the lattice.

The current density j_{corr} inside the corrector coil, necessary to correct the ponderomotive drift, is presented in Fig. 3.8. As expected, the necessary current density decreases with increasing the number of poles. In Fig. 3.9b, the resulting trajectories tracked through a twelve poled RW with applied corrector coil are presented. As can be seen, the device becomes transparent for the reference particle, whereas off-axis particles experience horizontal focussing.

3.2.4 Resulting Design

Because of the reasons derived in the previous sections, the preferred normal conducting design is a twelve poled RW. The twelve poles are constituted of eight main poles and four end poles. The outer end poles have quarter the length of the main poles, whereas the inner end poles have three quarters of the length of a main pole:

$$+1/4, -3/4, +1, -1, \ldots, +1, -1, +3/4, -1/4.$$

The sign indicates the polarity of the pole. Such an arrangement was chosen in order to have the beam undulating around the centre of the vacuum chamber instead of an off-axis oscillation. In Fig. 3.3, the wiggler is presented. The correction coil pair used to compensate the ponderomotive drift can be seen close to the pole tips, spanning the complete length of the device.

The nominal operating current density for the main coils is set to $j_{\text{main}} = 7.1\,\text{A}\,\text{mm}^{-2}$. In Fig. 3.11b, the on-axis B_y and $\partial B_y/\partial x$ are illustrated as a function of the current density j_{coil} in the coils. For high current densities above $\sim j_{\text{main}}$, the

(a)   (b)
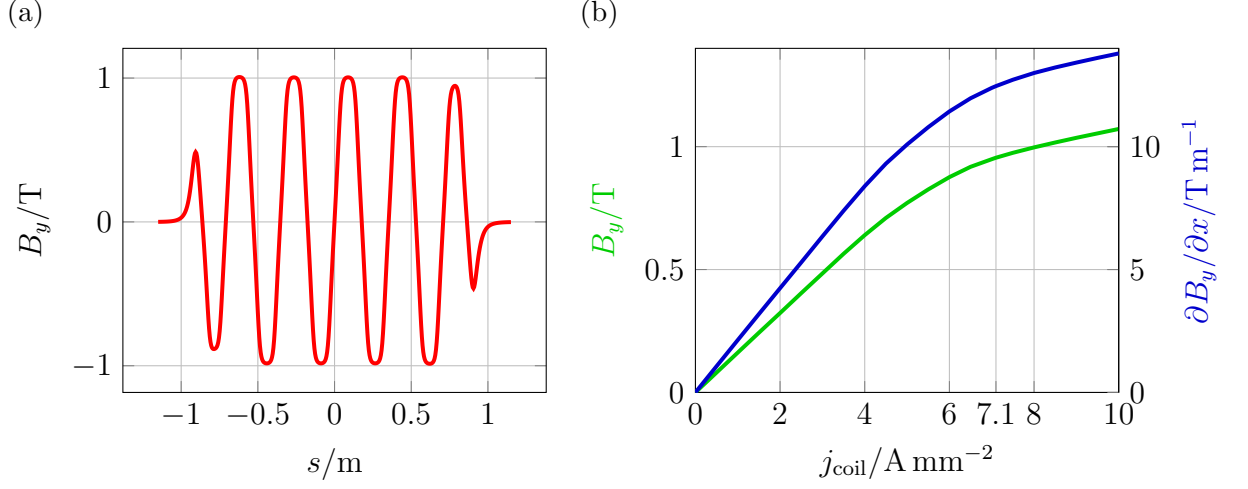
Figure 3.11: The on-axis B_0 as a function of the longitudinal position (a). The on-axis B_0 and gradient as a function of the excitation current density j_{coil} in the coils (b). The correction coil pair was switched off.

magnetic field saturates and the gain in field by increasing the current is reduced. Therefore, $7.1\,\mathrm{A\,mm^{-2}}$ were chosen to conduct the simulations. This gives some margin for increasing the current density if required.

Generally, the maximum current density for normal conducting devices with water cooled coils is $\sim 10\,\mathrm{A\,mm^{-2}}$ (Russenschuck, 2010). Therefore, looking at Fig. 3.11b, the performance of the twelve poled RW can be pushed by another $24\,\%$ when increasing the current density to the maximum.

With a current density of $7.1\,\mathrm{A\,mm^{-2}}$, the twelve poled RW is able to alter D by

$$\Delta D = -1.49 \cdot \langle \eta_x \rangle_{\mathrm{RW}}\,\mathrm{m^{-1}}.$$

This result has been determined by integrating B_y and the field gradient along the reference trajectory through the field map (green line in Fig. 3.9b). The bare MLS lattice has a damping partition of $D = -0.055$. Therefore, with a dispersion of $1\,\mathrm{m}$ at the wiggler, the damping is shifted to -1.545. If a dispersion of $1.2\,\mathrm{m}$ is set up, the damping would shift to -1.845, beyond the desired value of -1.75, and therefore fully enabling the desired effect on the damping. Together with the additional margin for the current density, the twelve poled RW would be able to reach values of $D = -2$ for the damping partition.

In Fig. 3.11a, the on-axis field is presented as a function of the longitudinal position. The overall length of the device is limited to $1900\,\mathrm{mm}$ by the available

length in the short straight section opposite to the septum magnet. With twelve poles, the period length is therefore $\lambda_{\mathrm{RW}} = 353.6\,\mathrm{mm}$. Together with the average on-axis peak field $B_y = 0.99\,\mathrm{T}$ the deflection parameter K becomes

$$K_{\mathrm{RW}} = \frac{eB_y\lambda_{\mathrm{RW}}}{2\pi mc} = 32.508. \tag{3.8}$$

With an deflection parameter $K \gg 1$, the RW is expected to be a wiggler indeed regarding its radiation characteristics (Clarke, 2004). This is discussed in detail in Sec. 3.5.

3.3 Beam Optics Development

3.3.1 Dispersion

The value of the dispersion function η_x at the position of the RW determines the impact on the damping redistribution of the RW. In I_4 (Eq. 2.38) it is part of the product that is aimed to be controlled by the RW, and therefore the dispersion is a lever on how much the RW influences the damping distribution in a specified optic. As the field strengths, achieved by normal conducting devices, are limited to $1\,\mathrm{T}$ to $2\,\mathrm{T}$, it is worthwhile to have the dispersion as high as possible at the place the RW is installed. Doing so, lower field strengths of the RW are sufficient to achieve the same ΔD. The advantage is that the number of poles may be increased, resulting in a lower net focussing and lower "natural" chromaticity (comp. Fig. 3.8 and Sec. 3.2.2).

However, at the MLS, one major constraint is that the dispersion needs to be close to zero at the septum magnet. In Fig. 3.12a, the resulting current times lifetime as a function of the set up dispersion at the septum magnet is presented. Even small values of the dispersion of several cm have a measurable impact on the lifetime.

With this constraint arises another limitation: when keeping the dispersion zero at the septum and increasing the dispersion at the RW (the opposite side of the synchrotron), the integrated dispersion in the dipoles, and therefore the momentum compaction factor α, increases. Increasing the momentum compaction factor in turn decreases the rf-acceptance as in Eq. 2.73:

$$\delta^2_{\mathrm{acc,rf}} \propto |\eta_c|^{-1} \approx |\alpha|^{-1}.$$

In Fig. 3.12b the momentum acceptance for different rf-voltages and without cavity
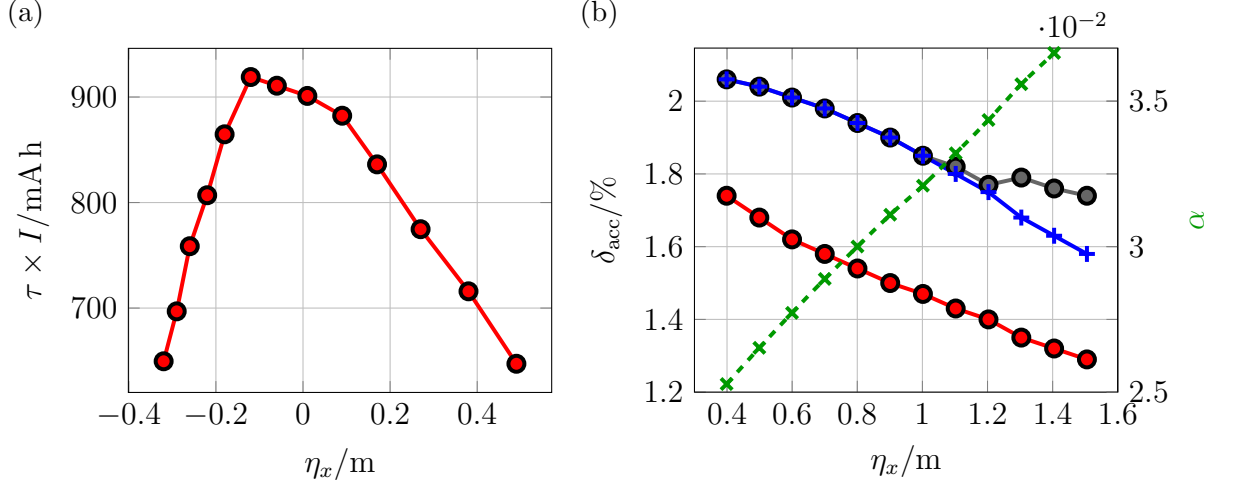
Figure 3.12: Measured current times lifetime as a function of the set up dispersion η_x at the septum magnet (a). Tracked momentum acceptance for matched electrons, neglecting synchrotron radiation, as a function of the dispersion at the RW for cavity voltages of $800\,\mathrm{kV}$ (blue), $500\,\mathrm{kV}$ (red), and without cavity (grey) for standard user operation mode at the MLS without RW (b). In green, the evolution of the momentum compaction factor α is presented.

is presented as a function of the dispersion at the wiggler. The evolution of α is indicated by the dashed green line.

In conclusion, the dispersion at the Wiggler has to be maximized without decreasing the acceptance below $1.15\,\%$ (comp. Sec. 2.4.1, geometrical acceptance), so that the acceptance does not counteract the lifetime increasing effect. A dispersion at the Wiggler of $1.1\,\mathrm{m}$ proves to be worthwhile (comp. Fig. 3.13). With increasing the dispersion at the RW from the standard user optics value of $0.8\,\mathrm{m}$ to $1.1\,\mathrm{m}$, the gradient in the long straights becomes steeper while decreasing the peak dispersion in the DBA structures in the vicinity of the RW (comp. Fig. 3.13). However, the global maximum value for the dispersion is maintained and is still located in the DBA structures in the vicinity of the septum magnet. This is a crucial point, as the geometric acceptance depends on the ratio between dispersion and free aperture and may become limiting if the peak dispersion increases (Eq. 2.75).

In Fig. 3.19, a close up of the evolution of the dispersion function inside a twelve poled RW is presented.
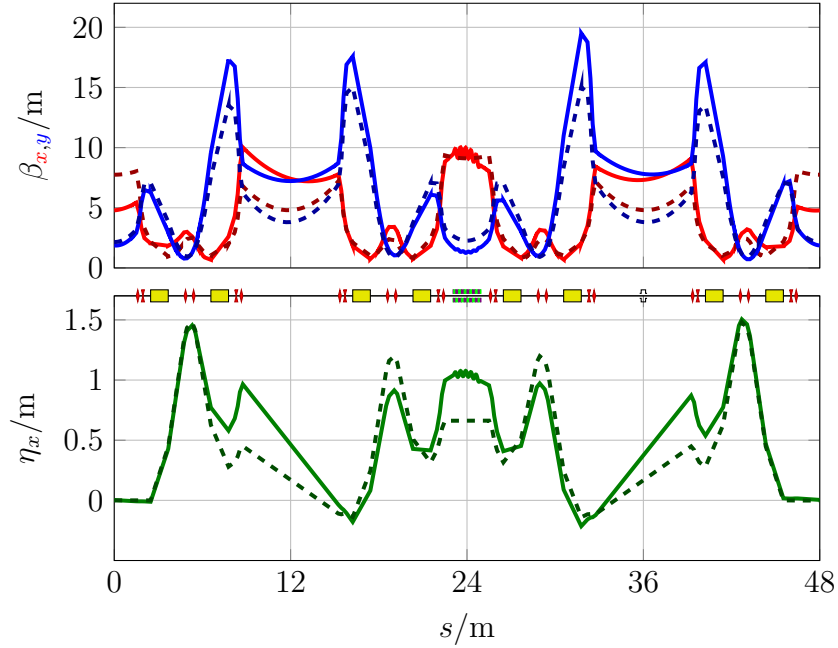
Figure 3.13: Comparison of the β-functions and dispersion for standard user operation mode (dashed) and for the RW lattice (solid).

3.3.2 β-functions

For the MLS, the β-functions are usually chosen to be smaller than $20\,\mathrm{m}$ to $25\,\mathrm{m}$. The reason for this are halo particles, that are more likely to get lost for high β-functions, and the source size of the emitted synchrotron radiation. Therefore, an arbitrary upper limit of $20\,\mathrm{m}$ for the β-functions was set.

In Fig. 3.13, the optimized β-functions for a twelve poled RW are presented together with the ones for the standard user operation mode for comparison. Due to the additional vertical focussing of the device, the maxima of the vertical β-function increase from $\sim 15\,\mathrm{m}$ to $20\,\mathrm{m}$. In Fig. 3.19, a close up of the evolution of the β-functions inside the wiggler is obtained.

In Sec. 4.2, the impact on the dipole beamline performance by the change of the optics will be discussed, whereas Sec. 4.3 covers the effects on the undulator beamline.

3.4 Dynamic Aperture & Error Estimations

During the design phase of an insertion device, the error margins on the designed field distributions have to be defined. The usual and straight forward way to do this is to define the error margins through the first and second field integral. The first

field integral

$$I_{F1} = \int_{-\infty}^{\infty} B_y(s) \, \mathrm{d}s \qquad (3.9)$$

is a measure for the exit angle, whereas the second field integral

$$I_{F2} = \int_{-\infty}^{\infty} \int_{-\infty}^{s} B_y(s') \, \mathrm{d}s' \, \mathrm{d}s \qquad (3.10)$$

is a measure for the position offset the particles accumulate in the horizontal (i.e. deflection) plane (Clarke, 2004). In order to have no deflection and no residual kick it is required to have $I_{F1} = I_{F2} = 0$. Assuming a planar device (i.e. no gradient and therefore no ponderomotive drifts), the allowed field errors can be defined through the ideal proximity of I_{F1} and I_{F2} to zero. The field integrals can be measured with a stretched wire along a straight line through the planar device.

With regard to the RW this approach could only be used for defining the field qualities when the correction coil is turned off. This approach is only of limited use when the device is in operation as the additional dipole field of the correction coil generates finite values of I_{F1} and I_{F2} for a transparent device if measured along a straight line. Along the trajectory of the reference particle, I_{F1} and I_{F2} are equally zero. However, the stretched wire measures along a straight line. Therefore this approach is not effective and defining the required field qualities is challenging.

For the wiggler in operation, the parameters of concern are deflection, angle, (dynamic) aperture and momentum acceptance. It is indeed time consuming to calculate the aperture for many different reasonable error settings. But it is also the most accurate method for the existing problem. To determine the allowed error amplitudes the following scheme was used:

1. Generation of a 3d field map without errors from the `RADIA` model of the device;

2. Application of different error types to the field map;

3. Determination of the (dynamic) aperture and momentum acceptance with `FTRACK` (see Sec. 3.4.1).

Depending on the granularity of the 3d mesh-grid on which the field map is generated, the field map can be an accurate description of the real device. Implementing the errors directly in `RADIA`, e.g. errors on the current in the coils or distortions of field vectors due to surface roughness, would be desirable. But, as generating a field

map with a certain granularity is time consuming (in the order of 24 h), this is not an appropriate approach. Instead, the field map is generated once for a "perfect" device and various error types are applied later. Another program was written that can read the number of poles from the given field map and calculates the multipoles of the vertical field component for each horizontal grid line. Errors are defined by the user and then applied to the field map. The applied errors change the transparency of the device. Therefore, it is essential to make the field map as transparent as possible again. `FTRACK`, described in Sec. 3.4.1, possesses this feature and calculates and applies the additional dipole field required for transparency (which, in case of the RW, is exactly what the correction coil does). If the tunes get mismatched by the additional dipole field (and focussing), `FTRACK` features the option to rematch the tunes, based on an iterative process including a predefined tune bump, using the quadrupoles in the lattice.

The field map with errors can thus be used in `FTRACK` in order to calculate the dynamic aperture and momentum acceptance. By comparing the dynamic aperture for the error free device with the one containing errors, the allowed error limits can be determined. The criterion for acceptable dynamic aperture is having more than 20σ free aperture in each transverse plane in order not to reduce the aperture significantly. This is combined with the criterion for the momentum acceptance: the momentum acceptance has to be given by rf-acceptance corresponding to $800\,\mathrm{kV}$ cavity voltage ($\delta_{\mathrm{acc,800\,kV}} = 1.7\,\%$ for $\alpha = 0.034$), which is a possible upgrade value for the existing $500\,\mathrm{kV}$ cavity.

In the following, `FTRACK` will be introduced, followed by calculations for the dynamic aperture. Finally, estimations for the allowed field errors for the twelve poled RW are presented.

3.4.1 `FTRACK`

Existing particle tracking codes like `MAD-X-PTC` (Deniau et al., 2015) lack the ability to properly include arbitrary field maps. Therefore, the program `FTRACK`[1] was developed. `FTRACK` features a symplectic integrator which enables tracking through arbitrary field maps. For the standard lattice components, `FTRACK` uses `MAD`-like routines for tracking through extended dipoles and quadrupoles, together with thin lens approximations for tracking through sextupole and octupole magnets (all ac-

---

[1]Naming the program `FTRACK` may imply that this code does have some official status. This is not the case. The name `FTRACK` is only used for simplicity. `FTRACK` is an in-house code, with contributions from our working group and especially (Scheer and Wüstefeld, 2014; Ries and Feikes, 2013-2016).
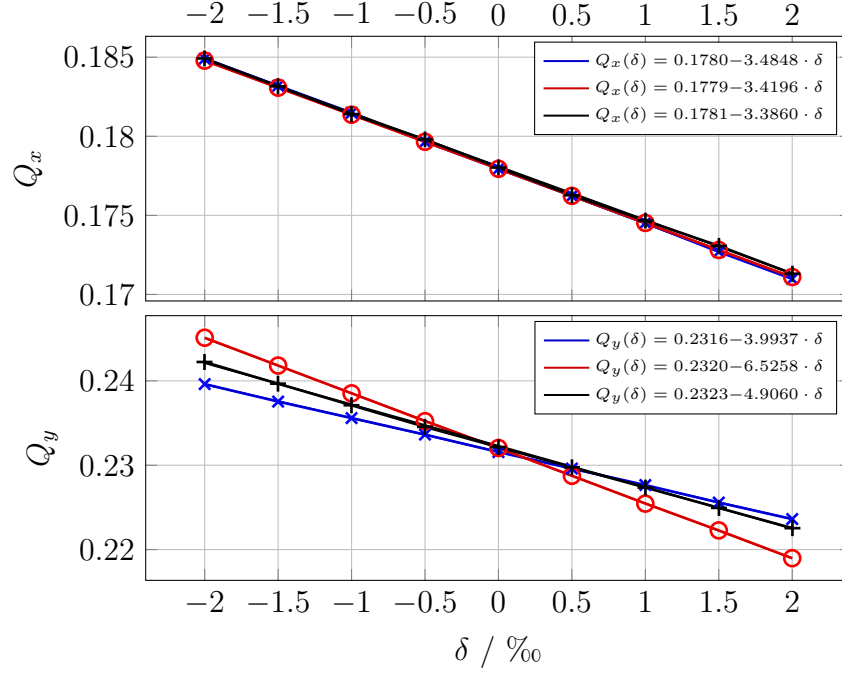
Figure 3.14: Tracked non integer parts of the tunes and fitted chromaticities for `MAD-X-PTC` (red) and `FTRACK` (blue). The cavity was turned off in both cases. Measured non integer parts of the tunes and fitted chromaticities for the standard user operation mode with sextupoles, skew quadrupoles and octupole turned off (black). A momentum deviation of $\delta = 0.5\,\text{‰}$ corresponds to a change in rf-frequency of $\Delta f = 7.5\,\text{kHz}$ (see Eq. 2.25).

cording to (Brown, 1968)).

The program does not feature the TWISS functionality of `MAD-X-PTC` but is indeed able to calculate the β-functions, dispersion, tunes, chromaticities and primarily the dynamic aperture and momentum acceptance through particle tracking. Matching the tunes in `MAD-X-PTC` and using the matched quadrupole strengths in `FTRACK` proofed to be functioning. Comparing the tunes between both programs for the standard user operation mode yields a deviation below accuracy for the horizontal tune (on-energy), and $0.02\,\%$ for the vertical tune (on-energy). The natural chromaticities for the standard user mode, calculated with both programs, deviate by $1.9\,\%$ for the horizontal plane and by $38.8\,\%$ for the vertical plane (compare also Fig. 3.14). In Tab. 3.3 the absolute values of the mentioned quantities are presented. The difference in the vertical chromaticity is mainly due to the different dipole routines used in `MAD-X-PTC` and `FTRACK`. Measuring the natural chromaticity at the MLS results in $\xi_{x,\text{meas}} = -3.39$ and $\xi_{y,\text{meas}} = -4.91$ (see Fig. 3.14). The value for the measured vertical natural chromaticity lies between the ones calculated by `FTRACK` and `MAD-X-PTC`. Both codes deviate from the measured

values. Therefore, slightly different sextupole settings will be used for the calcula-
tions in `FTRACK` in order to compensate the vertical chromaticity mismatch between
`FTRACK` and `MAD-X-PTC`.

It is also possible to generate 6×6 transport matrices for the given field maps
in `FTRACK`, which can be used in `MAD-X-PTC` in order to match the optical functions.
The quadrupole strengths matched in `MAD-X-PTC` are then used in `FTRACK` for de-
termining the dynamic aperture, momentum acceptance etc. with the more detailed
information from the actual field map. Comparing the matrix based matched tunes
from `MAD-X-PTC` with field map based tracked tunes in `FTRACK` yields a deviation
in the order of $0.4\,\%$ for the non-integer part of the horizontal tune, and $0.44\,\%$
for the non-integer part of the vertical tune (both on-energy, comp. Tab. 3.4). As
the objective here is to find quadrupole settings for which the β-functions are reas-
onable and the tunes are matched to sufficient precision, the achieved accuracy is
acceptable.

The overall intention of `FTRACK` is to find the dynamic aperture for lattices
containing an arbitrary field map by means of integration. A small deviation from
the matched tunes will not affect the dynamic aperture calculation in a way that
would increase the dynamic aperture.

To benchmark `FTRACK` with `MAD-X-PTC`, calculations for the MLS standard user
operation mode, are compared in the following. For the calculations, the exact
same quadrupole strengths were used. However, as mentioned earlier, there appears
to be a difference in the tracked vertical chromaticities. As a consequence, slightly
different sextupole strengths were used in `FTRACK` in order to keep the chromaticities
close to 0.5 in both transverse planes to stay clear of resonances. The deviation of the
tunes in the order of sub-percentages between the two codes were already mentioned
in the introduction to this section (comp. Tab. 3.3). In Fig. 3.15 the β-functions

Table 3.3: Transverse non-integer parts of the tunes and natural chromaticities for
the standard user operation mode at the MLS tracked with `MAD-X-PTC` and `FTRACK`.
The tunes were calculated from a particle with starting coordinates $x_0 = y_0 = 0.5 \times 10^{-5}\,\mathrm{m}$, $\delta = 0.5 \times 10^{-5}$, and the rest equal to zero. The cavity was turned off
for tracking the chromaticity.

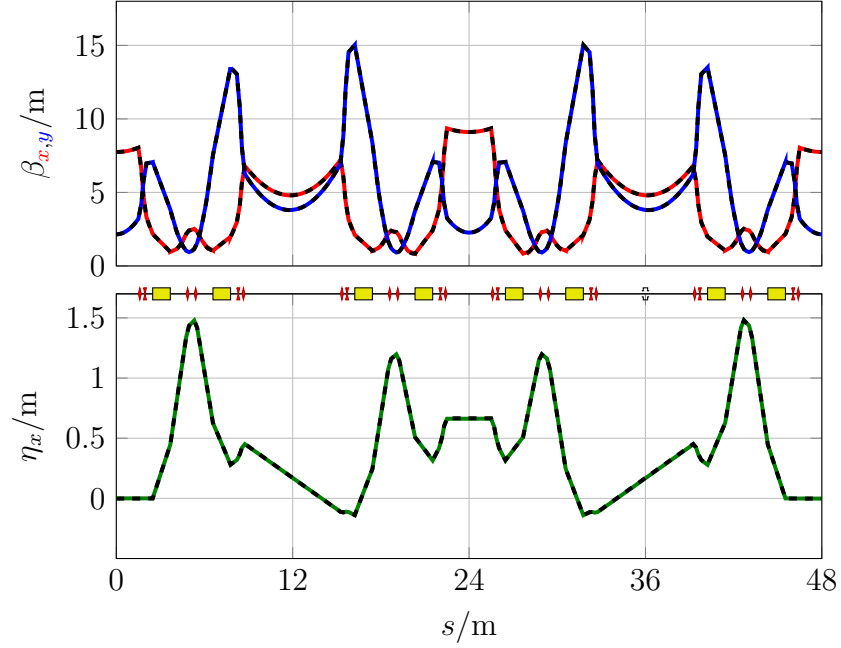|	MAD-X-PTC	FTRACK	$\Delta_{\mathrm{FTRACK,MAD-X-PTC}}$ / %
Q_x	0.178 07	0.178 07	0.00
Q_y	0.232 17	0.231 68	0.02
ξ_x	−3.419 64	−3.484 77	1.90
ξ_y	−6.525 81	−3.993 65	38.80

Figure 3.15: Comparison of the β-functions and dispersion for `MAD-X-PTC` (black, dashed) and `FTRACK` (colour, solid) for the standard user operation mode at the MLS.

and the dispersion are presented for `FTRACK` and `MAD-X-PTC`. As expected from the comparison of the tunes, there are no obvious differences between the optical functions for the two codes.

Differences between `FTRACK` and `MAD-X-PTC` can be observed considering the tune footprint of the tracked particles (comp. Fig. 3.16). Although the chromaticities were corrected, the tuneshift with amplitude is different because of the different sextupole strengths. As a consequence, the area which the particles cover in the tune diagram differs. This does not affect the aperture presented in Fig. 3.17. For the calculations, 6-d particle tracking was performed with the cavity voltage set to $800\,\mathrm{kV}$. The geometrical apertures of the vacuum chamber were also included. Therefore, Fig. 3.17 shows the aperture in general, as it included all three acceptances listed

Table 3.4: Transverse non integer parts of the tunes for the RW lattice calculated with `MAD-X-PTC` and `FTRACK`. The tunes were determined from a particle with starting coordinates $x_0 = y_0 = 1 \times 10^{-5}\,\mathrm{m}$, and all other coordinates equal to zero in `FTRACK`. In `MAD-X-PTC`, the tunes were calculated with `TWISS`.

	`MAD-X-PTC`	`FTRACK`	$\Delta_{\text{FTRACK,MAD-X-PTC}}$ / %
Q_x	0.178 00	0.178 71	0.40
Q_y	0.232 00	0.230 97	0.44
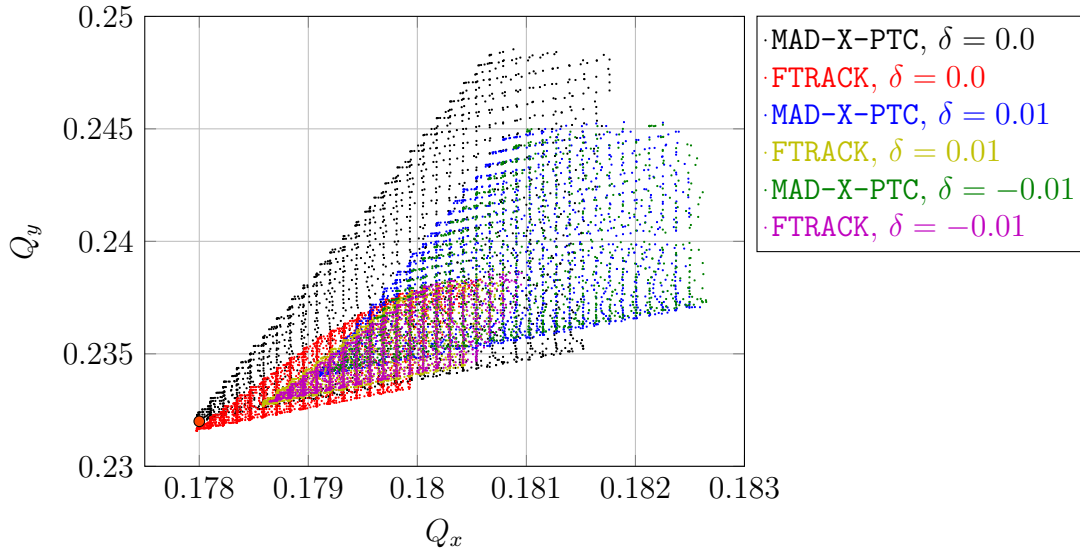
Figure 3.16: Tune footprint for the standard user mode at the MLS. The transverse chromaticities were corrected to 0.5 in both planes for both codes. The orange dot marks the reference tune (0.178/0.232).

in Sec. 2.4.1.

The aperture for the standard user operation mode at the MLS agrees well between `FTRACK` and `MAD-X-PTC` (comp. Fig. 3.17). This circumstance justifies using `FTRACK` to determine the aperture for the MLS including the RW on the premise that the field map integration is working properly.

3.4.2 Dynamic Aperture for the Robinson Wiggler Lattice

As mentioned above, the optical functions and tunes for the RW lattice were matched in `MAD-X-PTC` with 6×6 transfer matrices generated in `FTRACK`. The transfer matrix is not as precise as the actual field map, and as a result, the deviations for the tracked tunes between `FTRACK` and `MAD-X-PTC` increase compared to the standard user mode calculations. Still, the deviations are small as can be seen by comparing the optical functions for the RW lattice shown in Fig. 3.18 and Fig. 3.19. In Tab. 3.4 the matched tunes in `MAD-X-PTC` and corresponding tracked tunes from `FTRACK` are compared. As said, the deviation of 0.4 % in the horizontal plane is larger than for the standard user operation mode calculations. However, the intention of this code is not to have ultimate precision regarding the tunes, but to have reasonable precision for determining the dynamic aperture. All in all, a mismatch of the tunes would, as long as the intended tunes for the machine are chosen wisely, if anything decrease the dynamic aperture. Therefore, the accuracy with which the tunes are
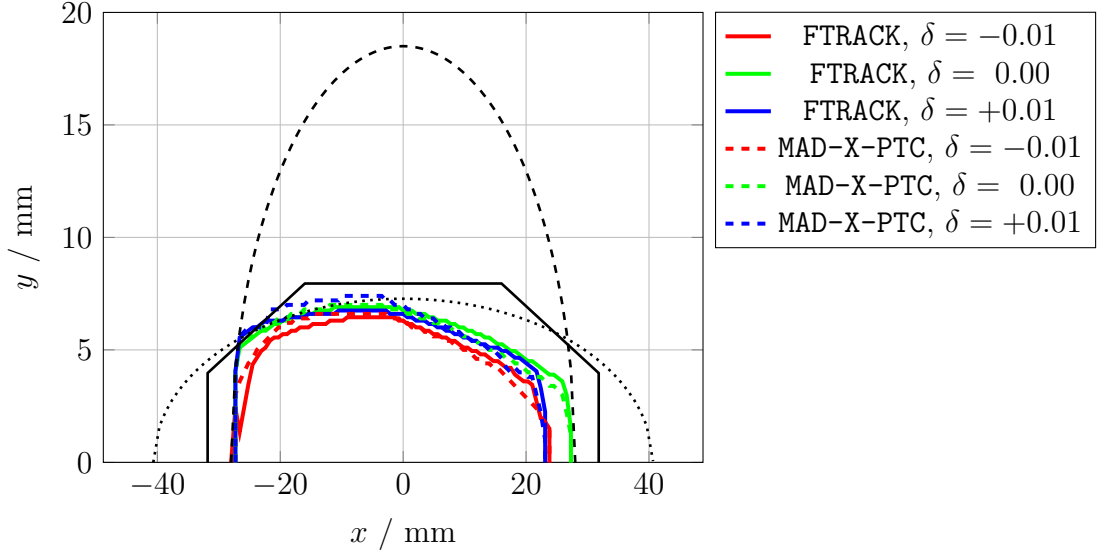
Figure 3.17: Dynamic aperture including geometrical apertures for standard user operation mode at MLS calculated with `MAD-X-PTC` and `FTRACK`. Chromaticities were corrected for `FTRACK` so that in both codes the chromaticities are around 0.5 in both transverse planes. The geometrical apertures (black) were scaled according to the square root of the ratio of the β-functions at the septum to the β-functions at the longitudinal position s_a of the aperture: $a_{x/y,\text{plot}} = a_{x/y}(s_a) \cdot \sqrt{\frac{\beta_{x/y,\text{septum}}}{\beta_{x/y}(s_a)}}$. The geometrical apertures are the septum magnet (dashed), the undulator chamber (dotted), and the remaining vacuum chamber (solid).

translated between the two programs is sufficient.

In Fig. 3.20a the aperture for the RW lattice is presented. The field map used is the one for an "ideal" RW with 12 poles. Like for the standard user operation mode in the previous section, 6-d particle tracking, including cavity (800 kV) and geometrical apertures, was performed. Figure 3.20a also features the aperture for standard user operation mode for comparison. The aperture with RW appears to be smaller than without the RW. The reason for the smaller aperture is, that the results shown in Fig. 3.20a do not take the change in emittance into account that occurs when the RW is in operation. The change in damping partition leads to a decreased emittance of roughly half of the initial value. Therefore, when comparing the two apertures, it is necessary to include the changed emittance. Taking the change in emittance into account, as in Fig. 3.20b, it becomes clear that the aperture would actually increase for on-energy particles, with cuts for off-energy particles. However, the aperture is larger than 20σ in every direction and therefore sufficiently large to stably store the electron beam.

To achieve this, it is essential to find sextupole settings for which the chromaticity
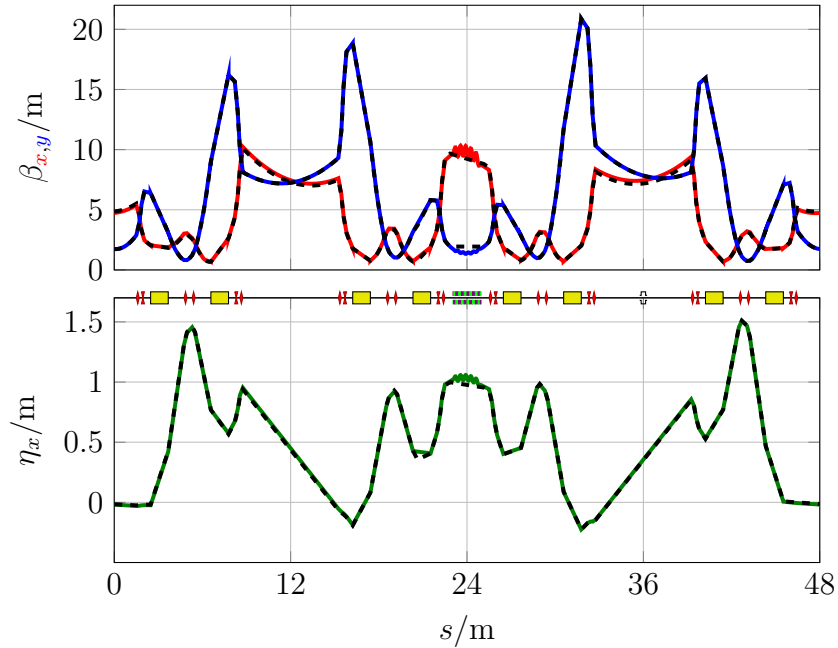
Figure 3.18: Comparison of the β-functions and dispersion for `MAD-X-PTC` (black, dashed) and `FTRACK` (colour, solid) for the RW lattice.

is small and positive, and for which the tuneshift with amplitude is also small. Especially the vertical chromaticity is important as the vertical tune is close to a resonance line at 0.25.

At some point, the value of the dispersion function at the RW also becomes a factor limiting the aperture. But, with a dispersion of 1.1 m at the RW, the aperture is sufficiently large to have stable operation, while maintaining the desired effect on the damping. After all, it is not necessary to inject into a lattice where the RW is fully powered, as the RW can be switched off for injection.

3.4.3 Error Estimations from `FTRACK`

To find the tolerances for field errors for the RW with twelve poles, the procedure as described above was followed. Different error types were applied and for each type the threshold was determined for which stable operation cannot be guaranteed. The latter was done by (a) tracking in phase space, as a first-order-of-magnitude scan, and (b) tracking the dynamic aperture for greater detail. The following error types were applied to the field map:

- **Relative noise**
  Every point on the grid in the x-s-plane or every individual pole gets a random relative error assigned, depending on the initial field at that point; the same
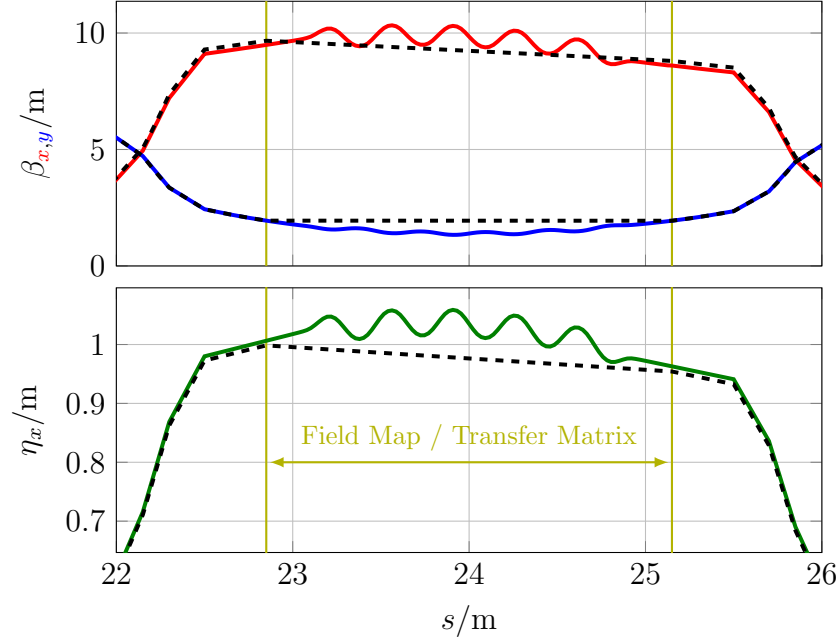
Figure 3.19: Close up of the comparison of the β-functions and dispersion for `MAD-X-PTC` (black, dashed) and `FTRACK` (colour, solid) for the RW simulated as a transfer matrix and as a field map respectively.

relative error is applied to each grid point in the y-direction;

- **Multipole errors**
  Different multipole errors (up to order 10) are applied to each pole or to each horizontal grid line in the x-s-plane; the multipole errors in the y-direction are calculated with reference to the values for the x-s-plane.

As the multipole errors include order 0, the tolerance for allowed deviations from design B_0 between the individual poles can be determined. In principle, errors in B_0 can be easily corrected with the correction coil, which is simulated in `FTRACK` with the additional dipole field that can be applied to make the field map as transparent as possible. What the additional dipole field is not able to correct to full extent are the higher order multipole errors.

In Tab. 3.5 the determined thresholds for the different error types are presented. The thresholds were determined for a field map with a step width of $5\,\mathrm{mm}$ in the longitudinal plane, and $1\,\mathrm{mm}$ in the horizontal and vertical plane. Figure 3.21 shows the resulting aperture when all the errors are applied with the values of the respective thresholds.

The aperture for the RW with the determined thresholds for the errors would still be sufficiently large, as it is still larger than 20σ in both transverse planes.

(a)

(b)
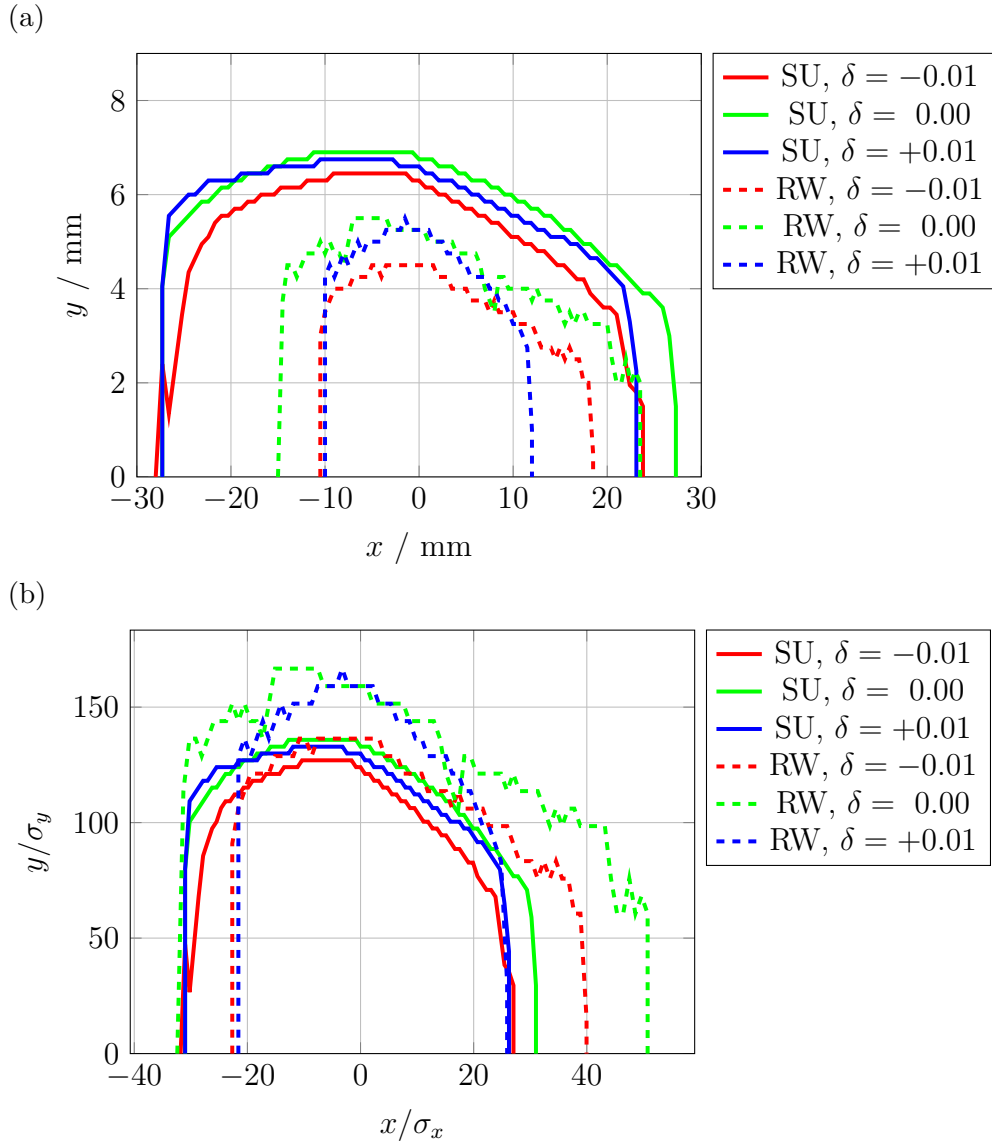
Figure 3.20:   Dynamic aperture for the RW lattice calculated with `FTRACK`, $\eta_x = 1.1\,\mathrm{m}$ at the RW. The transverse chromaticities were corrected to be below 1.0 and of positive sign in both transverse planes. The optical functions were optimized to be below $20\,\mathrm{m}$. The apertures take the change in beam size into account for (b), whereas (a) shows the apertures in length units.

Apart from minor deviations in the vertical plane, the apertures for a RW with and without errors are essentially similar.

However, in contrast to the standard user operation mode without RW, especially in the horizontal plane, the dynamic aperture becomes more important and might become limiting as it cuts into the apertures given by the geometry of the vacuum chamber (comp. Fig. 2.9, 3.17 and 3.21). In that sense, the MLS with RW makes more use of its potential regarding the dynamic aperture. Without RW, the dynamic
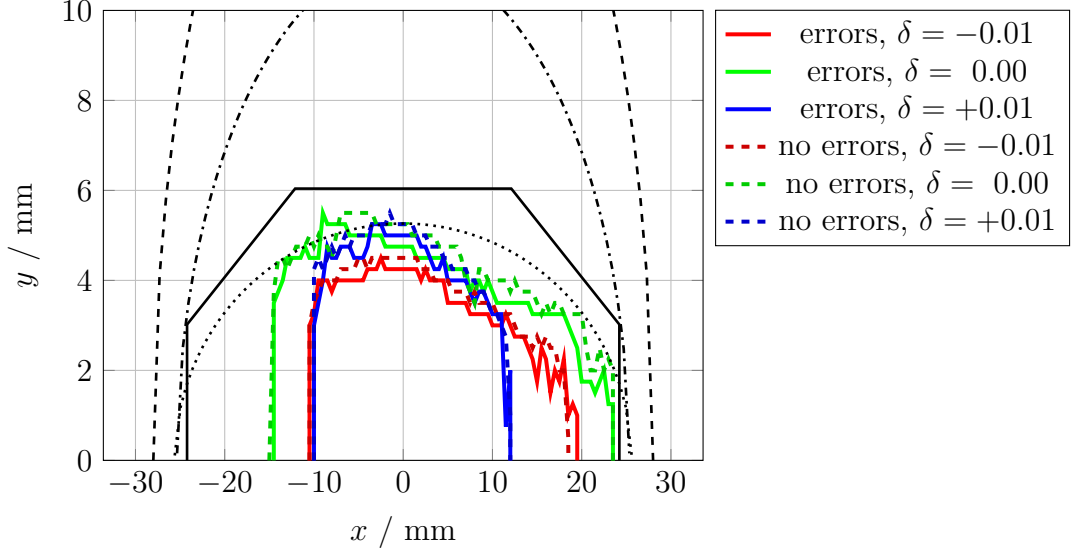
Figure 3.21: Comparison of the dynamic apertures for the MLS with RW, with and without errors. The geometrical apertures (black) are the septum magnet (dashed), the undulator chamber (dotted), the remaining vacuum chamber (solid), and the RW vacuum chamber (dash dotted).

aperture is larger than the geometrical aperture (Fig. 2.9). This potential is used

Table 3.5: Thresholds for the different error types. For the multipole orders 0 and 1, which are the "design" orders for dipole and quadrupole field, the thresholds are the allowed relative deviations from the design values. For the higher order multipoles, the thresholds are the upper absolutes of the multipole coefficients (Eq. 3.6). The thresholds were determined via dynamic aperture tracking with FTRACK.

	each point / hor. grid line	polewise
relative noise	1.0×10^{-4}	3.0×10^{-3}
multipole order 0	1.0×10^{-2}	4.0×10^{-3}
multipole order 1	7.0×10^{-3}	8.0×10^{-3}
		$|\partial^n B_y / \partial x^n|$
multipole order 2		2.0×10^{1}
multipole order 3		4.2×10^{3}
multipole order 4		2.2×10^{5}
multipole order 5		1.2×10^{8}
multipole order 6		1.4×10^{10}
multipole order 7		3.5×10^{12}
multipole order 8		8.0×10^{14}
multipole order 9		7.3×10^{16}
multipole order 10		2.5×10^{19}

when operating the RW. Regarding operation and lifetime, the resulting aperture is sufficiently large.

3.5 Radiation Characteristics

In order to study the radiation characteristics of the RW, as well as the new RW optics' influence on the undulator performance, the program `WAVE` was used. `WAVE`, developed by Dr. Michael Scheer at HZB, offers the calculation of spontaneous synchrotron radiation for arbitrary magnetic fields (Scheer, 2012). As an input, an electron bunch with initial coordinates according to energy spread, emittance, and dispersion and β-functions at the entrance of the wiggler, can be provided. Individual particles are tracked and the produced radiation is folded taking coherence effects into account.

At the end of the short straight section, opposite of the septum magnet, exists a radiation port which enables the extraction of the radiation produced by the RW. Therefore, the RW may be used as an additional radiation source. The acceptance of this port is ± 7.7 mrad in the horizontal plane and ± 4.3 mrad in the vertical plane, which is comparable to that of the EUV-dipole beamline at the MLS.

As derived in Eq. 3.8, the deflection parameter of the twelve poled RW is $K_{\mathrm{RW}} = 32.508$. Therefore, a wiggler spectrum is expected. From the undulator equation

$$\lambda_n = \frac{\lambda_{\mathrm{RW}}}{2n\gamma^2} \left(1 + \frac{K_{\mathrm{RW}}^2}{2} + \theta^2 \gamma^2 \right), \tag{3.11}$$

it is possible to calculate the first undulator harmonic for the twelve poled RW. For $\theta = 0$, i.e. on-axis, the first undulator harmonic for the twelve poled RW is expected at $\lambda_{1,\mathrm{RW}} = 61.76\,\mu\mathrm{m}$, or $E_{1,\mathrm{RW}} = 2.01 \times 10^{-2}\,\mathrm{eV}$. In Fig. 3.22a, the spectrum generated by the twelve poled RW is presented together with the spectra of the EUV and the IR beamline dipoles (with the respective acceptances). The wiggler spectrum, depicted in shades of blue, was determined in two different ways:

1. the RW as a wiggler: each individual radiation source (i.e. the poles) are treated completely incoherently (light blue in Fig. 3.22a),

2. the RW as an undulator: interference effects are included, giving rise to undulator harmonics (deep blue in Fig. 3.22a).

The RW spectra agree well for photon energies above $\sim 1 \times 10^{-1}\,\mathrm{eV}$ and show the characteristics of a wiggler spectrum. The expected position for the first undulator harmonic is slightly off. As the on-axis field of the RW is comparable to that of the dipoles at the MLS, it is expected that the spectrum shows more or less twelve times
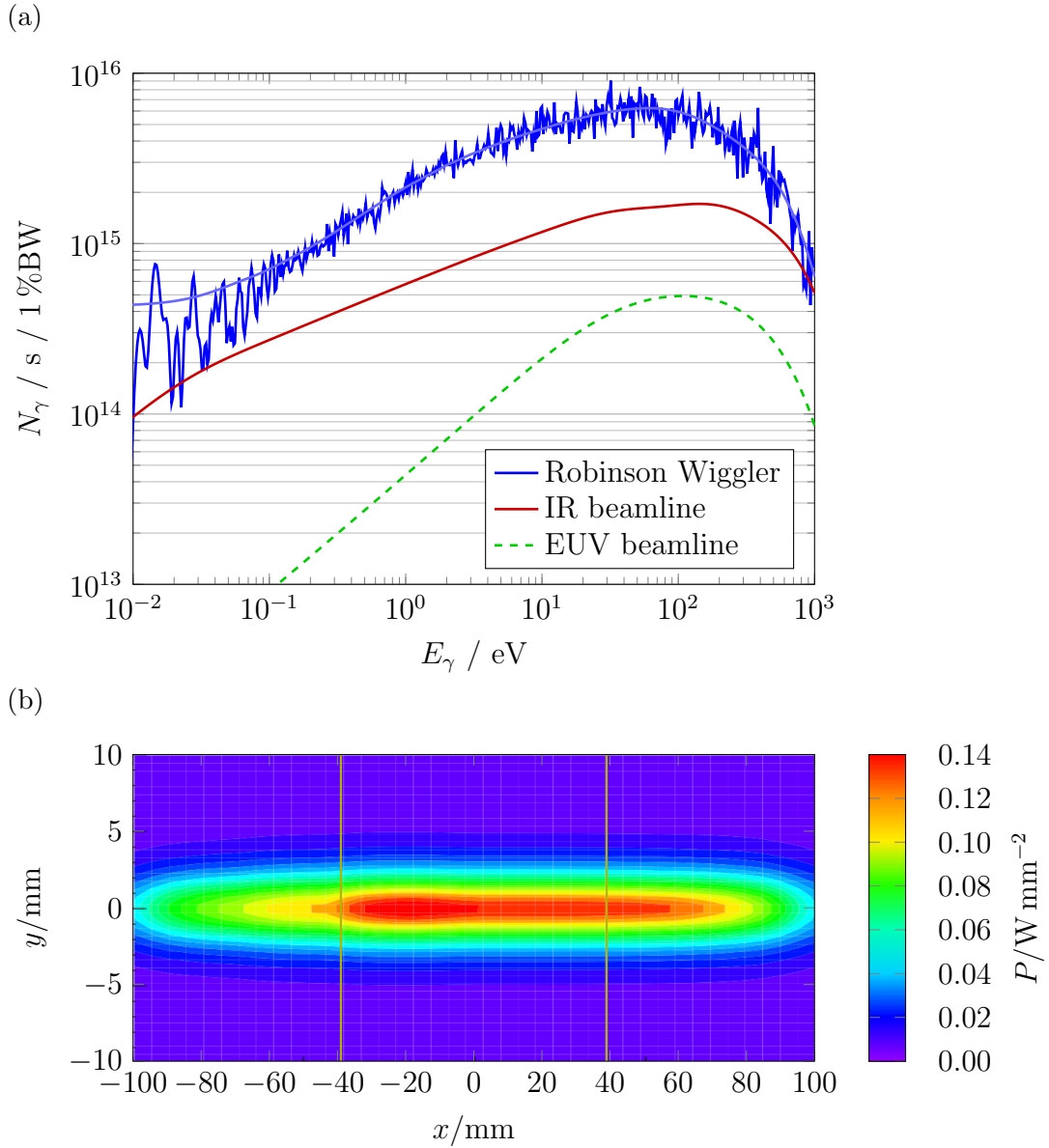
(a)

(b)

Figure 3.22: Photon spectrum for the twelve poled RW together with the spectra for the IR and the EUV beamlines (a). All calculations were done with the existing apertures at the respective beamlines. Power distribution in pinhole at distance 3.665 m from RW straight centre (b). The pinhole acceptance is indicated in yellow in the horizontal plane.

the number of photons (because of twelve poles) as for the EUV-dipole beamline (as the acceptance for the two is more or less the same). Comparing the spectra of the EUV-beamline and the RW in Fig. 3.22a, confirms this.

The total power radiated by the device is 105.59 W of which 52.20 W are distributed inside the acceptance of the pinhole. In Fig. 3.22b, the power distribution of the radiation from an aligned bunch is presented together with an indication of the

(a)

(b)
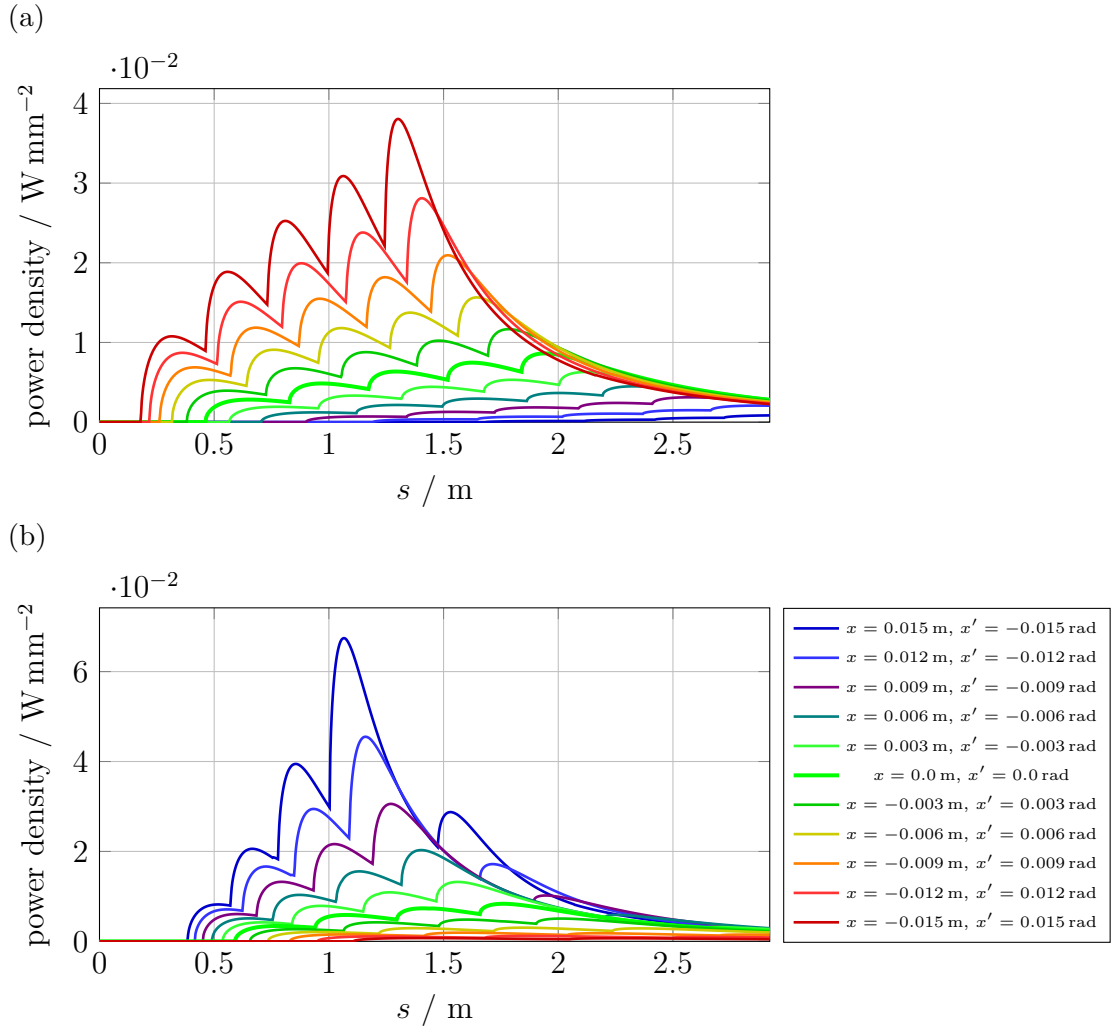
Figure 3.23: Longitudinal power distribution on the inside of the vacuum chamber due to the radiation of the RW. The longitudinal position is measured from the center of the short straight section in K3 (= center of the RW). The power distribution was calculated for different offsets and angles of the particles on the vacuum chamber wall at $x = 35\,\text{mm}$ (a) and on the vacuum chamber wall at $x = -35\,\text{mm}$ (b).

acceptance of the pinhole. The remainder of the produced radiation may hit the vacuum chamber and cause heating which might not be cooled away by the existing cooling system. In order to study these effects, the power distribution on the vacuum chamber walls for different beam angles was determined (compare Fig. 3.23). The power distributions were then used to calculate the heat flow in the downstream objects (Dirsat et al., 2014-2016). The result of these studies is that none of the downstream objects will be endangered by the additional radiation of the device.
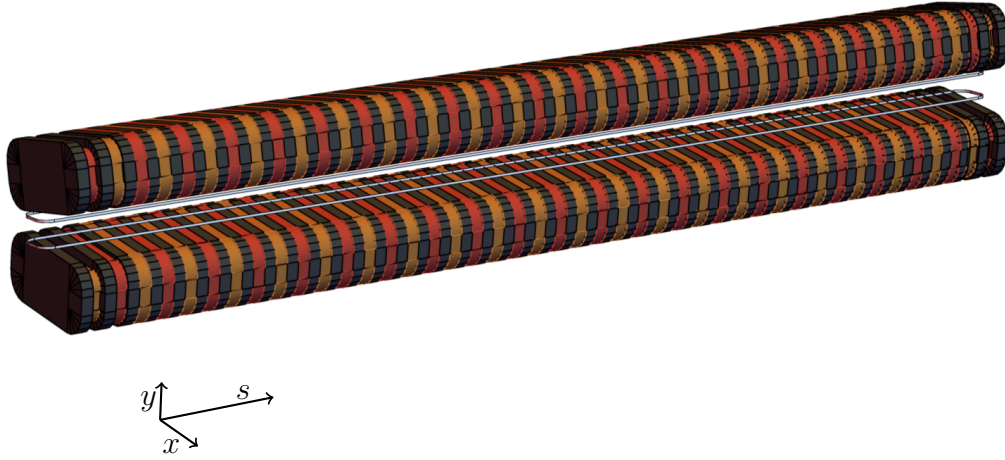
Figure 3.24: Superconducting RW design consisting of racetrack coils (red and orange) wound around a magnetization free yoke (black, e.g. made of copper).

3.6 Superconducting Design

Super conductivity offers high fields in rather small structures. A superconducting design enables short period lengths and therefore a smaller impact on the accelerator optics while preserving the ability to alter D.

Two superconducting design studies were conducted. The first design, consisting of a set of Helmholtz coils, was oriented at a design given by (Rodríguez et al., 2013), yielding high gradients in the order of $100 \, \mathrm{T \, m^{-1}}$. A second design using racetrack coils yields a smaller gradient but with a wider horizontal range of linear field gradient. The second design is depicted in Fig. 3.24, in the following called "racetrack design". It consists of several superconducting racetrack coils, wound around a magnetization free yoke. This design yields an on-axis field of $B_y = 1.387 \, \mathrm{T}$ with a gradient of $14.78 \, \mathrm{T \, m^{-1}}$. The integrated product is high enough so that a dispersion of $\eta_x = 1.0 \, \mathrm{m}$ would be sufficient to reach $D = -1.75$. The focussing is affected as expected from the increased number of poles: R_{21} is equal to -0.012, for which the absolute value is an order of magnitude smaller than for any of the presented normal conducting design solutions. The vertical focussing stays comparable with $R_{43} = -0.327$.

The decreased impact on the optics can be seen in Fig. 3.25, where the β-functions and the dispersion are displayed for a lattice including the superconducting RW. The oscillations of the β-functions and the dispersion inside the wiggler are only visible when zooming in.

Due to the short period length of $80 \, \mathrm{mm}$, the horizontal oscillation amplitude
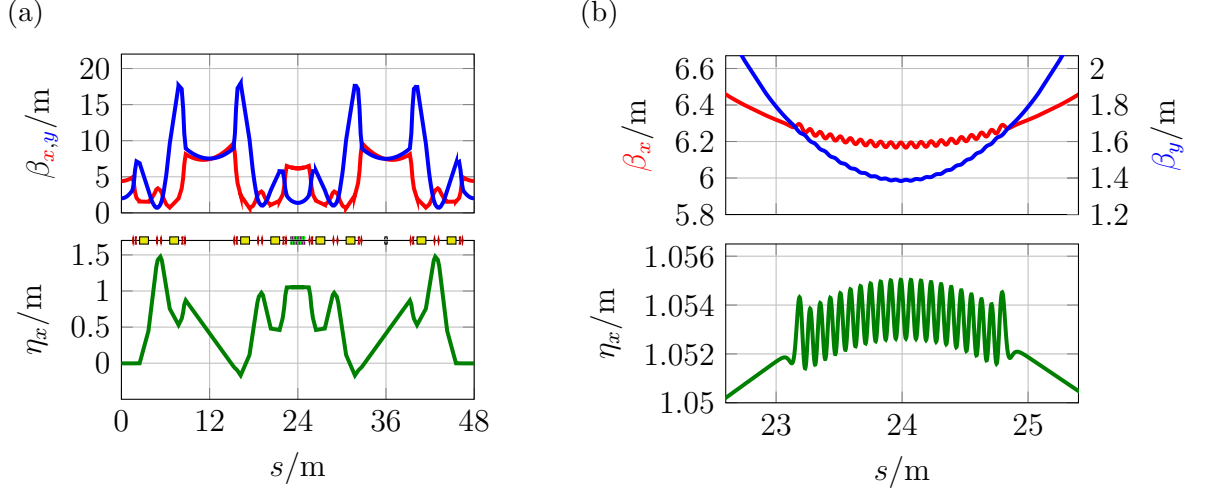
Figure 3.25: Optical functions for the MLS with a superconducting RW of the racetrack design. The complete ring is shown in (a) while (b) depicts the optical functions inside the wiggler as a close up.

is in the order of $100\,\mu m$. The normal conducting devices introduce oscillation amplitudes in the order of several milli meters. Due to the higher number of poles, also the ponderomotive drift is smaller compared to the normal conducting RW's. Therefore, a smaller current in the correction coil is needed to make the device transparent. The chromatic effects of the device are also small compared to the normal conducting solutions: the chromaticities, without excited sextupoles, with the superconducting device are $\xi_x = -3.4536$ and $\xi_y = -5.2044$, corresponding to $\Delta\xi_x = 0.0312$ and $\Delta\xi_y = -1.2107$. In the horizontal plane the chromaticity is essentially the same as for the standard user operation mode without the RW, while in the vertical plane the chromaticity is slightly lower as for all normal conducting RW's.

The overall length was again set to $1900\,mm$, being the available space in the short straight section opposite of the septum magnet. Together with the period length and the on-axis field, the deflection parameter K is calculated to be

$$K_{\mathrm{SCRW}} = 10.346.$$

With a K in the order of 10 it depends on the definition whether to speak of an undulator or a wiggler, some would even call it a "wundulator" (Clarke, 2004), as for longer wavelengths an undulator like behaviour with interference effects occurs, whereas for short wavelengths the radiation of the device shows no interference
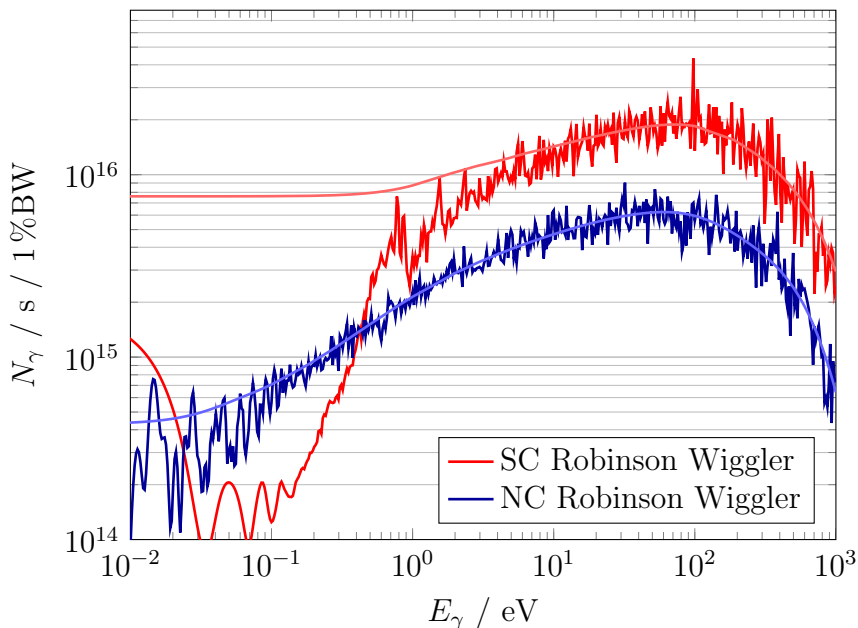
Figure 3.26: Photon spectrum for the superconducting RW together with the spectrum for a normal conducting twelve poled RW. All calculations were done with the existing apertures at the respective beamlines.

effects and is therefore more wiggler like.

Applying Eq. 3.11 on the superconducting design yields the wavelength for the first undulator harmonic $\lambda_{1,\text{SCRW}} = 1.44\,\mu\text{m}$, or in terms of energy: $E_{1,\text{SCRW}} = 0.8615\,\text{eV}$

In Fig. 3.26, the calculated spectra for the superconducting and the normal conducting RW are presented. The normal conducting spectrum is better described by the pure wiggler spectrum than the superconducting one, which can be understood by comparing the deflection parameters. The deflection parameter for the superconducting device is closer to one than the deflection parameter for the normal conducting device. Therefore, the spectrum for the normal conducting device should be closer to a pure wiggler spectrum than the spectrum of the superconducting device. Where the spectra of the normal conducting device agree well for photon energies higher than $\sim 0.1\,\text{eV}$, the spectra for the superconducting device agree for photon energies higher than $\sim 10\,\text{eV}$.

Comparing the peak value for the wiggler spectra at $\sim 100\,\text{eV}$, the superconducting device yields ~ 5.5 times more photons than the normal conducting device. The number of poles for the superconducting device is 43, which is 3.6 times higher than the twelve poled normal conducting device. The on-axis B_y is 1.4 times higher, and together that makes an estimated increase in flux by a factor of 5.04, which agrees well with the simulations.

(a)

(b)
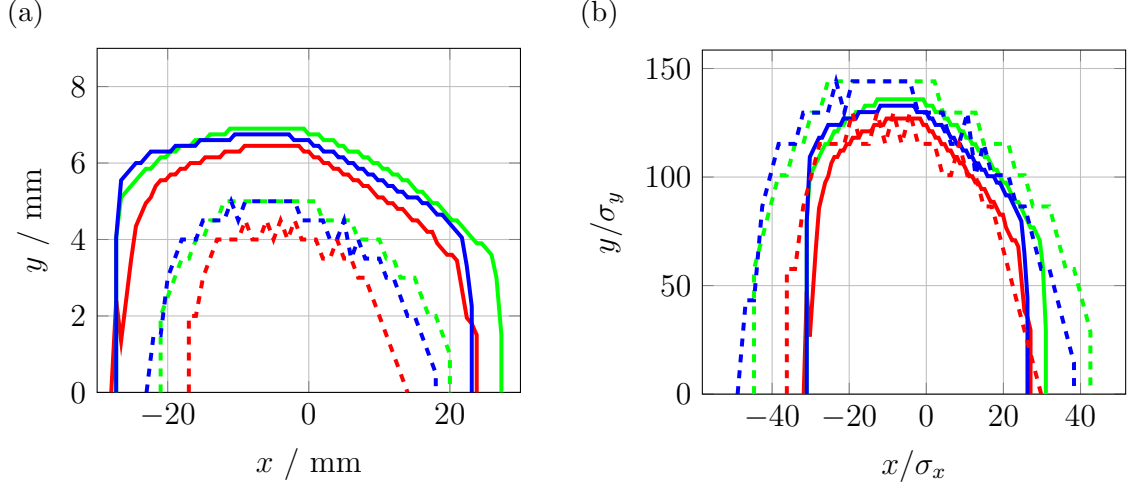
Figure 3.27: Dynamic aperture for the MLS with a superconducting RW compared to standard user mode. In (a) the dynamic aperture is depicted in units of length, in (b) in units of beam size. The solid lines represent the standard user mode, the dashed lines the RW lattice. Green stands for on-energy particles, whereas blue indicates an initial energy offset of 1%, and red indicates an initial energy offset of -1%.

The power radiated by the superconducting RW is $159.64\,\mathrm{W}$, which is 51.2% higher than for the normal conducting version, and due to the higher on-axis B_y.

The dynamic aperture for the MLS with a superconducting RW would increase slightly due to the shrinking beam size (compare Fig. 3.27). But as expected by the focussing characteristics, there is no major impact of the superconducting RW.

The superconducting alternative seems very attractive regarding dynamic aperture, additional focussing, and radiation characteristics. In all these fields it is superior to the normal conducting design. However, concerning reliability, a superconducting solution might be inferior compared to normal conducting solutions which do not quench or are dependent on helium supply. Furthermore, the normal conducting solutions use well known technology and are realizable on shorter time scales than the superconducting solution with the present resources at HZB. Therefore, a normal conducting design seems preferable in the case of the MLS. Nevertheless, the superconducting design could be the next step as it features many advantages over the normal conducting design.

Expected Effects on Operation

4.1 Beam Lifetime

In the previous chapter, the design of a twelve poled normal conducting RW was derived. The ability of the RW to alter the damping partition depends on the current density in the coils. For a current density of $7.1\,\mathrm{A\,mm^{-2}}$, D may be altered to $D_f = -1.49 \cdot \langle \eta_x \rangle_{\mathrm{RW}}\,\mathrm{m^{-1}} + D_i$, depending on the dispersion set up at the RW.

With changing the damping partition, the equilibrium emittance and the energy spread are altered. In Fig. 4.1, the evolution of the emittance and the energy spread as a function of the dispersion set up at the RW is presented for different excitation current densities. The emittance and the energy spread, determined with `FTRACK` according to (Helm et al., 1973), are normalized to their initial values for the standard user operation mode of $\varepsilon_{x,0} = 117.37\,\mathrm{nm\,rad}$ and $\sigma_{\delta,0} = 4.42 \times 10^{-4}$.

The emittance depends not only on the damping partition, but also on I_5. Therefore, varying the dispersion at the RW has an effect on the emittance apart from the damping effect. This is the reason why the emittance for high values of the dispersion at the RW increases again. The effect is stronger for small excitation currents than for high excitation currents. In Fig. 4.2a and Fig. 4.2b, the fifth synchrotron radiation integral I_5 and the damping partition respectively are plotted as a function of the dispersion set up at the RW for different excitation current densities. Looking at Fig. 4.2b, it is possible to reach the longitudinally antidamped regime with damping partitions below -2 with the twelve poled RW.

From the evolution of the emittance and the energy spread, together with the matched optical functions, the lifetime for each step of the set up dispersion can be calculated. In Fig. 4.3, the evolution of the lifetime for different excitation current densities as a function of the dispersion at the RW is presented. The gas lifetime,
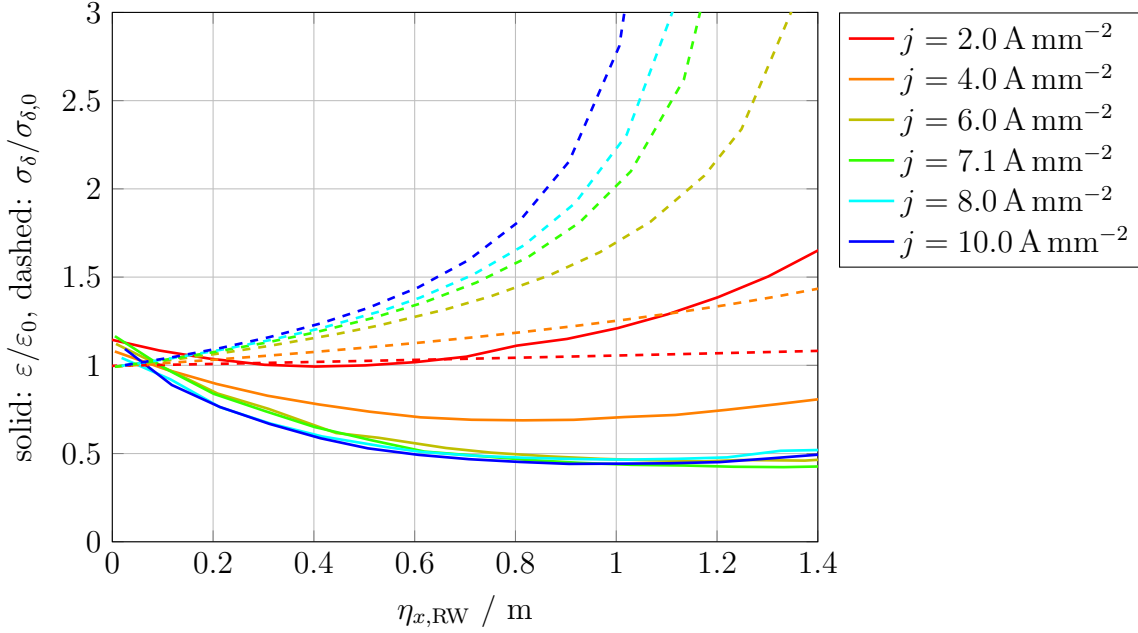
Figure 4.1: Emittance ε (solid) and energy spread σ_δ (dashed) normalized to the standard user operation values ε_0 and $\sigma_{\delta,0}$ as a function of the dispersion set up at the RW. Emittance and energy spread were calculated with `FTRACK`. The optical functions for each step (0.1 m steps for the dispersion at the RW) were matched with `MAD-X`.

determined in (Goetsch, 2013), was assumed to be constant at $\tau_{\text{gas}} = 24.5\,\text{h}$ for the calculations. The acceptance was assumed to be constant at $\delta_{acc} = 1.15\,\%$ (comp. geometrical acceptance in Sec. 2.4.1) and the cavity voltage was set to $500\,\text{kV}$.

The emittance coupling was adjusted in a way that the lifetime for $150\,\text{mA}$ in standard user operation mode meets the measured lifetime of $6.0\,\text{h}$. A coupling parameter of $\kappa_{\text{wn}} = 0.022$ proofed to result in a matching lifetime. This value for the coupling is higher than the measured emittance coupling without white noise excitation[1] of $\kappa_{\text{nwn}} = 0.005$ for the standard user operation mode. But as during the standard user mode operation the beam is vertically excited with white noise excitation, it is necessary to calculate the lifetime with an increased coupling. For the calculations of the lifetime with RW, the vertical beam size was assumed to stay constant (apart from variations of the vertical β-function) as for the standard user operation mode because the white noise excitation will still be applied when the wiggler is in operation. Therefore, the vertical beam size for all calculations was set

---

[1]comp. Sec. 1.2

(a)

(b)
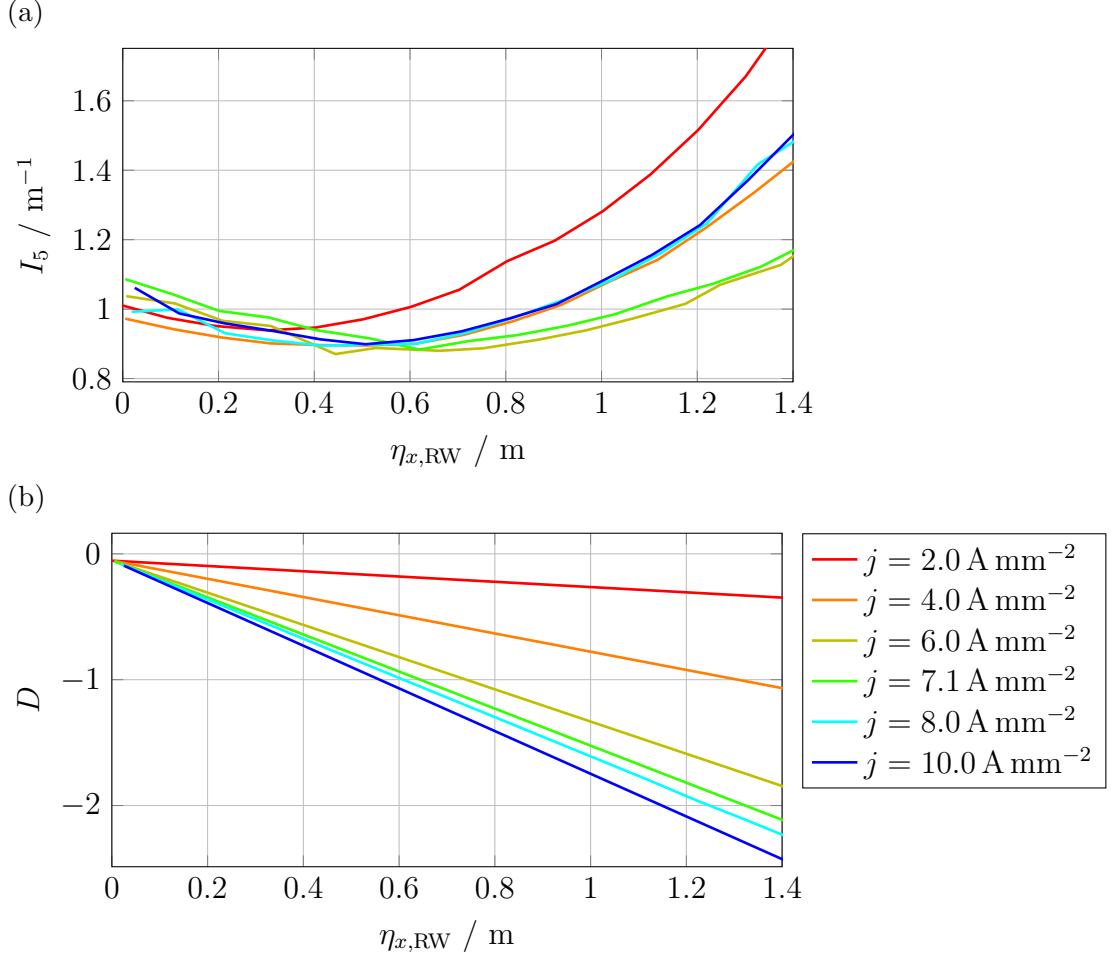
Figure 4.2: The evolution of I_5 (a) and the damping partition D (b) as a function of the dispersion at the RW for different excitation current densities j.

to

$$\sigma_y(s) = \sqrt{\varepsilon_{x,0} \cdot \kappa_{\text{wn}} \cdot \beta_y} \approx \sqrt{117.37\,\text{nm rad} \cdot 0.022 \cdot \beta_y} = \sqrt{2.58\,\text{nm rad} \cdot \beta_y}.$$

All calculations were performed assuming a stored current of $150\,\text{mA}$. In Sec. A.2, the `Python` script used for calculating the lifetime is given.

The predicted lifetime in Fig. 4.3 shows that the twelve poled normal conducting RW is able to increase the beam lifetime at the MLS by a factor of 2.6. Further increasing this factor is not possible because of the longitudinal quantum lifetime which decreases the total lifetime dramatically for damping partitions smaller than -1.895. This effect can be seen in Fig. 4.3 for the current densities above $6.0\,\text{A mm}^{-2}$. Nevertheless, it is possible to operate the MLS with a total lifetime of above $14\,\text{h}$ at $150\,\text{mA}$ instead of $6\,\text{h}$ at $150\,\text{mA}$. This corresponds to increasing
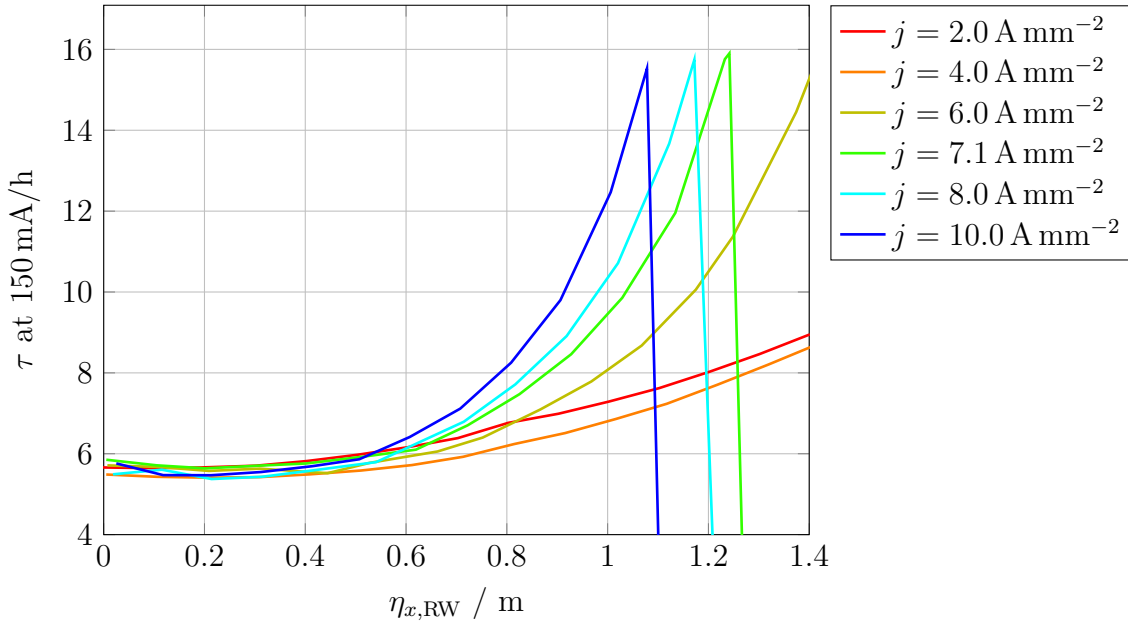
Figure 4.3: Predicted lifetime as a function of the dispersion at the RW for different excitation currents and a beam current of 150 mA.

current times lifetime for a standard user operation run from 900 mA h to above 2100 mA h.

The integrated stored beam current in a standard user run, starting at 200 mA and decaying in a time interval of 6 h, increases from 749.1 mA h to 958.4 mA h, corresponding to an increase in photon flux of 27.9 %. After a standard user run of six hours, the remaining stored beam current increases from 80 mA to 127 mA. Furthermore, it is possible to extend the duration of a standard user run from 6 h to 12 h with a remaining beam current after twelve hours of 87 mA, which is higher than 80 mA after six hours in the current standard user operation mode.

Such an increase in lifetime is a benefit for the user community of the MLS as the temporal stability of the emitted synchrotron radiation is further improved and the integrated photon flux increased.

4.2 Dipole Beamlines Performance

The MLS serves eight beamlines, of which seven use bending magnet radiation. The optical functions for the MLS including a normal conducting twelve poled RW, are depicted in Fig. 3.13. The changes regarding the optical functions are of minor nature compared to the expected change in emittance and energy spread.

Assuming a current density of $7.1\,\mathrm{A\,mm^{-2}}$ in the coils, and a value of the dispersion function at the RW of $1.1\,\mathrm{m}$, the emittance reduces in theory from $117.37\,\mathrm{nm\,rad}$ to $50.74\,\mathrm{nm\,rad}$, whereas the energy spread increases from 4.42×10^{-4} to 1.16×10^{-3}. Together with Eq. 2.18 and 2.21, the source sizes and divergences before and after the installation of the RW can be calculated.

In Tab. 4.1, the source sizes for the different beamlines with and without RW are listed. These calculations do not include white noise excitation used at the MLS to compensate ion effects and which keeps the vertical source size constant. Therefore, the vertical source sizes listed in Tab. 4.1 can be understood as possible lower limits for the vertical source size that can be reached if the MLS is operated without white noise excitation and at low currents with few bunches to reduce ion effects.

The standard user at the MLS is mainly concerned about the vertical source size, its divergence, and how constant the two are. Assuming no white noise excitation and no ion effects, the vertical source size is smaller with lower divergence for every beamline. With white noise excitation, the vertical source size stays more or less the same as before. It is not harmful that the horizontal source size increases for the EUV, VUV, and THz beamlines, as the respective divergences all reduce so that the brilliance stays more or less constant (comp. Tab. 4.2). However, the one insertion device used at the MLS, namely the U125, will be affected by an increase in source size of $7.1\,\%$ combined with an increase in divergence of $31.5\,\%$. Because of this and because of effects of the increased energy spread on the width of undulator harmonics, it is important to study the effects on the U125 performance in detail in the following section.

Table 4.1: Source size and divergence for the different beamlines at the MLS, (a) before and (b) after a possible installation of the RW. Calculations performed in `MAD-X` for standard user mode and RW mode.

(a) $\varepsilon_x = 117.37\,\text{nm rad}$, $\sigma_\delta = 4.42 \times 10^{-4}$, $\kappa = 0.5\,\%$

Beam-line	β_x /m	β_y /m	η_x /m	η'_x	γ_x /m^{-1}	γ_y /m^{-1}	σ_x /µm	σ'_x /µrad	σ_y /µm	σ'_y /µrad
IDB	4.73	3.91	0.20	−0.10	0.21	0.26	750.32	163.1	47.90	12.35
QPD01	1.81	13.29	−0.16	0.10	0.70	0.78	466.31	290.02	88.31	21.39
QNIM	1.50	11.53	−0.10	0.32	0.83	0.78	421.91	342.67	82.26	21.39
EUV	1.10	4.41	0.41	−0.28	1.19	0.57	402.43	393.68	50.87	18.29
VUV	1.49	5.2	0.35	−0.13	0.57	0.35	445.88	264.96	55.24	14.33
THz	1.95	6.09	0.34	−0.02	0.83	0.57	501.45	312.24	59.78	18.29
IR	1.22	9.91	0.03	−0.52	0.95	0.78	378.64	405.37	76.26	21.39
QPD00	1.50	11.53	−0.10	−0.32	0.83	0.78	421.91	342.67	82.26	21.39

(b) $\varepsilon_x = 50.74\,\text{nm rad}$, $\sigma_\delta = 1.16 \times 10^{-3}$, $\kappa = 0.5\,\%$

Beam-line	β_x /m	β_y /m	η_x /m	η'_x	γ_x /m^{-1}	γ_y /m^{-1}	σ_x /µm	σ'_x /µrad	σ_y /µm	σ'_y /µrad
IDB	7.11	6.64	0.46	−0.17	0.14	0.15	803.42	214.46	41.04	6.17
QPD01	1.40	16.46	−0.25	0.00	1.04	0.85	393.87	229.72	64.62	14.68
QNIM	1.04	14.37	−0.21	0.23	1.19	0.85	334.83	362.72	60.38	14.68
EUV	0.80	3.68	0.38	−0.14	1.34	0.49	484.66	307.19	30.56	11.15
VUV	1.05	4.26	0.36	0.01	1.24	0.49	477.14	251.10	32.87	11.15
THz	1.46	4.60	0.38	−0.14	0.98	0.51	518.06	275.86	34.16	11.37
IR	0.84	13.43	−0.11	−0.47	1.32	0.92	242.7	603.51	58.37	15.28
QPD00	1.13	15.54	−0.22	−0.25	1.20	0.92	349.95	380.77	62.79	15.28
RW	9.77	1.39	1.13	−0.18	0.54	0.76	1487.93	266.45	18.78	13.89

Table 4.2: Relative changes in horizontal source size and divergence for the MLS with RW and without RW as in Tab. 4.1.

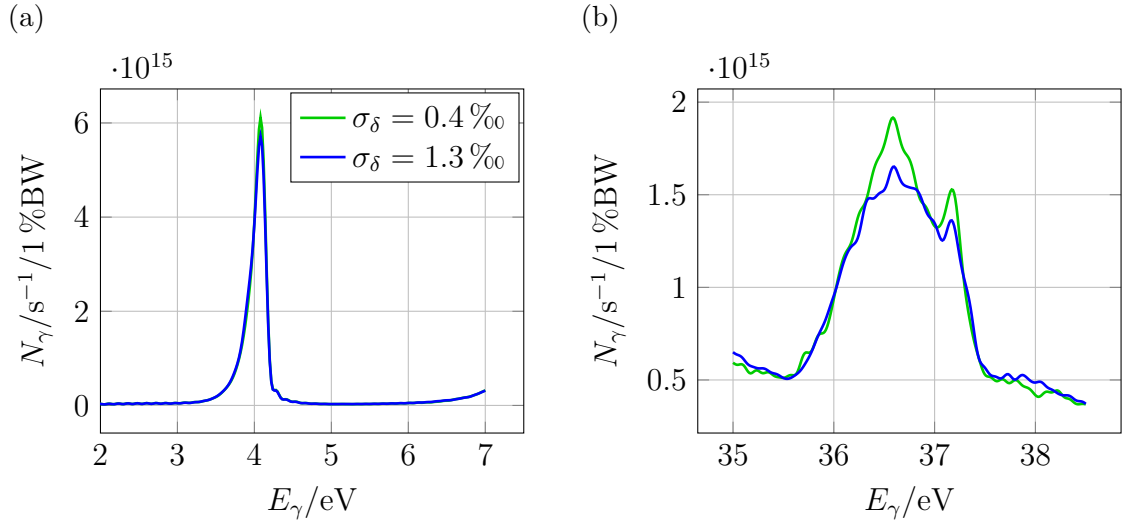| Beamline	$\Delta\sigma_x/\%$	$\Delta\sigma'_x/\%$	$\Delta\sigma_y/\%$	$\Delta\sigma'_y/\%$
IDB	7.08	31.49	−14.32	−50.04
QPD01	−15.53	−20.79	−26.83	−31.37
QNIM	−20.64	5.85	−26.60	−31.37
EUV	20.43	−21.97	−39.93	−39.04
VUV	7.01	−5.23	−40.50	−22.19
THz	3.31	−11.65	−42.86	−37.83
IR	−35.90	48.88	−23.46	−28.56
QPD00	−17.06	11.12	−23.67	−28.56

(a)

(b)

Figure 4.4: Undulator harmonics for the U125 of MLS for energy spreads with (blue, $\sigma_\delta = 1.3 \times 10^{-3}$) and without (green, $\sigma_\delta = 4.4 \times 10^{-4}$) RW. The spectra were calculated with `WAVE` using measured field maps for a gap of 60 mm and 200 mA ring current. In (a), the first undulator harmonic is presented. In (b) the ninth undulator harmonic is displayed, being used by the most demanding undulator radiation user.

4.3 Undulator Beamline Performance

The performance of the U125 is affected by installing the RW. As presented in Tab. 4.1, the horizontal source size increases by 7.1 % combined with an increase in divergence of 31.5 %. It depends on the specific experiment the users at the ID-beamline want to conduct whether this increase is harmful or not. If it is, the RW has to be turned off for that specific experiment.

Furthermore, increasing the energy spread generally impacts the width of the undulator harmonics. To study how much the undulator harmonics are affected by installing the RW, the program `WAVE` was used. In Fig. 4.4, the first and ninth undulator harmonic of U125 are presented for the MLS with and without RW, corresponding to an energy spread of 1.3×10^{-3} and 4.4×10^{-4} respectively. The change in optical functions was taken into account for the simulations. The most demanding ID beamline user conducts experiments using the ninth harmonic. As can be seen in Fig. 4.4b, the effect of the RW on the width of the harmonic is small compared to the increase in photon flux resulting from the lifetime improvement.

4.4 Low-α Operation Mode

The low-α operation mode is used to generate short electron bunches. The emitted radiation of short pulses becomes coherent for wavelengths longer than the bunch length, usually up to the THz regime (Ries, 2014). The bunches are made short by reducing the momentum compaction factor α. The integrated dispersion function has to be close to zero (comp. Fig. 1.3b), so that the momentum compaction factor α becomes small and the electron bunches get shortened as in Eq. 2.62:

$$\sigma_s \propto \frac{\alpha}{f_s} \cdot \sigma_\delta \propto \sqrt{\alpha} \cdot \sigma_\delta.$$

The RW enables to alter the damping distribution. With a negative dispersion at the RW, like it is in the low α operation mode at the MLS, the energy spread may be reduced resulting in a shortened bunch length. Assuming the optical function in the low-α operation mode do not change with operating the RW, the dispersion at the RW is $\eta_{x,\mathrm{RW}} = -0.55\,\mathrm{m}$. Therefore, the damping partition can be altered to $D = 0.76$ for an excitation current density of $j = 7.1\,\mathrm{A\,mm^{-2}}$. Thus, according to Eq. 2.68, the energy spread can be reduced by $14.9\,\%$ from 4.4×10^{-4} to 3.7×10^{-4}. The same relative reduction is achieved for the bunch length σ_s. This reduction in bunch length happens on the cost of an increased emittance. The emittance in such a setup increases by $316\,\%$. However, during low α operation, the transverse beam sizes are made large through coupling in order to have a long beam lifetime. Due to the increased emittance, the coupling can be reduced while maintaining a long lifetime. Therefore, the low-α operation mode can, additionally to the standard user operation mode, benefit from the installation of the RW at the MLS.

4.5 Low-ε Operation Mode

The installation of the RW will not only benefit the standard user operation mode at the MLS. It will also be possible to use the RW to adjust the horizontal source size in a limited range for other operation modes like the low emittance operation mode. In 2013, the low-ε operation mode at the MLS was developed and implemented. It is one result of a survey of beam optics solutions, for which the quadrupole strengths were scanned and for each setting different beam parameters like emittance, momentum compaction factor and Touschek lifetime were determined (Ries et al., 2013). The optical functions for the low emittance mode at the MLS are depicted in Fig. 1.3c. The dispersion is minimized in the dipoles in order to reduce

the quantum excitation. In turn, the dispersion is relatively high in the straight sections like the one where the RW can be installed.

The dispersion at the RW has a value of $0.87\,\mathrm{m}$. In Fig. 4.1, it is obtained that for a value for the dispersion of $0.9\,\mathrm{m}$ at the RW, an excitation current density of $6.0\,\mathrm{A\,mm^{-2}}$ is sufficient to reduce the emittance by a factor of ~ 2, while increasing the energy spread by $\sim 50\,\%$. The optimum ratio for the horizontal source size is found for D equal to -1. Here, the emittance is reduced by a factor of 2 while the energy spread increases by a factor of $\sqrt{2} \approx 1.414$, corresponding to $41.4\,\%$.

With an initial horizontal emittance of $41.2\,\mathrm{nm\,rad}$ for the low emittance operation mode, the resulting emittance is below $21\,\mathrm{nm\,rad}$, when operating the MLS at $D = -1$. Regarding the lifetime for this set up, the horizontal beam size is dominated by the large dispersion in the straight sections and the energy spread. Therefore, the lifetime is slightly reduced to $\sim 2.0\,\mathrm{h}$ compared to $2.06\,\mathrm{h}$ at $150\,\mathrm{mA}$ for the current set up and a varying vertical beam size. For a constant vertical beam size, the lifetime can be increased to $\sim 2.7\,\mathrm{h}$ at $150\,\mathrm{mA}$.

As an example, the horizontal source size at the IR beamline is approximated, assuming that the optical functions with RW stay the same as without the RW: the value of the dispersion at the source point of the IR beamline is $0.18\,\mathrm{m}$ in the low ε operation mode, while the horizontal β-function has a value of $0.75\,\mathrm{m}$. The gradient of the horizontal dispersion is $\eta'_x = -0.24$ and $\gamma_x = 1.35\,\mathrm{m^{-1}}$. As derived above, the emittance can be reduced from $41.2\,\mathrm{nm\,rad}$ to $21\,\mathrm{nm\,rad}$, while the energy spread increases from 4.4×10^{-4} to 6.2×10^{-4}. The source size therefore decreases from $192.8\,\mathrm{\mu m}$ to $167.9\,\mathrm{\mu m}$, which corresponds to a considerable reduction by $12.9\,\%$. The horizontal divergence σ'_x reduces from $258.4\,\mathrm{\mu rad}$ to $224.7\,\mathrm{\mu rad}$, corresponding to a reduction by $13.0\,\%$. Assuming constant vertical beam size and divergence due to white noise excitation, the brilliance at the IR-beamline can be improved by $32.1\,\%$.

Therefore, the performance of the low emittance operation mode at the MLS can be improved with the RW. The IR-beamline, being currently the major user of the low emittance operation mode, has an improved brilliance with RW due to reduced source size and divergence.

CHAPTER 5

Conclusion & Outlook

Concepts of improving the performance of light sources with the installation of transverse gradient Robinson Wigglers are currently investigated at different facilities around the world. In order to improve the performance of an existing accelerator, such a transverse gradient device has been shown to be a powerful and cost effective upgrade. For the MLS, which is not as sensitive to an increased energy spread as other facilities, it is possible to improve the lifetime by a factor of 2.3 while simultaneously improving the brilliance for selected beamlines.

In this setup, the damping is redistributed such that the horizontal emittance of the electron beam is reduced by a factor of 2 while the energy spread is increased by a factor of 3. Analytical calculations were presented and verified using particle tracking simulations. In addition, the effect was experimentally verified, though on a small scale, with the existing MLS lattice by steering the electron beam off-axis through quadrupole magnets.

The bunch length scales linearly with the increased energy spread. The bunch width reduction due to the shrinking emittance is on average compensated by the dispersive contribution to the bunch width from the increased energy spread. The Touschek lifetime component, which is the dominant lifetime contribution at the MLS, can thus be improved as the particle density inside the bunches is reduced. With an increased lifetime, the integrated stored beam current, and corresponding the integrated photon flux after a standard user operation run of six hours was shown to increase by approximately 30 %.

The derived normal conducting design for a RW, consisting of twelve poles, serves all requirements for machine integration and yields sufficiently high integrated fields in order to alter the damping partition as desired. An alternative superconducting design was developed and compared to the normal conducting solution. It shows advantages regarding the focussing characteristics of the device. However, due to

reliability reasons and the necessity to realize such a device in the coming year, the normal conducting design is chosen for the MLS.

In order to study effects on dynamic aperture and momentum acceptance, a simulation code was developed, which enables to implement arbitrary field maps into an accelerator lattice. Comprehensive simulations with this tracking code indicate that both devices yield sufficient dynamic aperture to guarantee operation of the MLS after installation.

Furthermore, it is possible to use the RW as a parasitic radiation source. The radiation spectra, calculated with `WAVE` (Scheer, 2012), show the characteristics of wiggler spectra for both the normal conducting and the superconducting solution.

In addition to improving the lifetime in the standard user operation mode, the RW may enhance the performance of the low-α operation mode as well as the low-ε operation mode. With simulations regarding the dynamic aperture and momentum acceptance, the allowed higher order multipole components for the normal conducting design were derived. These will be used for writing the technical specifications for the manufacturing process of the RW. It is proposed to start the manufacturing of a RW for the MLS in early 2017.

Outlook

Newly built light sources, like MAX IV, are optimized regarding their damping distribution using combined function magnets as deflecting magnets (Tavares et al., 2014). Different existing light sources with separated function lattices around the world aim to optimize their damping distribution with respect to emittance and brilliance using insertion devices, like Robinson Wigglers.

Other concepts of using transverse gradient ID's are currently investigated in the scope of laser wakefield accelerators (e.g. (Rodríguez et al., 2013)). To compensate large energy spreads, a transverse gradient undulator can be used to keep the deflection parameter K constant for all energies inside the electron bunch.

Another field may also take advantage of the concept: assuming a lepton collider with an initial damping partition equal to zero, the emittance can be reduced by a factor of 2 in order to improve the luminosity of the collider. The RW can be seen as a rather cost effective upgrade to push the luminosity (assuming that the vertical emittance is dominated by coupling). The hourglass effect has to be considered regarding the possible luminosity improvement because of the bunch lengthening by a factor of $\sqrt{2}$ (Furman, 1991). According to preliminary calculations, the luminosity can be improved by $\sim 50\%$, for β-functions at the interaction point of several milli metres.

Bibliography

M. G. Å. Anderson, M. Eriksson. Landau Cavities at MaxII. In *EPAC98 Conference*, pages 273–275, 1998.

G. Aad et al. Observation of a new particle in the search for the Standard Model Higgs boson with the ATLAS detector at the LHC. *Phys. Lett.*, B716:1–29, 2012.

M. Abo-Bakr. Design Studie für einen kompakten Niederenergie-Elektronenspeicherring für die Radiometrie im UV/VUV Spektralbereich. PhD thesis, Humboldt-Universität zu Berlin, 2000.

M. Abo-Bakr et al. Brilliant, Coherent Far-Infrared (THz) Synchrotron Radiation. *Phys. Rev. Lett.*, 90:094801, Mar 2003.

H. B. Abualrob et al. Soleil Emittance Reduction using a Robinson Wiggler. In *Proceedings, 3rd International Conference on Particle accelerator (IPAC 2012)*, pages 702–704, 2012.

Y. Baconnier et al. Emittance control of the PS e± beams using a robinson wiggler. *Nuclear Instruments and Methods in Physics Research Section A: Accelerators, Spectrometers, Detectors and Associated Equipment*, 234(2):244 – 252, 1985.

C. J. Bocchetta. Lifetime and Beam Quality. In *CAS Synchrotron Radiation and Free Electron LASERs, Grenoble, France*, pages 221–285, 1996.

K. L. Brown. A First and Second Order Matrix Theory for the Design of Beam Transport Systems and Charged Particle Spectrometers. *Adv. Part. Phys.*, 1:71–134, 1968.

S. Chatrchyan et al. Observation of a new boson at a mass of 125 GeV with the CMS experiment at the LHC. *Physics Letters B*, 716(1):30 – 61, 2012. ISSN 0370-2693.

J. A. Clarke. The science and technology of undulators and wigglers. Oxford series on synchrotron radiation. Oxford Univ. Press, Oxford, 2004.

L. Deniau et al. The MAD-X Program - User's Reference Manual. CERN - European Organisation For Nuclear Research, 2015.

M. Dirsat, S. Wiese, and V. Dürr. Helmholtz-Zentrum Berlin für Materialien und Energie, 2014-2016.

V. Dürr and J. Borninkhof. personal communication, Helmholtz-Zentrum Berlin für Materialien und Energie, 2013.

J. Feikes et al. Metrology Light Source: The first electron storage ring optimized for generating coherent THz radiation. *Phys. Rev. ST Accel. Beams*, 14:030705, Mar 2011.

A. Ferrari, P. R. Sala, A. Fassò, and J. Ranft. FLUKA: A multi-particle transport code (program version 2005). CERN, Geneva, 2005.

M. A. Furman. Hourglass Effects for Asymmetric Colliders. In *PAC91 Conference*, pages 422–424, 1991.

T. Goetsch. Lifetime Studies at the Metrology Light Source and the Ånströmquelle Karlsruhe. diploma thesis, Karlsruhe Institute of Technology, 2013.

Hamamatsu. Universal Streak Camera C5680 Series, 2010.

R. H. Helm et al. Evaluation of Synchrotron Radiation Integrals. In *PAC73 Conference*, pages 900–901, 1973.

R. Klein et al. Operation of the Metrology Light Source as a primary radiation source standard. *Phys. Rev. ST Accel. Beams*, 11:110701, Nov 2008.

J. le Duff. Single And Multiple Touschek Effects. In *CERN Accelerator School*, volume CERN 89-01, 1989.

D. W. Lynch. Tantalus, a 240MeV Dedicated Source of Synchrotron Radiation, 1968 - 1986. *Journal of Synchrotron Radiation*, 4(6):334–343, Nov 1997.

L. S. Nadolski. Horizontal Emittance Reduction using a Robinson Wiggler. Talk, ESLSXIX, Aarhus, 2011.

J. C. O. Chubar, P. Elleaume. A 3D Magnetostatics Computer Code for Insertion Devices. In *SRI97 Conference*, pages 481–484, 1997.

J. C. P. Elleaume, O. Chubar. Computing 3D Magnetic Field from Insertion Devices. In *PAC97 Conference*, pages 3509–3511, 1997.

A. Piwinski. The Touschek effect in strong focusing storage rings. DESY 98-179, 1998.

M. Ries. Nonlinear momentum compaction and coherent synchrotron radiation at the Metrology Light Source - low-alpha commissioning and development. PhD thesis, Humboldt-Universität zu Berlin, 2014.

M. Ries and J. Feikes. personal communication, Helmholtz-Zentrum Berlin für Materialien und Energie, 2013-2016.

M. Ries, J. Feikes, T. Goetsch, and G. Wüstefeld. Survey of Beam Optics Solutions for the MLS Lattice. In *IPAC2013 Shanghai, China*, pages 1883–1885, 2013.

K. W. Robinson. Radiation Effects in Circular Electron Accelerators. *Phys. Rev.*, 111:373–380, Jul 1958.

V. A. Rodríguez et al. Development of a Superconducting Transverse-Gradient Undulator for Laser-Wakefield Accelerators. *IEEE Transactions on Applied Superconductivity*, 23, 2013.

S. Russenschuck. Field computation for accelerator magnets: analytical and numerical methods for electromagnetic design and optimization. Wiley, Weinheim, 2010.

S. Sakanaka et al. Improvement in the beam lifetime by means of an rf phase modulation at the KEK Photon Factory storage ring. *Phys. Rev. ST Accel. Beams*, 3, May 2000.

M. Scheer. WAVE - A Computer Code for the Tracking of Electrons through Magnetic Fields and the Calculation of Spontaneous Synchrotron Radiation. In *ICAP2012 Conference, Rostock-Warnemünde, Germany*, pages 86–88, 2012.

M. Scheer and G. Wüstefeld. Beam optics code with symplectic tracking options for arbitrary, 3-dimensional magnetic fields. private communication, Helmholtz-Zentrum Berlin für Materialien und Energie, 2014.

M. Sommer et al. Interaction of RF Phase Modulation and Coupled-Bunch Instabilities at the DELTA Storage Ring. In *Proceedings of IPAC2016, Busan, Korea*, pages 1720–1723, 2016.

P. F. Tavares, S. C. Leemann, M. Sjöström, and Å. Andersson. The MAXIV storage ring project. *Journal of Synchrotron Radiation*, 21(5):862–877, Sep 2014.

H. Wiedemann. Particle Accelerator Physics. Number ISBN-13 978-3-540-49043-2 in 3rd. Springer-Verlag Berlin Heidelberg New York, 2007.

K. Wille. The Physics of Particle Accelerators - An Introduction. Number ISBN 0-19-850549-3. Oxford University Press Inc., New York, 2005.

E. Wilson. An Introduction to Particle Accelerators. Oxford University Press Inc., New York, 2001.

Wolfram Research, Inc. Mathematica, *Version 10.4*. Wolfram Research, Inc., Champaign, IL, 2016.

A. Wolski. Low-emittance Storage Rings. In *CAS Advanced Accelerator Physics, Trondheim, Norway*, pages 245–294, 2013.

A. Wolski. Beam Dynamics in High Energy Particle Accelerators. Imperial College Press, 2014. ISBN 9781783262779.

Appendix A

Codes

A.1 `RADIA` Notebook

```
1  geo[]:=(
2  poleshape = ReadList["/path/to/poleshape.txt",{Number,Number}];
3  poleshape[[All,All]]=poleshape[[All,All]]*1000;
4
5  pole = radObjThckPgn[N[polelength/4],N[polelength/2.],N[poleshape]];
6  p14=radObjThckPgn[N[-2*longgap-3*polelength/4-polelength/8-polelength
       /16-deltaepole/4.],N[polelength/8.+deltaepole/2.],N[poleshape]];
7  p34=radObjThckPgn[N[-longgap-3*polelength/16.-3*polelength/8.],N[3*
       polelength/8.],N[poleshape]];
8
9  pole=radObjCutMag[pole,{N[polelength/4],N[poleshape[[1,1]]],N[
       poleshape[[1,2]]+chamfer]},{N[0],-1,-1}][[1]];
10 p14=radObjCutMag[p14,{N[-2*longgap-3*polelength/4-polelength/8-
       polelength/16],N[poleshape[[1,1]]],N[poleshape[[1,2]]+chamfer]},{N
       [0],-1,-1}][[1]];
11 p34=radObjCutMag[p34,{N[-longgap-3*polelength/16.-3*polelength/8.],N[
       poleshape[[1,1]]],N[poleshape[[1,2]]+chamfer]},{N[0],-1,-1}][[1]];
12
13 Do[
14    deltay = N[poleshape[[i+1,1]]-poleshape[[i,1]]];
15    deltaz = N[poleshape[[i+1,2]]-poleshape[[i,2]]];
16    alpha =ArcTan[deltaz/deltay];
17    pole=radObjCutMag[pole,{N[0.0],N[poleshape[[i+1,1]]-Sin[alpha]*
          chamfer],N[poleshape[[i+1,2]]+Cos[alpha]*chamfer]},{N[-deltay*
          chamfer*Cos[alpha]-deltaz*chamfer*Sin[alpha]],N[deltaz*chamfer],N
          [-deltay*chamfer]}][[1]];
18    p14=radObjCutMag[p14,{N[-2*longgap-polelength-deltaepole/4.],N[
          poleshape[[i+1,1]]-Sin[alpha]*chamfer],N[poleshape[[i+1,2]]+Cos[
```

```mathematica
        alpha]*chamfer]},{N[-deltay*chamfer*Cos[alpha]-deltaz*chamfer*Sin
        [alpha]],N[deltaz*chamfer],N[-deltay*chamfer]}][[1]];
19    p34=radObjCutMag[p34,{N[-longgap-3*polelength/4],N[poleshape[[i
        +1,1]]-Sin[alpha]*chamfer],N[poleshape[[i+1,2]]+Cos[alpha]*
        chamfer]},{N[-deltay*chamfer*Cos[alpha]-deltaz*chamfer*Sin[alpha
        ]],N[deltaz*chamfer],N[-deltay*chamfer]}][[1]];
20    ,{i,18}];
21  radObjDivMag[pole,n1];
22  radObjDrwAtr[pole,{0.25,0.25,0.25},0.001];
23
24  RadTrfZerPerp[pole,{N[polelength/2],0,0},{1,0,0}];
25
26  c1=radObjRaceTrk[{N[polelength/2],0,N[coilverticalposMain]},{N[rmin],N
        [0.5*longgap+rmin-0.5]},{N[polelength-2*rmin],N[width]},N[
        coilheightMain],20,mcur];
27  radObjDrwAtr[c1,{0.72,0.45,0.2},0.001];
28
29  polecoil=radObjCnt[{pole,c1}];
30
31  RadTrfZerPara[polecoil,{0,0,0},{0,0,1}];
32
33  RadTrfZerPara[polecoil,{N[polelength+0.5*longgap],0,0},{1,0,0}];
34
35  If[Mod[npoles,2]==0,
36    (*then:*)
37    radTrfMlt[polecoil,radTrfTrsl[{N[2*polelength+2*longgap],0,0}],N[(
        npoles-4)/2]],
38    (*else:*)
39    radTrfMlt[polecoil,radTrfTrsl[{N[2*polelength+2*longgap],0,0}],N[(
        npoles-5)/2]];
40    expole = radObjThckPgn[N[(2*polelength+2*longgap)*((npoles-5)/2)+
        polelength/4],N[polelength/2.],N[poleshape]];
41    expole=radObjCutMag[expole,{N[(2*polelength+2*longgap)*((npoles-5)
        /2)+polelength/4],N[poleshape[[1,1]]],N[poleshape[[1,2]]+chamfer
        ]},{N[0],-1,-1}][[1]];
42    Do[
43      deltay = N[poleshape[[i+1,1]]-poleshape[[i,1]]];
44      deltaz = N[poleshape[[i+1,2]]-poleshape[[i,2]]];
45      alpha =ArcTan[deltaz/deltay];
46      expole=radObjCutMag[expole,{N[(2*polelength+2*longgap)*((npoles-5)
          /2)],N[poleshape[[i+1,1]]-Sin[alpha]*chamfer],N[poleshape[[i
          +1,2]]+Cos[alpha]*chamfer]},{N[-deltay*chamfer*Cos[alpha]-
          deltaz*chamfer*Sin[alpha]],N[deltaz*chamfer],N[-deltay*chamfer
          ]}][[1]];
```

```
47        ,{ i ,18}];
48     radObjDivMag [ expole , n1 ] ;
49     radObjDrwAtr [ expole ,{0.25 ,0.25 ,0.25} ,0.001];
50     RadTrfZerPerp [ expole ,{N[(2∗ polelength +2∗longgap )∗(( npoles −5)/2)+
           polelength /2] ,0 ,0} ,{1 ,0 ,0}];
51     exc1=radObjRaceTrk [{N[(2∗ polelength +2∗longgap )∗(( npoles −5)/2)+
           polelength /2] ,0 ,N[ coilverticalposMain ]} ,{N[ rmin ] ,N[0.5∗ longgap+
           rmin −0.5]} ,{N[ polelength −2∗rmin ] ,N[ width ]} ,N[ coilheightMain ] ,20 ,
           mcur ] ;
52     radObjDrwAtr [ exc1 ,{0.72 ,0.45 ,0.2} ,0.001];
53     expolecoil=radObjCnt [{ expole , exc1 }];
54     RadTrfZerPara [ expolecoil ,{N[(2∗ polelength +2∗longgap )∗(( npoles −5)/2)+
           polelength /2] ,0 ,0} ,{0 ,0 ,1}];
55     polecoil=radObjCnt [{ polecoil , expolecoil }];
56     ];
57
58  (∗End−poles and −coils ∗)
59
60  radObjDivMag [ p14 , n1 ] ;
61  radObjDrwAtr [ p14 ,{0.25 ,0.25 ,0.25} ,0.001];
62  RadTrfZerPerp [ p14 ,{N[−2∗longgap −3∗polelength /4.− polelength
       /8.] ,0 ,0} ,{1 ,0 ,0}];
63
64  c14=radObjRaceTrk [{N[−2∗longgap −3∗polelength /4.− polelength /8.] ,0 ,N[
       coilverticalposMain ]} ,{N[ rmin ] ,N[0.5∗ longgap+rmin −0.5 −4.]} ,{N[0] ,N[
       width ]} ,N[ coilheightMain ] ,20 ,N[mcur+delcurep14 ]];
65  radObjDrwAtr [ c14 ,{0.72 ,0.45 ,0.2} ,0.001];
66
67  radObjDivMag [ p34 , n1 ] ;
68  radObjDrwAtr [ p34 ,{0.25 ,0.25 ,0.25} ,0.001];
69  RadTrfZerPerp [ p34 ,{N[−longgap −3∗polelength /8] ,0 ,0} ,{1 ,0 ,0}];
70
71  c34=radObjRaceTrk [{N[−longgap −3∗polelength /8] ,0 ,N[ coilverticalposMain
       ]} ,{N[ rmin ] ,N[0.5∗ longgap+rmin −0.5]} ,{N[0.75∗ polelength −2∗rmin ] ,N[
       width ]} ,N[ coilheightMain ] ,20 ,−N[mcur+delcurep34 ]];
72  radObjDrwAtr [ c34 ,{0.72 ,0.45 ,0.2} ,0.001];
73
74  epc14=radObjCnt [{ p14 , c14 }];
75  epc34=radObjCnt [{ p34 , c34 }];
76
77  RadTrfZerPara [ epc14 ,{0 ,0 ,0} ,{0 ,0 ,1}];
78  RadTrfZerPara [ epc34 ,{0 ,0 ,0} ,{0 ,0 ,1}];
79
80  epc=radObjCnt [{ epc34 , epc14 }];
```

```
81
82  If [Mod[npoles, 2] == 0,
83     RadTrfZerPara[epc,{N[(npoles−4)/2*polelength+((npoles−4)/2−0.5)*
             longgap],0,0},{1,0,0}]
84     ,
85     RadTrfZerPerp[epc,{N[(npoles−4)/2*polelength+((npoles−4)/2−0.5)*
             longgap],0,0},{1,0,0}]
86     ];
87
88  (*corrector coils*)
89  CC=radObjRaceTrk[{N[(npoles−4)/2*polelength+((npoles−4)/2−0.5)*longgap
             ],0,N[coilverticalposAdd]},{rmin,N[rmin+coilthicknesAdd]},{N[(
             npoles−2)*polelength+(npoles−1)*longgap−2*rmin],N[width−2*rmin]},N[
             coilheightAdd],10,ccur];
90  radObjDrwAtr[CC,{0.82,0.5,0.25},0.001];
91  CCu=radObjRaceTrk[{N[(npoles−4)/2*polelength+((npoles−4)/2−0.5)*
             longgap],0,−N[coilverticalposAdd]},{rmin,N[rmin+coilthicknesAdd]},{
             N[(npoles−2)*polelength+(npoles−1)*longgap−2*rmin],N[width−2*rmin
             ]},N[coilheightAdd],10,ccur];
92  radObjDrwAtr[CCu,{0.82,0.5,0.25},0.001];
93
94  (*bringing all together*)
95  backyoke1=radObjRecMag[{N[(npoles−4)/2*polelength+((npoles−4)/2−0.5)*
             longgap],0,200.0},{N[LoA−longgap+2],135,100}];
96  radObjDivMag[backyoke1,n2];
97  backyoke2=radObjRecMag[{N[(npoles−4)/2*polelength+((npoles−4)/2−0.5)*
             longgap],0,−200.0},{N[LoA−longgap+2],135,100}];
98  radObjDivMag[backyoke2,n2];
99  backyoke=radObjCnt[{backyoke1,backyoke2}];
100 radObjDrwAtr[backyoke,{0.3,0.3,0.3},0.001];
101 TG = radObjCnt[{polecoil,epc,backyoke,CC,CCu}];
102 radMatApl[pole,mat2];
103 If[Mod[npoles,2]==0,,radMatApl[expole,mat2]];
104 radMatApl[p14,mat2];radMatApl[p34,mat2];
105 radMatApl[backyoke,mat1];
106 radTrfOrnt[TG,radTrfTrsl[{N[polelength+2.5*longgap],0,0}]];
107 radTrfOrnt[TG,radTrfRot[{0,0,0},{0,0,1},N[−Pi/2]]]; (*needed for in
         radia tracking*)
108 )
109
110 radUtiDelAll[];
111
112 width=131; (*width of the poles*)
113
```

```
114 npoles = 12;(*number of poles (including end poles)*)
115
116 LoA = 1900; (* over all length of the device*)
117
118 polelength=LoA/(npoles-2+npoles*0.6);(*length of main poles*)
119 deltaepole=0.0;
120 longgap=polelength*0.6; (*gap between poles (filled with coils)*)
121 chamfer =5;
122
123 coilthicknesMain=longgap/2-1;
124 coilthicknesAdd=0.5*longgap;
125
126 coilverticalposMain=90.0;
127 coilverticalposAdd=25;
128
129 coilheightMain=119;
130 coilheightAdd=10;
131
132 rmin=20;
133 rmax=longgap/2-1;
134
135 (*current densities in A/mm^2*)
136 mcur=-9.0;(*current density in the main coils (including end poles)*)
137 ccur=4.28;(*current density in the corrector coil*)
138 delcurep14 =1.15;
139 delcurep34 = 0.0;
140 np=15;
141 nx=3;ny=3;nz=3;
142 n1={{nx,1},{ny,1},{nz,1}};
143 n2={{100,1},{ny,1},{nz,1}};
144 n3={{nx,1},{ny,1},{nz,1}};
145 n4={{nx,1},{50,1},{nz,1}};
146
147 mat1=RadMatXc06[]; (* standard steel for backyoke *)
148 mat2=RadMatAFK502[];(* cobalt steel for pole tips (49 percent cobalt,
        49 percent iron, 2 percent vanadium*)
149 geo[]; (* with this call of geo(), the geometry is built *)
150 re=radSolve[TG,0.001,1000];
```

A.2 Lifetime Calculation

```python
from pylab import *

import matplotlib.pyplot as plt
import numpy
import scipy.integrate as integrate
import argparse

def tunecalc(frev,gamma,alpha,V,E0,h):
    psi = 0.0
    wrev = 2*pi*frev
    etac = 1/gamma**2 - alpha
    omega = numpy.sqrt(wrev**2*h*numpy.absolute(etac)*V*numpy.cos(psi)
        /2/pi/E0)
    return omega

def F(q):
    y = 2.0 * (numpy.sqrt(q**2-1)-numpy.arccos(1/q))
    return y

def deltapcalc(V,alpha):
    V0 = V*1000
    U0 = 9062
    q = V0/U0
    deltap = numpy.sqrt(U0*F(q)/pi/alpha/80/629e6)
    return deltap

def Dint1(x):
    y = (numpy.log(x)*numpy.exp(-x))/x
    return y

def Dint2(x):
    y = numpy.exp(-x)/x
    return y

def D(x):
    q1 = integrate.quad(Dint1,x,+inf)
    q2 = integrate.quad(Dint2,x,+inf)
    y = numpy.sqrt(x)*(-1.5*numpy.exp(-x) + 0.5*x*q1[0]+0.5*(3.0*x-x*
        numpy.log(x) + 2.0)*q2[0])
    return y
```

```python
def touschek(gamma, betx, bety, dispx, delta, epsilon, vertemittance, dpp,
        sigs, s, ne):
    clight=299792458
    dummy = 0.0
    sigx = numpy.empty((betx.shape[0],1))
    sigy = numpy.empty((betx.shape[0],1))
    zeta = numpy.empty((betx.shape[0],1))
    K = numpy.empty((betx.shape[0],1))
    tau = numpy.empty((betx.shape[0],1))
    for i in range(0,betx.shape[0]-1):
        sigx[i] = numpy.sqrt(epsilon*betx[i]+delta**2*dispx[i]**2)
        sigy[i] = numpy.sqrt(vertemittance*bety[i])
        zeta[i] = ((dpp*betx[i])/(gamma*sigx[i]))**2
        K[i] = D(zeta[i])
        tau[i] = (8*pi*gamma**2*(sigx[i]*sigy[i]*sigs)*(dpp**3))/((2.81794
            e-15)**2*clight*ne*K[i])
        tau[i] = tau[i]/3600.0
        dummy = dummy + (s[i+1]-s[i])/tau[i]
    taut = 48.0/dummy


    return taut


def quantxlt(emit, betax, dispx, sige, taux, taus):
    sigt = numpy.sqrt(emit*betax+sige**2*dispx**2)
    r = dispx**2*sige**2/sigt**2
    tauqvs = taux*taus*numpy.exp(0.035**2/2/sigt**2)*sigt**3/0.035**3/
        numpy.sqrt(2*pi)/(taux*r+taus*(1-r))/numpy.sqrt(r*(1-r))/3600
    tauqges=numpy.sum(1/tauqvs)
    tauqges=1/tauqges
    return tauqges


def quantums(taus, delta, delta_acc):
    tauq = taus*delta**2/delta_acc**2*numpy.exp(delta_acc**2/2/delta**2)
        /3600
    return tauq


parser = argparse.ArgumentParser()
parser.add_argument('filename1')
parser.add_argument('filename2')
parser.add_argument('D',type=float)
parser.add_argument('emit',type=float)
parser.add_argument('delta',type=float)
parser.add_argument('alpha',type=float)
parser.add_argument('voltage',type=float)
```

```python
80  parser.add_argument('ringcurrent',type=float)
81  parser.add_argument('-a','--deltaacc',type=float)
82  parser.add_argument('-v','--veremit',type=float)
83  parser.add_argument('-c','--coupling',type=float)
84  parser.add_argument('-l','--lines', type=int)
85  args=parser.parse_args()
86  if args.lines:
87     skiplines=args.lines
88  else:
89     skiplines=0
90
91  if args.D:
92     dam = args.D
93  else:
94     dam = -0.052
95
96  if args.emit:
97     emittance = args.emit
98  else:
99     emittance = 100.E-9
100
101 if args.delta:
102    sige = args.delta
103 else:
104    sige = 4.4E-4
105
106 if args.ringcurrent:
107    ir = args.ringcurrent
108 else:
109    ir = 200.0
110
111 if args.coupling:
112    cplg = args.coupling
113 else:
114    cplg = 0.022
115
116 if args.deltaacc:
117    acceptance = args.deltaacc
118    alphac = args.alpha
119    v0 = args.voltage
120 else:
121    if args.voltage:
122       if args.alpha:
123          alphac = args.alpha
```

```python
124           v0 = args.voltage
125           acceptance = deltapcalc(args.voltage,alphac)
126         else:
127           alphac = 0.03
128           v0 = args.voltage
129           acceptance = deltapcalc(args.voltage,0.03)
130     else:
131       if args.alpha:
132         alphac = args.alpha
133         v0 = 800.0
134         acceptance = deltapcalc(800.0,alphac)
135       else:
136         alphac = 0.03
137         v0 = 800.0
138         acceptance = deltapcalc(800.0,0.03)
139
140  data1 = loadtxt(args.filename1,skiprows=skiplines)
141  data2 = loadtxt(args.filename2,skiprows=skiplines)
142
143  s = data1[:,0]
144  betx = data1[:,1]
145  bety = data1[:,3]
146
147  dispx = data2[:,1]
148
149  taug = 24.5
150
151  if args.veremit:
152    vertemittance=args.veremit
153  else:
154    vertemittance=emittance*cplg
155
156  clight=299792458
157
158
159  ne = ir/80 * (6.2415e15/299792458*48.0)
160  print 'No. of electrons per bunch = ',ne
161
162  fsyn = tunecalc(6.25e6,1231,alphac,v0*1000,629e6,80)
163
164  print 'synchrotron frequency = ',fsyn
165
166  sigs = alphac*clight*sige/fsyn
167
```

```
168  taux = 2/(1−dam)∗629e6/9.062e3/6.25e6
169  taus = 2/(2+dam)∗629e6/9.062e3/6.25e6
170
171  print 'Emittance = ',emittance,' Energy Spread = ',sige,' Bunch Length
        = ',sigs
172  print 'Acceptance = ',acceptance
173
174  print 'Calculating the Touschek lifetime ...'
175  taut = touschek(1231,betx,bety,dispx,sige,emittance,vertemittance,
        acceptance,sigs,s,ne)
176  print 'Touschek lifetime = ',taut
177  print 'Calculating the horizontal quantum lifetime ...'
178  tauqx = quantxlt(emittance,betx,dispx,sige,taux,taus)
179  print 'Horizontal quantum lifetime = ',tauqx
180  print 'Calculating the longitudinal quantum lifetime ...'
181  tauqs = quantums(taus,sige,acceptance)
182  print 'Longitudinal quantum lifetime = ',tauqs
183
184  if tauqs < 10000:
185    if tauqx < 10000:
186      tt = 1/(1/taug+1/taut+1/tauqx+1/tauqs)
187    else:
188      tt = 1/(1/taug+1/taut+1/tauqs)
189  else:
190    if tauqx < 10000:
191      tt = 1/(1/taug+1/taut+1/tauqx)
192    else:
193      tt = 1/(1/taug+1/taut)
194
195  print 'Resulting lifetime = ',tt
```

Index

Acknowledgements

Selbständigkeitserklärung

Ich erkläre, dass ich die vorliegende Arbeit selbständig und nur unter Verwendung der angegebenen Literatur und Hilfsmittel angefertigt habe.

Berlin, den 28. Juli 2016   Tobias Tydecks